# Bipropellant Engine Plume Contamination Program

Volume I
Chamber Measurements — Phase I

R. E. Alt
ARO, Inc.

December 1979

Final Report for Period September 5 — December 12, 1977

ARNOLD ENGINEERING DEVELOPMENT CENTER
ARNOLD AIR FORCE STATION, TENNESSEE
AIR FORCE SYSTEMS COMMAND
UNITED STATES AIR FORCE

This report has been reviewed by the Information Office (OI) and is releasable to the National Technical Information Service (NTIS). At NTIS, it will be available to the general public, including foreign nations.

APPROVAL STATEMENT

This report has been reviewed and approved.

JOSEPH F. PAWLICK, JR., Lt Colonel, USAF
Test Director, VKF Division
Directorate of Test Operations

Approved for publication:

FOR THE COMMANDER

JAMES D. SANDERS, Colonel, USAF
Deputy for Operations

REPORT DOCUMENTATION PAGE		READ INSTRUCTIONS BEFORE COMPLETING FORM
1. REPORT NUMBER AEDC-TR-79-28	2. GOVT ACCESSION NO.	3. RECIPIENT'S CATALOG NUMBER
4. TITLE (and Subtitle) BIPROPELLANT ENGINE PLUME CONTAMINATION PROGRAM: VOLUME I, CHAMBER MEASUREMENTS --PHASE I		5. TYPE OF REPORT & PERIOD COVERED Final Report, September 5 - December 12, 1977
		6. PERFORMING ORG. REPORT NUMBER
7. AUTHOR(s) R. E. Alt, ARO, Inc., a Sverdrup Corporation Company		8. CONTRACT OR GRANT NUMBER(s)
9. PERFORMING ORGANIZATION NAME AND ADDRESS Arnold Engineering Development Center Air Force Systems Command Arnold Air Force Station, Tennessee 37389		10. PROGRAM ELEMENT, PROJECT, TASK AREA & WORK UNIT NUMBERS Program Elements 62302F 63411F
11. CONTROLLING OFFICE NAME AND ADDRESS Air Force Rocket Propulsion Laboratory/PACP Edwards Air Force Base, California 93523		12. REPORT DATE December 1979
		13. NUMBER OF PAGES 102
14. MONITORING AGENCY NAME & ADDRESS(if different from Controlling Office)		15. SECURITY CLASS. (of this report) UNCLASSIFIED
		15a. DECLASSIFICATION/DOWNGRADING SCHEDULE N/A

16. DISTRIBUTION STATEMENT (of this Report)

Approved for public release; distribution unlimited.

17. DISTRIBUTION STATEMENT (of the abstract entered in Block 20, if different from Report)

18. SUPPLEMENTARY NOTES

Available in DDC.

19. KEY WORDS (Continue on reverse side if necessary and identify by block number)

rocket plumes	spacecraft contamination
plume contamination	quartz crystal microbalance
plume diagnostics	QCM

20. ABSTRACT (Continue on reverse side if necessary and identify by block number)

    An experimental program to measure the mass flux in the backflow region of a 5-lbf bipropellant thruster at angles up to 147 deg with respect to the plume centerline using temperature-controlled and temperature-compensated quartz crystal microbalances (QCM's) is presented. The measurements were conducted in a high vacuum cryogenic chamber (Aerospace Chamber 10V) at AEDC. Gaseous helium and liquid helium cryopanels provided a blank-off pressure

DD _{1 JAN 73} FORM 1473   EDITION OF 1 NOV 65 IS OBSOLETE

20. ABSTRACT. Concluded

in the 10^{-6} torr range and maintained the background pressure in the 10-5 torr range while pulse firing the motor (25- to 100-msec pulse width, 1- to 10-percent duty cycle). Chamber recovery time was a few tenths of a second. Several motor configurations and operating conditions were compared for potential contamination effects. Variations included: injector - zero and 45-deg splash plate; combustion chamber - 2-in. cylindrical, 1.5-in. cylindrical, and 2-in. conical; nozzle area ratio - 50:1 and 100:1; oxidizer fuel ratio - 1.4, 1.6, and 1.8; chamber pressure - 75, 100, and 125 psia; pulse duty cycle - 1, 5, and 10 percent, and continuous. In addition to the QCM's, more extensive diagnostics were used to fully characterize the plume constituents, to measure exit plane properties, and to monitor nozzle lip effects. Infrared spectroscopy, two-angle laser interference thickness monitoring, IR scanning camera, solar cells, attenuated total reflectance (ATR) plates, witness plates, photography, and mass spectroscopy were among the other diagnostic tools.

AFSC
Arnold AFS Tenn

PREFACE

The work reported herein was conducted by the Arnold Engineering Development Center (AEDC), Air Force Systems Command (AFSC) at the request of the Air Force Rocket Propulsion Laboratory (AFRPL/PACP), the Space and Missile Systems Organization (SAMSO/LVRE), and the AEDC/DOT under Program Elements 63411F and 62302F. The results presented were obtained by ARO, Inc., AEDC Division (a Sverdrup Corporation Company), operating contractor for the AEDC, AFSC, Arnold Air Force Station, Tennessee, under ARO Project number V41Q-49. The data analysis was completed on May 12, 1978, and the manuscript was submitted for publication on July 18, 1979.

J. A. Roux, B. E. Wood, D. F. Frazine, R. Dawbarn, and H. E. Scott are coauthors of this report.

CONTENTS

ILLUSTRATIONS

TABLES

1.0 INTRODUCTION

The potential contamination of spacecraft surfaces and components by exhaust products from spacecraft thrusters, whether solid, liquid or electric, is of considerable concern to the spacecraft design community. This concern is attributed to the development of more sophisticated spacecraft systems designed to perform multiple, noninterfering missions for longer periods of time in space. Contamination and subsequent degradation of sensitive spacecraft surfaces and components such as thermal control coatings, solar cells, antennas, optical devices, and cooled infrared sensors can compromise mission objectives and lead to a reduction in spacecraft lifetime. For example, contamination of surfaces with low absorptivity-to-emissivity (α/ϵ) properties, required for passive control of spacecraft temperatures, can result in a heat imbalance with a subsequent change in spacecraft temperature, thus affecting the spacecraft mission and/or lifetime.

In order to predict the effects of rocket exhaust plumes from liquid bipropellant and monopropellant engines on spacecraft surfaces of interest, a computer code (CONTAM) (Ref. 1) was developed at the request of the Air Force Rocket Propulsion Laboratory (AFRPL). The code has been available to DOD agencies and industry for several years but has received only limited use, primarily because of the programming complexity of the code but also because of a lack of verification with representative engine data. The code is also deficient in the prediction of mass flow outside the nozzle Prandtl-Meyer expansion angle, due to the fact that the code does not incorporate any sort of boundary-layer model. The AFRPL currently is in the process of having the code improved and verified.

The verification of the accuracy of the code will require comparisons of predictions to representative measured data. Monopropellant engine data have been obtained at the Arnold Engineering Development Center (AEDC) previously (Refs. 2 and 3), and bipropellant data are being collected during the current Bipropellant Contamination program, part of which is included in this report. The Bipropellant Contamination program was requested by the AFRPL to obtain data from a representative engine for use in CONTAM code verification and also to aid the Space and Missile Systems Organization (SAMSO) in assessing the potential contamination from the Space Transportation System's (STS) 25- and 500-lbf thrust bipropellant engines.

The engine selected for the program was a 5-lbf thrust bipropellant engine developed by the Aerojet Corporation (Ref. 4). The engine analysis and design were based on the existing CONTAM computer code, and initial sea-level tests by Aerojet verified the high performance of the thruster. In addition, the engine mass flow was low enough to enable simulation of a high altitude operating environment during the engine firings. This allowed

mass flux measurements to be made outside the Prandtl-Meyer expansion angle (backflow region) with a high degree of accuracy.

The objectives of the Bipropellant Contamination program were as follows:

a. Development and demonstration of a cryogenic pumping capability in an existing AEDC altitude simulation chamber that would permit accurate mass flux measurements to be made in the backflow region of the 5-lbf bipropellant engine.

b. Measurement of the mass flux distribution in the bipropellant engine plume over a wide range of angles with respect to the nozzle axis for CONTAM code verification while the engine configuration and operating conditions were varied to determine any significant dependence on these parameters.

c. Characterization of the plume by identification of the plume constituents (gaseous species, droplets, particles, etc.), measurement of the properties of condensed plume constituents, and assessment of the effects of the condensed constituents on selected surfaces in the plume.

The program was conducted in the Aerospace Research Chamber (10V) of the von Kármán Gas Dynamics Facility (VKF), AEDC, at background pressure levels near 1×10^{-5} torr during engine pulsings at duty cycles up to 10 percent. Eleven quartz crystal microbalances (QCM's) were used to measure the plume mass flux distribution for a wide range of engine operating parameters. The mass flux in the plume flow field is presented for angles between 30 and 147 deg from the nozzle axis. Plume constituents condensed at temperatures between 26 and 200°K are identified. Also shown are the effects of the plume gases on solar cells and Attenuated Total Reflectance (ATR) plates which were exposed to the plume while being maintained near 300°K.

2.0 APPARATUS

2.1 TEST UNIT - AEROSPACE CHAMBER 10V

The Bipropellant Contamination program was conducted in AEDC Aerospace Chamber 10V. The chamber and its performance capability are described in Ref. 5. The chamber is designed for testing small rocket engines under space vacuum conditions. The stainless steel chamber is 10 ft in diameter and 20 ft long. It is equipped with an internal cryogenic system designed for high efficiency vacuum pumping of rocket exhaust products (Ref. 6).

The 10V chamber pumpdown is accomplished with mechanical vacuum pumps and a 6-in. diffusion pump. After the chamber is pumped down, the cryogenic surfaces are cooled. The chamber cryogenic system consists of a liquid nitrogen (LN_2)-cooled (77°K) chamber liner, a radial-finned gaseous helium (GHe)-cooled (20°K) cryopump, and a liquid helium (LHe)-cooled (4.2°K) cryopump. The chamber configuration for the Bipropellant Contamination program is shown in Fig. 1.

The free expansion of the rocket plume is made possible by the high capture rate (pumping speed) of the exhaust gases on the chamber's cryogenically cooled surfaces. The rocket engine is located at the front of the chamber and fires axially along the chamber horizontal centerline. The engine is installed in this position by means of an antechamber which extends through an opening on the front of the chamber. The LN_2-cooled surfaces, in the form of a 9-ft-diam cylinder, line the entire length of the chamber. There are several cutouts in the liner for visual and physical access to the chamber interior. The radial-finned GHe-cooled cryopump, approximately 6 ft in inner diameter, extends nearly the entire length of the LN_2 liner. The circular region at the far end of the chamber is covered with a liquid nitrogen-cooled shield, and the region at the front of the chamber, between the antechamber and the LN_2 liner, is covered with a GHe-cooled shield. The LHe-cooled cryopump is on the chamber vertical axis at the far end of the chamber. The requirement for making plume measurements behind the rocket nozzle, in the plume backflow region, required the installation of a small (approximately 7-ft² surface area), LHe-cooled cryopump in this region. Figure 2 shows a view of the cryogenic system installation in the 10V chamber.

A chamber background pressure of approximately 1×10^{-5} torr insured that the plume expansion was not significantly different from what would occur in an operational space environment; that is, the molecular mean free path of about 2 m was long enough to permit molecules to travel from the nozzle to the QCM's without being significantly deflected by intermolecular collisions. The background gas in the chamber during the pulse firing was primarily hydrogen (H_2), since the pumping speed of the LHe surfaces for H_2 was considerably less than the pumping speed of the GHe surfaces for nitrogen (N_2) and carbon monoxide (CO) or the LN_2 surfaces for carbon dioxide (CO_2) and water vapor (H_2O), the other primary gas species in the plume of a bipropellant engine.

The chamber instruments used to assess the chamber performance during engine firings were four ionization gages, three glass envelope gages (located in the test volume), and a single nude gage located behind the GHe shield in the front of the chamber (Fig. 1). The gage mounted on the top end of the antechamber was directed downstream along the plume axis, and the gage at the bottom of the chamber faced in the opposite direction toward the GHe shield panel. The third gage in the test volume was attached to a mechanical

feedthrough rod which allowed it to be translated parallel to the plume axis and rotated about its axis.

2.2 FIVE-lbf THRUST ENGINE AND PROPELLANT SYSTEM

The five-pound thrust bipropellant engine (AJ10-181) was developed for the Air Force by the Aerojet Corporation. The engine was designed to operate on nitrogen tetroxide (N_2O_4) oxidizer and monomethylhydrazine (MMH) ($CH_3N_2H_3$) fuel at a mixture ratio of 1.6 lb N_2O_4/1 lb MMH at propellant supply temperatures between 20 and 120°F. The engine analysis and design were based on the CONTAM computer code, which indicated that a low dribble volume multi-element injector was necessary for attaining high pulse mode performance and low contaminant generation (Ref. 7). It should be noted that contaminant in the sense stated here refers primarily to the expulsion of raw propellant (fuel or oxidizer in either liquid or gaseous form) from the combustion chamber along with the products of combustion. However, since any exhaust product of the engine is capable of contaminating a specific surface (at least in the sense of altering the surface optical or radiative characteristics) all plume gases are loosely referred to as contaminants in this report.

The baseline engine designated for this program was optimized for maximum performance with a pressure-regulated propellant feed system and a radiation-cooled, combustion chamber-nozzle. The baseline engine (AJ 10-181-2) incorporated a six-element splash plate injector (45-deg element orientation) and a 2-in.-long cylindrical combustion chamber with a 100:1 expansion ratio nozzle (Fig. 3). This engine had no firing or duty cycle limitations at combustion chamber pressures to 110 psia (4-lbf thrust) and could operate over a wide range of duty cycles at combustion chamber pressures up to 150 psia. A second engine operated in this program, AJ 10-181-3, employed a six-element splash plate injector with 0-deg element orientation. This design had limited steady-state operational durations that were combustion chamber pressure dependent.

Three additional combustion chamber/nozzle (thrust chamber) configurations were available for use with either engine configuration. The combinations which were used during the Bipropellant Contamination program are listed in Table 1. Each engine assembly utilized the six-element injector integrated with a torque motor-actuated/linked bipropellant valve manufactured by Moog, Inc. The thrust chambers mechanically attached to the injector were silicide-coated, columbium alloy units. The weight of the complete engine (valve, injector, and thrust chamber) was approximately 1.2 lb. Engine specifications are listed in Table 2.

The engine was installed in the 10V chamber at the location shown in Fig. 1. The engine was mounted on a traversing mechanism (sting) with flexible propellant lines which allowed it to be withdrawn into the antechamber during nonoperating periods. A schematic of the propellant supply system is shown in Fig. 4. The fuel and oxidizer run tanks, feedlines, and pressure and flow-rate measurement instrumentation were located, along with the engine, within the 10V antechamber. An isolation valve between the antechamber and 10V chamber interior provided access to the engine while the chamber was maintained at test conditions.

The flexible tubing provided for the fuel and oxidizer supply and drain lines and the GN_2 pressurization lines to the run tanks allowed movement of the propellant feed system along with the engine when the engine was inserted into firing position. Manual isolation valves were located in the supply and drain lines just exterior to the antechamber wall. The run tanks were filled from 240-in.³ supply tanks located in propellant consoles near the chamber. Approximately 20 in.³ of propellant was transferred from the supply tanks to the run tanks initially or as the run tanks became depleted during testing. The 40-in.³ run tanks were normally maintained less than 50 percent full. The GN_2 pressurization levels of the run tanks were used to control the propellant flow rates during the engine firings. The propellant feedline lengths (60-in. fuel line and 33-in. oxidizer line) from run tanks to engine were sized to reduce the engine mixture ratio variation on bipropellant valve opening (Ref. 7). The instrumentation used for propellant system and engine parameter measurements is given in Fig. 4. The engine was operated by a millisecond (ms) sequencer which could be programmed for any electrical pulse width (EPW) from 1 to 9,999 ms, any pulse interval from 1 to 9,999 ms, and from 1 to 9,999 pulses.

2.3 DIAGNOSTIC INSTRUMENTATION

2.3.1 Quartz Crystal Microbalances

In the planning stage of this program, the intent was to use a QCM design which had performed successfully in the Jet Propulsion Laboratory (JPL) Molsink chamber for monopropellant thruster contamination study (Refs. 8 and 9). After the JPL designs were reviewed, it was evident that extensive modifications would be necessary to adapt the "low temperature" units which had been used to measure "far-field" contamination. To meet the requirements of this study, additional QCM's of the "variable temperature" design used by JPL to measure the mass flux within 30 deg of plume centerline were needed.

To determine the necessary design changes, one of the JPL variable temperature QCM's was operated in a small cryogenic vacuum chamber at AEDC. In the present AEDC version (Fig. 5) the electronics package is insulated from the mounting and independently

temperature controlled at near room temperature. The crystal is mounted on a temperature-controlled heat sink connected to the QCM mounting block by a thermal conductor sized to allow 20 to 300°K temperature cycling in one hour with a heater power of 10 W. With these two modifications, the QCM can be clamped to a constant low-temperature 20°K heat sink, the crystal temperature controlled anywhere between the heat sink temperature and 300°K, and the oscillator electronics maintained at room temperature.

Crystals from some original JPL units were used, and additional crystals were purchased from the same vendor. Three of the crystals were cut at 39°49' for a low-temperature coefficient in the 77°K range; the remaining nine were cut at 40°28' for the range less than 40°K. The oscillator and mixer circuit was modified by adding an output stage with a gain of ten to improve the S/N when the QCM's are operated on long cables.

A field-of-view (fov) limiting aperture was added to the cover plate on all QCM's except one, to reduce the fov to approximately $2\pi/12$ sr (48 deg full angle) and thereby to reduce the molecular flux reaching the crystal from directions other than the nozzle. The QCM without an fov-limiting tube was located at 90 deg from plume centerline adjacent to the cooled germanium substrate and used in conjunction with the IR transmission measurements.

Crystal temperature was taken to be that measured by a thermocouple imbedded in the heat sink to which the crystal was mounted. The temperature of the QCM surroundings was less than 80°K, excluding the thruster nozzle directly in the fov, and as a result there was a low radiation exchange between the QCM and its surroundings, and the crystal temperature was calculated to be within 0.1°K of the heat sink temperature.

Eleven QCM's were installed in the chamber by clamping them to a stainless steel cryogenic line at various locations to achieve angles (ϕ) of between 25 and 147 deg from the plume centerline to the QCM's (Table 3). With two exceptions, the QCM's were always pointed at the nozzle; QCM No. 1 (ϕ = 118 deg) was pointed downstream parallel to the plume centerline, and QCM No. 9 (ϕ = 62 deg) was pointed downstream toward the center of the LN_2 shield (Fig. 1). Neither of these QCM's had a geometrical view of the nozzle; this setup was used to enable measurement of backscattered flux during firing, from directions other than the nozzle or the antechamber door, and to determine whether significant backscattering from the plume and the cryopanels occurred.

The cryogen line to which the QCM's were clamped was cooled with nominal 20°K GHe, allowing the QCM crystal temperatures to be controlled from approximately 25 to 300°K. Several operating temperatures above 25°K were chosen in an attempt to selectively collect

particular plume species. When all of the QCM crystals had stabilized at the desired temperature, a set of QCM frequencies and temperatures was recorded; this was usually about ten minutes prior to the beginning of a sequence of engine firings. A second set was recorded just prior to the engine firing, and a third set just after the firing sequence. If the data sets are designated 1, 2, and 3, respectively, the measured mass flux, I, is

$$I = \frac{dm}{d\Omega} = \frac{K R^2 \Delta f}{N t_p}, \text{ gm/sec-sr} \tag{1}$$

where $\dot{m}$ = mass rate collected by QCM, gm/sec

Ω = solid angle subtended by the QCM fov, sr

K = QCM calibration constant = 1.77×10^{-8} gm/cm^2 $-$ Hz

R = distance from nozzle exit to QCM crystal, cm

$$\Delta f = f_e - f_2 - \left(f_2 - f_1\right) \frac{t_3 - t_2}{t_2 - t_1}, \text{ Hz} \tag{2}$$

N = number of engine firing pulses

t_p = pulse length, sec

t_i = time at which data were recorded, sec

f_i = QCM beat frequency

The second term in Eq. (2) was used to eliminate the chamber background mass flux at each QCM location.

During the firing sequence, QCM frequencies were monitored with a frequency-to-voltage converter and a strip chart recorder. When one or more QCM's stopped oscillating due to mass saturation, normally at frequencies between 50 and 100 KHz, the crystals were heated to 300°K to remove the deposit. This process of cleaning the QCM crystals required a maximum of one hour.

2.3.2 IR Transmission

A schematic of the experimental apparatus showing the IR interferometer (Digilab Model FTS-14), the two laser beams, the high vacuum chamber (10V) containing the cryocooled QCM (No. 4) and germanium window, and the IR source location is given in Fig. 6. For the bipropellant engine the exhaust products were collected at an angle of 90 deg (see Table 3) from the plume axis centerline and at a distance of 82 cm along the nozzle exit plane. Normal absolute transmission spectra were measured using 26°K germanium as a substrate material. To minimize the 300°K background radiation seen by the spectrometer a cold stop was located in the "back-of-window" gas baffle. This stop was 1.50 in. in diameter, and the clear aperture of the germanium was 2.0 in. in diameter. Gas was prevented from condensing on the back of the germanium window by a baffle positioned close to the back of the window holder; this baffle also held the optical stop.

The spectral resolution of the interferometer system could be selected between 16 and 0.5 cm^{-1}, but 4 cm^{-1} resolution proved to be sufficient for the low temperatures where all rotational structure was eliminated. The wavenumber accuracy of the interferometer is about 0.005 cm^{-1}, limited only by the uncertainty in the optical path difference monitored by the auxiliary helium-neon (He-Ne) laser interferometer. Transmission data were recorded in the 500- to 3,500-cm^{-1} region using a pyroelectric detector. Transmission measurements were performed by rotating the germanium out of the beam and recording and storing a reference power spectrum. Thirty-six 36 interferograms were generally co-added before execution of the Fourier transform, thereby improving the S/N ratio. Next the window was rotated into the beam and the process repeated. The reference file was then divided into the sample file via a NOVA 4001 minicomputer and the ratio plotted by a digital incremental plotter, producing the final data record on a linear ordinate scale of zero- to 100-percent transmission; these data were also stored on digital tape for further processing by an IBM 370/165 computer to determine optical properties from the transmission data.

The IR transmission of condensed exhaust products collected on the 26°K optical substrate (germanium) was used to provide in situ identification of species deposited on the QCM's and to determine optical properties of the condensed exhaust gages (Ref. 10). The QCM located directly below the substrate was kept at the same temperature and was used in conjunction with the IR transmission measurements and the laser interference measurements to obtain the deposit density and thickness. A theoretical model of substrate plus film transmission was developed and subsequently employed with the experimental results to determine the complex refractive index ($\bar{n} = n - ik$) of the cryopumped exhaust constituents. The subtractive Kramers-Kronig treatment for calculation of the film refractive index was also employed, and the results were compared to those of the nonlinear least squares determination.

2.3.3 Two-Angle Laser Interference

A two-angle laser interference technique was employed to measure the film thickness and also the film refractive index at 0.6328 μm (Ref. 10). Basically, two He-Ne laser (2 mW) beams (Fig. 6) were specularly reflected off the germanium window at different incidence angles (accurate to within 0.5 deg). As the exhaust gases were condensed, two interference fringes of different periods were observed on silicon solar cell detector outputs used to measure the intensity of reflected laser light. If the ratio of fringe periods is termed β, the refractive index of the film is given by

$$ n = \frac{\left(\sin^2 \theta_b - \beta^2 \sin^2 \theta_a\right)^{1/2}}{\left(1 - \beta^2\right)^{1/2}} \tag{3} $$

where θ_a and θ_b (typically 2.5 and 62.5 deg) are the two laser beam incidence angles. Once n has been established, the thickness d_1 of the film is readily calculated from $m_a\lambda = 2nd_1 [1 -(\sin^2\theta_a/n^2)]^{1/2}$, where m_a is the order of the interference maxima for incidence angle θ_a. A QCM was used in conjunction with the two-angle laser technique to determine the density of the condensed exhaust products. The laser beams were incident on the center of the same optical substrate used for the IR transmission measurements and thus provided properties for the same deposit.

2.3.4 Thermovision (Infrared Scanning Camera)

An AGA Thermovision Model 680 was employed for flow visualization purposes. The data recorded were spectrally filtered with a narrow band CO_2 filter (4.21 - 4.41 μm). The IR scanning camera was equipped with an InSb (indium antimonide) detector and an 8-deg fov lens. Data were recorded for several 1-sec firings at the rate of 16 frames (fields)/sec. Peripheral equipment included a color monitor and a video disk recorder. The IR viewport window was NaCl (sodium chloride); IR camera data were recorded from the side viewport of the 10V chamber. The flowfield viewed with the 8-deg fov lens covered the end of the exhaust nozzle and about 12 in. of the exhaust plume.

2.3.5 Solar Cell Test Apparatus

A solar cell test array was arranged in the 10V chamber to determine the degree of degradation during the series of engine firings. The array, shown in Fig. 7, consisted of five

silicon solar cells and five selenium solar cells mounted internal to the vacuum chamber and two silicon solar cells mounted behind a glass window outside the chamber. All the solar cells were temperature controlled to 300°K since their response is temperature sensitive. The silicon solar cells (Vactec VTS 3020) were 0.4 in. square; the selenium cells (Vactec 157201 AJGH) were 0.65 x 0.75 in. The two external silicon cells were also made by Vactec and were 0.2 in. square. The radiation source was an Optical Radiation Corporation (ORCON) 1600-watt xenon lamp with a focusing attachment for varying the beam size and intensity. The solar simulator was positioned on a tripod outside the chamber with the solar beam passing through a quartz window in the chamber wall to the solar cells. Unfortunately, the simulator had to be removed after each series of measurements because it was located in a walkway. Efforts were made to place it in the exact position each time measurements were made, but there were slight variations in position. The same power level settings and focusing position were maintained throughout the program. The intensity of the solar output lamp was measured and found to be 117 W/cm^2, which is 0.86 solar constant. The spectral output of the xenon lamp is shown in Fig. 8 along with the Johnson curve of solar spectral energy.

Data acquisition of the solar cell contamination data was performed automatically using a system built around a Digital Equipment Corporation microprocessor (MPS) system. The MPS served as a programmable sequencer for scanning the array of solar cells while their loads were varied. Loads were resistive, with the same load being presented to solar cells of the same type. Data were recorded on a strip chart recorder.

2.3.6 Attenuated Total Reflectance Plates

Of primary interest in the Bipropellant Contamination program was the extent to which, if any, droplets of raw fuel or oxidizer, or any liquid or solid residues of the combustion process, might be ejected from the nozzle into the plume backflow region. It was postulated that noncombustion propellants could flow from the combustion chamber along the thrust chamber wall to the nozzle lip, where they would be entrained in the nozzle boundary-layer flow expansion and travel outside the normal Prandtl-Meyer expansion angle into the backflow region. One of the methods utilized in attempting to determine whether this process occurred, and possibly the extent to which it occurred with the 5-lbf thrust engine, was total internal reflection spectroscopy.

Three Attenuated Total Reflectance Plates (ATR's) were installed in the plume backflow region. One was mounted on the engine mount sting just below the engine attachment point (Fig. 3), and two were attached to the end of a rod which extended through a penetration at the front of the 10V chamber into the backflow region. The ATR plates could be installed in

the backflow region and also removed from this region and the chamber by the use of a small vacuum valve on the chamber penetration. The ATR plates were maintained near ambient temperature during the time they were in the chamber by means of a temperature-controlled resistance heating element bonded to the end of the rod. The ATR plates were installed back-to-back on the attachment surface, one plate installed to directly face the nozzle, the other as a control to face away from the nozzle.

The ATR plates used in this program were of KRS-5 material roughly 50 by 20 by 2 mm thick with a 45-deg angle chamfered on each of the 50-mm-long ends of the plate. A beam of radiation normally incident on the 45-deg face will undergo approximately 25 internal reflections as it passes through the plate and exits at the opposite end, normal to the other 45-deg face. All beam energy is internally reflected when the angle of incidence at the edge of the plate (45 deg) is greater than the critical angle of the KRS-5 material (24 deg). Although all of the energy is reflected, the radiation beam penetrates slightly beyond the reflecting surface and then returns. When a coating of material which selectively absorbs radiation is in contact with the reflecting surface of the KRS-5 plate, the beam will lose energy in these absorption bands. The attenuated radiation, when measured and plotted as a function of wavelength by a spectrophotometer, allows the absorption characteristics of the coating to be determined. Since the incident beam does not enter the plate as parallel rays, discrete reflections quickly disappear and the entire area of the plate is sensitive to the coating, so that the coating does not have to be dispersed over the surfaces, and even small droplets on the surface will influence the absorption measurement (Ref. 11).

The ATR plates must be removed from the chamber for analysis in a spectrophotometer operated at ambient conditions. A double-beam-recording infrared spectrophotometer, operating over the spectral range from 2 to 15 μm, was used to make the laboratory measurement of ATR plate transmission. A clean control plate was placed in the reference beam of the spectrophotometer during the measurement process to eliminate an overlay of atmospheric absorption bands on the film transmission characteristics.

2.3.7 Reactive Coated Witness Plates

Small witness plates were installed in the test chamber prior to each test run. These plates consisted of a 1/2-in.-diam microscope cover glass slip cemented to the surface of a standard scanning electron microscope (SEM) sample holder. These samplers were vacuum coated, some with a thin layer of pure copper, others with aluminum to form a reactive surface. They were located in the test chamber both in the forward flow region and in the backflow region with their reactive surface facing the rocket motor. Their prime purpose was to intercept any small droplets of fuel or oxidizer. These droplets would then react with the

17

copper or aluminum, leaving a permanent mark which later could be analyzed to determine the probable size and composition of the droplet. Some witness plates were located in the test chamber prior to pumpdown and were recovered after several thousand engine pulses. Others were inserted into the backflow region via a vacuum lock and thus were recovered after a series of engine pulses. One witness plate was located under the engine mount and slightly behind the exit plane of the nozzle for each engine configuration.

2.3.8 Photography

A 35-mm sequence camera was installed on the access door viewport of the test chamber. It was fitted with a 200-mm lens and a 250-exposure magazine. Illumination was provided by an electronic flash lamp. The camera shutter and the electronic flash were triggered independently to avoid possible timing variations caused by the mechanical shutter release. In a typical run sequence, the camera shutter was opened just prior to each engine firing and the electronic flash was operated through a variable time delay. This delay was set at zero for the first engine pulse, and succeeding shots were taken at 10-msec intervals. The resulting photographs thus represented time sequences from engine start through engine shutdown.

2.3.9 Mass Spectrometer Installation

A quadrupole mass spectrometer was installed on the 10V chamber to serve as a vacuum monitor. Its prime purpose was to determine the composition of the background gases during the initial pumpdown and between engine firings. The mass spectrometer was mounted external to the test chamber; however, there was an internal 2-in.-diam tube which penetrated the cryoliner so that it was sampling gases from behind the rocket motor.

3.0 TEST DESCRIPTION

The primary test volume in which plume measurements were made was a cylindrical volume approximately 6 ft in diameter and 6 ft deep (Fig. 1). This volume was bounded by the front face of the antechamber, the GHe-finned tubes around the chamber walls, and the LN_2 shield in front of the LHe pump. No test hardware which would interfere with the expanding plume was installed in this volume.

The engine mount sting was normally positioned approximately 12 in. in front of the antechamber valve, as shown in Figs. 1 and 3. The engine was translated within ±6 in. of this position for specific diagnostic instrumentation measurements.

The 10V chamber is large enough to allow the engine to be fired and a high background altitude to be maintained throughout the test volume. As the exhaust gases expand into the

chamber, a large fraction of the total mass flux is contained within the Prandtl-Meyer expansion angle, which for this test was approximately 45 deg from the plume axis. The cryopumping system removed these gases with only a very small portion entering the volume behind the engine.

The region outside the Prandtl-Meyer expansion angle experienced a pressure rise during firings as a result of engine flow into the region and the limited cryosurface available. The LHe cryopump behind the engine removed these gases during pulse firings at a rate that maintained the pressure in this region below 1×10^{-5} torr. The gas flow to the backflow region was expected to arise from nozzle boundary-layer gas (and possible liquid droplets) expanding around the nozzle lip. The plume diagnostic measurements were primarily made outside the Prandtl-Meyer expansion angle in a region where the present CONTAM code predicts zero mass flux.

There was an effort in the program planning phase to take advantage of all noninterference-type diagnostic methods available for studying plume contamination. These diagnostic techniques were selected both for a specific purpose and also to complement the other techniques. For example, the QCM, the condensed phase IR transmission, and the laser interference techniques combined to provide information which none in and of itself could produce. The two-angle laser interference technique measured the thickness of a thin film of condensed exhaust products on a cryogenically cooled optical substrate. When this thickness is combined with the mass of the cryodeposit measured by the QCM at the same temperature as the optical substrate, the cryodeposit density is obtained. The condensed phase IR transmission coupled with the laser thickness measurement yields the optical properties n (index of refraction) and k (absorption index) of the deposit. Finally, the IR transmission spectra permitted identification of the IR active species collected by the substrate.

Five engine configurations (Table 1) were fired over a wide range of parameter variations. The baseline operating conditions and parameter variations from these conditions are listed in Table 4. The parameters varied were chosen to reveal any effects these variables might have on the mass flux distribution and/or contaminant levels in the plume. Varied parameters included oxidizer-to-fuel ratio (O/F), duty cycle (DC), combustion chamber pressure (P_c), and electrical pulse width (EPW).

Table 5 summarizes the measurements performed on each engine configuration. The QCM data are complete for all configurations but are somewhat limited on configurations C and D. Coverage of the in situ IR transmission and laser interference measurements was also thorough. Extensive IR transmission measurements were not made on configurations A and C.

4.0 DATA PRESENTATION AND DISCUSSION

4.1 ENGINE PERFORMANCE

The 5-lbf bipropellant engine operating parameters were established during the course of the test program with 1-sec duration engine firings. These firings were made prior to starting a pulse series in order to properly adjust the fuel and oxidizer run tank pressure levels to obtain the desired combustion chamber pressure and mixture ratio. The initial run tank pressure settings were established using line pressure settings obtained from Ref. 7. Usually two or three 1-sec firings were required to verify the correct P_c and O/F ratio, due to feedline pressure losses encountered which required minor adjustments of the run tank pressure levels. The conditions established for the 1-sec firings were then used for subsequent pulse series. Figure 9 is a typical record of P_c and fuel and oxidizer flow rate.

It is evident from Fig. 9 that propellant flow rate measurement failed to stabilize during the 1-sec firing. The response of the flowmeter signal conditioners may have been too slow to adequately measure the flow rates during the 1-sec firings. The measured values of fuel and oxidizer flow rate were normally 7 to 10 percent lower than the predicted steady-state levels. The few firings of durations longer than 1 sec indicated better agreement with calculated values. Although the measured values of flow rate were lower than predicted, both fuel and oxidizer flows were lower by about the same fraction of measured flow; therefore, the measured values of mixture ratio agreed well with the predicted values.

Combustion chamber pressure response for 100-msec and 25-msec pulse firings is also shown in Fig. 9. The pressure rise and decay for the conical combustion chamber (configuration D) is somewhat slower than for other configurations, but otherwise the P_c response shown in this figure is typical.

4.2 CHAMBER PERFORMANCE

The base pressure achieved in the 10V chamber prior to the start of the engine firing sequences was 2 to 3 x 10^{-6} torr. This base pressure was reached with all cryogenic systems at their operating temperatures. This base pressure was somewhat higher than had been anticipated and was due primarily to some cryosystem leakage. This leakage provided a high background of N_2 in the chamber during portions of the program, requiring that the background mass flux level on the QCM's be measured prior to starting a test sequence when the units were at their lowest operating temperature ($\approx 26°K$). This high background also increased the tare heat load on the GHe and LHe cryopumps, but it did not otherwise affect their performance.

20

The 10V chamber pressure was recorded during all engine operations with the nude ionization gage located in the front of the chamber, between the chamber wall and the cryopanels. The gages within the test volume were operated only periodically since their operation added a significant heat load to the smaller LHe cryopump in the front of the chamber. The peak pressure measured with the nude gage ranged up to 2 x 10^{-5} torr. The number of pulse repetitions normally had little effect on the chamber performance.

4.3 RESULTS OF QCM MASS FLUX MEASUREMENTS

In this section results are presented comparing the measured mass flux per unit solid angle, I (gm/sec-sr), for the various engine configurations and operating conditions. The oxidizer-to-fuel ratio (O/F), pulse duty cycle (δ), combustion chamber pressure (P_c), firing pulse length (t_p), and QCM crystal temperature (T_x) are specified in each case. Since comparisons by inspection only are often difficult, least squares exponential curves have been computed to fit appropriate sets of data. The slopes and intercepts (in semilog representation) for these exponential curves are always listed for the varied parameter, but the fitting lines are not always shown in order to avoid confusion on the figures. Instead, a so-called "reference line" is shown on most figures; this is simply the least squares exponential fit to the data for all engine configurations at baseline operating conditions and T_x = 26°K. The equation for the reference line is

$$I = 9.49e^{-0.0752\phi} \tag{4}$$

where I is as defined in Section 2.3.1 and ϕ is the angle (in degrees) between the plume axis and the QCM location. The line serves as a point of reference on each figure and accentuates the effect of any departure from the baseline operating conditions. At the same time the slope/intercept values can be used to detect any systematic changes in the measured mass flux resulting from the varied parameters.

Also, on most figures a few backscatter measurements are shown. These backscatter measurements indicate mass flux levels collected from viewing directions other than the nozzle exit during engine firing. This flux is attributed to molecular backscattering from either the cryogenic panels or the plume itself. The QCM's (Nos. 1 and 9) making these backscatter measurements were pointed downstream toward the far end of the chamber and had no direct line of sight to the nozzle. For ease of comparison with the other QCM measurements, these backscatter data have been plotted as if the QCM's were directed at the nozzle and located at the same R, ϕ coordinates (Table 3); that is, the data are displayed as mass flux per unit solid angle rather than mass flux per unit area. The QCM locations were staggered, with about half mounted on each side of the chamber or nozzle centerline. The

21

measured flux values show no evidence of assymmetry in the plume. Therefore, the nozzle geometrical axis and the plume centerline are taken to be identical, and all QCM data are plotted at positive angles.

4.3.1 Effect of Varying Engine Configurations

Data were obtained on all five engine configurations operating at baseline conditions (see Table 5), and the results are plotted in Fig. 10. Under these firing conditions the five configurations produced remarkably similar mass flux levels and angular distributions. These combined data for the five configurations, like all the QCM mass flux measurements obtained in this program, exhibit an exponential dependence on ϕ, the angle from the plume centerline. Nearly all measured values fall within a factor of two of the exponential line fitted to the combined data points and thereby justify the use of exponential curve fitting. In addition to the curve fitted to the combined data, slopes and intercepts are listed in Fig. 10 for the exponential curves fitted to the data for each engine configuration. The general conclusion drawn from Fig. 10 is that these measurements reveal no significant differences in the mass flux distributions for the five engine configurations tested. The only QCM data recorded for configuration C are shown in Fig. 10.

4.3.2 Effect of Varying Engine Operating Conditions

Figures 11, 12, and 13 show the results of varying the oxidizer-to-fuel (O/F) ratio (1.4 to 1.8), the duty cycle (1 to 10 percent), and the combustion chamber pressure, P_c (75 to 127 psia) for the baseline engine configuration. No pronounced effects on the measured mass flux are apparent. In fact, with respect to O/F ratio, duty cycle, and P_c, Eq. (4) (reference line) appears to fit all of the data in these figures within a factor of two. There is an indication in Fig. 13 that the mass flux at angles of less than 60 deg increased with high P_c as predicted by inviscid flow-field calculations. That is, the measured (or predicted) mass flow increases approximately 60 percent during a P_c change from 75 to 125 psia. This increase is not reflected in the mass flux measurements at the QCM locations outside 60 deg (Fig. 13), which indicate only a 20- to 30-percent increase. This indicates that the linear mass flux increase may not occur in the backflow region as it does with the total flow.

Figure 14 illustrates the effect of varying the firing pulse length from 25 msec to 1 sec for several engine configurations. Inspection of either the listed slopes/intercepts or the plotted points reveals a general increase in the measured mass flux as the pulse length decreased. The increase was less than a factor of two but was quite reproducible for all engine configurations. The essentially constant slope and changing intercept indicate that the effect does not depend on angle. This effect is partially the result of using the electrical pulse width

as the time scale. If the actual pressure transducer traces are used, then the time lag for the valve closings is greater than the time lag for valve openings. Thus the pulse widths are actually greater than the electrical pulse widths. If this time scale (not electrical pulse width) is used, then the extra time of each pulse is a greater fraction of the shorter pulse widths. The net results would be to cause the data spread to collapse onto essentially one straight line. On this basis, the conclusion is that the mass flux is primarily a function of actual engine firing time; however, if the electrical pulse width is used, then it would appear that the engine ignition and shutdown are the primary factors controlling mass flux.

4.3.3 QCM Temperature Variation

Figure 15 compares the mass flux collected at the various QCM operating temperatures. In this figure the fitted exponential lines are shown explicitly. The fitted line intercepts decrease in a well-behaved and predictable manner as the crystal temperature (T_x) increases, indicating that fewer exhaust species were cryopumped at the higher temperatures. Notice the sharp drop (about two orders of magnitude) in collected mass flux when the crystal temperature increases from 140 to 200°K. The species collected at $T_x \geq 180°K$ are probably products of incomplete combustion, since no major bipropellant combustion products should condense at such high temperatures.

Using the data from Fig. 15 one can calculate the relative mass fraction condensed at each QCM temperature. This is illustrated in Fig. 16, where relative condensed mass fraction versus crystal temperature is plotted. In Fig. 16 there are sharp jumps in the condensed mass at the temperatures where H_2O and N_2 condense (165°K and 30°K), but there is no similar jump in the curve at 86°K, where CO_2 condenses. This is caused either by cryosorption of CO_2 by previously cryopumped species or by trapping of CO_2 as other species condense at higher temperatures.

4.3.4 Chamber Background Pressure

The importance of a sufficiently long mean free path to the measurement of mass flux in the plume backflow region was recognized. A reduced mean free path resulting from an increase in vacuum chamber pressure during a firing sequence could invalidate the measurements. To determine the effect on the QCM data, the chamber pressure was systematically increased by adding helium. The QCM data obtained during these stepwise increases in chamber pressure are presented in Fig. 17, where the tabulated pressures (P_{He}) take into account the gage factors for hydrogen and helium. The lowest pressure listed was the case before the addition of helium began, and the residual gas was assumed to be mostly hydrogen. There was no significant change in the QCM data after the first increment of

23

helium was added. Further increases in chamber pressure up to 8.4×10^{-4} torr, a factor of approximately 100 times the lowest pressure, caused a factor of about three decrease in the collected mass flux. Finally, when the chamber pressure was increased to 4.2×10^{-3} torr, the results became very erratic.

4.3.5 Comparison with Analytical Predictions

As pointed out in the Introduction, CONTAM does not incorporate a boundary-layer model and, therefore, does not expand the flow field properly to predict mass flux in the backflow region. It would seem then that the most worthwhile qualitative assessment to make here is to compare the experimental data to both an inviscid model and a boundary-layer model. Such a comparison could be of value in providing direction to upcoming model improvement efforts. For the inviscid model prediction it is convenient to use the cosine law approximation (Refs. 6, 12, and 13) to the method of characteristic (MOC). For the boundary-layer model Simons (Ref. 13) has developed simple closed-form expressions for Boynton's numerical treatment (Ref. 14) of the supersonic portion of the nozzle boundary layer. It should be clearly understood at the outset that these are only first-order estimates for the purpose of comparison.

Boynton's work suggests that at large angles from the nozzle axis the plume gas density obeys an exponential decay law. Based on Boynton's results, Simons (Ref. 13) assumed that the cosine law is valid for angles less than some angle ϕ_0, and that the exponential applies for angles greater than ϕ_0, where ϕ_0 is the turning angle for the streamline at the edge of the boundary layer. Using this approach Simons obtained the following analytical forms for the gas density distribution:

$$f(\phi) = \cos^{2/(\gamma-1)}\left[(\pi/2)\left(\phi\Big/\phi_\infty\right)\right] \text{ for } \phi < \phi_0 \tag{5}$$

where γ is the ratio of specific heats and ϕ_∞ is the value of the limiting turning angle for an inviscid supersonic flow.

$$f(\phi) = f\left(\phi_0\right) e^{-\beta\left(\phi - \phi_0\right)} \text{ for } \phi > \phi_0 \tag{6}$$

where ϕ_0 and β are functions (Ref. 13) of the nozzle exit conditions, and ϕ_0 is related to the boundary-layer thickness (δ_e) through

$$f\left(\phi_0\right) = \left(2\delta_e\Big/R_e\right)^{2/(\gamma+1)} \tag{7}$$

where R_e is the nozzle exit radius.

24

For evaluating Simons' equations, the appropriate parameter values for the 5-lbf thruster (baseline configuration) were determined to be

Ratio of specific heats, $\gamma = 1.25$

Effective nozzle area ratio, $A_e / A_t = 84$

Exit Mach number, $M_e = 5.2$

Combustion chamber pressure, $P_c = 100$ psia

Combustion chamber temperature, $T_c = 2,500^\circ K$

Then the numberical values of Simons' parameters are

$$\phi_o = 22.06 \text{ deg}$$

$$\phi_\infty = 75.8 \text{ deg}$$

$$f(\phi_o) = 0.42$$

$$\beta = 8.93$$

$$\delta_e / R_e = 0.188$$

The resulting mass flux distributions predicted by the inviscid and boundary-layer models are plotted in Fig. 18 with the experimental data, Eq. (4), for comparison. As expected, the inviscid prediction falls off much too fast. The boundary-layer prediction also decays too rapidly. The slope $\beta = 8.93$ for the predicted exponential curve is a factor of two higher than for the measured data.

4.3.6 Uncertainty of Mass Flux Measurements

The uncertainty (U) of the mass flux measurement I (gm/cm²-sr), the maximum error that might reasonably be expected, is defined (Ref. 15) as

$$U = \pm \left(B + t_{0.95} S \right) \tag{8}$$

where B is the bias limit or systematic error in the measurement process, S is the precision error index (a function of the random error in the measurement process), and t is the 95th percentile point of the two-tailed Student's "t" distribution. The mass flux, I, has been defined in Section 2.3.1 as

$$I = \frac{K R^2 \Delta f}{N T_p} \tag{9}$$

The precision error and bias limits for the mass flux are calculated using the Taylor series expansion to approximate the effect of the errors in the measured values of the quantities. The precision error and bias limit of the mass flux I are given, in terms of the precision error and bias limits of the individual quantities, as

$$\frac{S_I}{I} = \left[\left(\frac{S_K}{K}\right)^2 + \left(\frac{2S_R}{R}\right)^2 + \left(\frac{S_{\Delta f}}{\Delta f}\right)^2 + \left(\frac{S_N}{N}\right)^2 + \left(\frac{S_{T_p}}{T_p}\right)^2 \right]^{\frac{1}{2}} \tag{10}$$

$$\frac{B_I}{I} = \left[\left(\frac{B_K}{K}\right)^2 + \left(\frac{2B_R}{R}\right)^2 + \left(\frac{B_{\Delta f}}{\Delta f}\right)^2 + \left(\frac{B_N}{N}\right)^2 + \left(\frac{B_{T_p}}{T_p}\right)^2 \right]^{\frac{1}{2}} \tag{11}$$

The precision index of the mass flux measurement, I, is best estimated from the mass flux measurements made during the program rather than from precision error estimates of the individual quantities, even though there were insufficient data at identical test conditions to provide a meaningful statistical base. Several sets of data which include variations in test conditions that did not strongly affect the measured results were used to estimate the precision error. These were measurements on engine configuration A at six QCM angles. Five firing sequences were anlayzed with the QCM's operating at 25°K. The relative standard deviation at each angle ranged from 5.9 to 10.49 percent. The precision index of the QCM measurements is therefore estimated at ± 10 percent. The degree of freedom is taken as the number of firing sequences analyzed, five.

The uncertainty, U, is then:

$$U = \pm \left(B + t_{0.95} S \right) = \pm [B + 2.57 (10)] = \pm (B + 25.7) \%$$

A calibration program on the QCM's was conducted following the test. The calibration program compared a calculated calibration constant based on crystal properties with a calibration constant experimentally determined by operating the QCM's in a molecular beam. The experimental value was 20 percent higher than the calculated value, and on the basis of these results the bias limit (B_K) for the QCM calibration constant has been assigned a value of ± 20 percent. Using this bias limit, one finds the uncertainty to be

$$U = \pm \left(B_K + 25.7 \right) \% = \pm (20 + 25.7) \% = \pm 45.7 \%$$

26

4.3.7 QCM Summary

1. The cryogenic chamber provided an adequate simulation of space operating conditions and had no significant effect on the plume flow field or the mass flux collected by the QCM's.

2. The QCM design modifications (thermally separated electronics) permitted reliable operation at 26°K.

3. Variation of engine configuration had no significant effect on the mass flux distribution.

4. Variation of engine operating conditions, with the exception of pulse length, had no significant effect on the mass flux distribution.

5. The QCM data show a smooth exponential mass flux distribution at angles greater than 30 deg from the plume axis. At 26°K all the data can be well described by Eq. (4), which permits a simple empirical expression for design purposes.

6. With pressure (P_c) traces used to determine pulse width, the mass flux appears to be a function of total engine "on" time and not a strong function of ignition and shutdown. If the electrical pulse width is used to define pulse width, then the shorter pulse width yields higher mass flux.

7. The mass flux decreased with increasing crystal temperature, T_x, as expected. About half the total mass flux is cryopumped for $T_x = 75°K$, and the other half for $T_x = 25°K$.

8. Comparison of theory with the QCM data shows that more work is required to account for the boundary-layer expansion into the backflow region; the current theoretical predictions are too low.

4.4 IR TRANSMISSION

The infrared (IR) transmission apparatus was used to (1) identify the plume exhaust species which cryopumped in the backflow region at 26°K; (2) identify any contaminants formed on the cell IR windows during the course of the test; (3) identify the deposition temperature of various species in the temperature range from 200 to 26°K; (4) determine the optical constants (n,k) of the deposit at 26°K; and (5) identify the gas species which sublimated from the chamber cryopanels during chamber warmup.

4.4.1 Identification of Species

4.4.1.1 IR Identification of Species Condensed at 26°K

IR transmission was used as a species identification diagnostic for the exhaust constituents cryopumped at 26°K. The results shown in Fig. 19 correspond to a 3.62-μm-thick deposit condensed initially at 26°K with spectra then recorded during the ensuing warmup. The range of temperatures shown in Figs. 19a through c corresponds to the temperatures at the beginning and end of each scan as the germanium surface was allowed to warm. This warmup was recorded for the BL configuration after the data for determining optical properties were recorded. Exhaust products were cryopumped on the germanium substrate located at 90 deg to the nozzle centerline (Fig. 6) at the nozzle exit plane. The deposit initial thickness for the data presented in Fig. 19 was 3.62 μm at 26°K; the refractive index was 1.34, and the density was 0.77 gm/cm^3. The major constituents were H_2O, CO_2, N_2 (see Section 4.5), and N_2O_4 with trace amounts of some form of nitrate, CO, NO, N_2O, NO_2, and N_2O_3.

The spectral bands found in Fig. 19 are identified in Table 6. The ν_2 band of CO_2 is located at 665 cm^{-1}. A broad band found between 700 and 860 cm^{-1} was assigned to two species, H_2O and N_2O_4. The N_2O_4 ν_{12} band is located at 750 cm^{-1}, and the H_2 band has been observed to peak at approximately 780 cm^{-1} at 26°K although it is relatively broad (770 to 920 cm^{-1}. The next band, at 1,275 cm^{-1}, is the N_2O_4 ν_{11} band.

A strong band was found at 1,310 cm^{-1}; this is a result of the (ν_{11} + R) band of N_2O_4 as identified by Wiener and Nixon (Ref. 16), N_2O_3, and the ν_3 nitrate band. Upon warmup of the germanium substrate to $\approx$ 100°K (Fig. 19b) the depth of both bands increased, but much more dramatically for the 1,275 cm^{-1} band. Both bands disappeared at $\approx$ 220°K (Fig. 19c) at a chamber pressure of 4 torr.

The next two bands are located at approximately 1,600 cm^{-1} and 1,645 cm^{-1}. The 1,600-cm^{-1} band is the ν_3 band of NO_2, and the 1,645-cm^{-1} band also matches the ν_2 band of N_2O_3 which is listed as 1,646 to 1,648 cm^{-1} by Bibart and Ewing (Ref. 17). As can be seen in the warmup data (Fig. 19b) this band (1,645 cm^{-1}) almost disappears at a temperature of $\approx$ 100°K. Only N_2O_3, N_2O, and NO sublimate at this temperature, and N_2O_3 is the only one of the three which has a band in the wavenumber region. (Note: the vapor pressure of N_2O_3 is uncertain.)

The next two bands seen in Fig. 19a are those located at 1,745 and 1,765 cm^{-1}. These two bands appear almost as one in Fig. 19a, but warmup observations at intermediate

temperatures (Fig. 19b) indicate two distinct bands. The 1,765 cm^{-1} band is strongest at 26°K, but the two bands have equal strength at $\approx$ 50°K. The strength of the 1,765^{-1} steadily decreases with temperature until at $\approx$ 135°K the 1,765 cm^{-1} band is just barely observable; at $\approx$ 165°K it is completely gone. The NO should have evaporated earlier, but it evidently was trapped by the other condensed gases. The band at 1,765 cm^{-1} began to lose strength at $\approx$ 50 to 60°K, where NO would normally begin to sublimate, and this band behaves like the NO fundamental band. The 1,745 cm^{-1} band remained up to a temperature of $\approx$ 185°K (for a chamber pressure of 1.5 torr); this was the N_2O_4 ν_9 band.

Consider the three bands located at 1,840, 1,880, and 1,910 cm^{-1}. The 1,880-cm^{-1} band is N_2O_4 which remained during warmup of the substrate to $\approx$ 185°K. The 1,840 and 1,910 cm^{-1} bands are N_2O_3 and NO, respectively. Some portion of the 1,840 cm^{-1} may also be NO. Both of these bands were observed to disappear at $\approx$ 100°K (Fig. 19b), which further indicates they are N_2O_3 and NO bands.

A series of weak bands occurs at 2,100, 2,150, 2,240, and 2,285 cm^{-1}. The band at 2,150 cm^{-1} is the ν_2 CO band. Although pure CO normally sublimates at 30 to 40°K, it is still seen at $\approx$ 100°K (Fig. 19b). This is the result of CO's being trapped in the solid matrix. In laboratory studies of mixtures involving CO trapped by other gases, CO has been observed up to temperatures of 96°K. The weak band observed at 2,240 cm^{-1} is due to a trace amount of N_2O, and it was the only N_2O band observable. The weak band at 2,285 cm^{-1} is caused by the Carbon 13 isotope ($C^{13}O_2$) band. The 2,100 cm^{-1} band is yet to be positively identified, but it could be the $\nu_1 + \nu_{12}$ band of N_2O_4, which shows up as a weak band in the gas phase.

The last two bands found in Fig. 19a are the ν_3 CO_2 band located at 2,345 cm^{-1} and the very broad H_2O band in the vicinity of 3,300 cm^{-1}. The CO_2 band (also the 665-cm^{-1} CO_2 band) was still present after warmup to about 165°K, which is considerably higher than the temperature at which pure CO_2 normally sublimates (about 115°K for a pressure of 1 x 10^{-1} torr). This is another example of more volatile gases trapped in a matrix of other constituents. Most of the H_2O sublimated in the temperature range from 209 to 214°K, although weak absorption was still apparent at 220°K (Fig. 19c).

The very small amount of CO observed in Fig. 19 indicates considerably less CO than was expected. A possible explanation is that most of the CO was contained in the central core of the exhaust plume and was cryopumped downstream of the germanium substrate, which was located in the backflow region.

In Fig. 19c the nitrate band (1,300 to 1,400 cm^{-1}) was observed even at the relatively high temperature of $\approx$ 220°K. This substance remained on the germanium and could be

driven off only when the substrate was heated to 340°K. This nitrate band is associated with N_2O_4 and was also observed during work conducted with N_2O_4 alone.

In summary, the infrared transmission of cryocooled (26°K) germanium with thin films of condensed plume exhaust gases has been determined. Infrared spectra of these condensed gases were measured in the 700- to 3,500-cm^{-1} region. The IR spectra were used to identify the exhaust constituents in the backflow region. For the 5-lbf thrust bipropellant engine the primary exhaust species in the backflow region were found to be N_2O_4, CO_2, and N_2 and N_2O; minor species were CO, NO, N_2O, N_2O_3, NO_2, and some form of nitrate (NO_3).

4.4.1.2 Identification of Species Condensed at 80°K

Similar transmission measurements of cooled germanium and contaminants from the biprop engine were made for condensates formed at 80°K as opposed to the previous 26°K temperature. Gases such as O_2, N_2, CO, CH_4, and NO would not be expected to condense at the higher temperature due to their higher vapor pressure. Gases such as N_2O, CO_2, NO_2, N_2O_4, N_2O, MMH, and possibly N_2O_3 should be the major constituents condensable at 80°K. Transmission measurement results are shown in Fig. 20 for a deposit thickness of 0.891 μm. The two narrow bands located at 2,340 and 660 cm^{-1} are the ν_3 and ν_2 CO_2 bands, respectively, whereas the broad bands observed between 700 and 900 cm^{-1} and 2,500 and 3,700 cm^{-1} are due to H_2O. A portion of the bands from 700 to 900 cm^{-1} and 2,500 to 3,700 cm^{-1} is due to H_2O. A portion of the 700 to 900 cm^{-1} (approximately 720 to 790 cm^{-1}) is due to the N_2O_4 ν_{12} band which occurs as a strong doublet band between 740 and 760 cm^{-1}, as was observed for pure N_2O_4 condensed at 77°K (Fig. 21). The remaining bands from approximately 1,110 to 2,300 cm^{-1} are due to either N_2O_4 or some of its derivatives.

The N_2O_4 bands at 1,265 and at 1,305 cm^{-1} were both observed in the bipropellant engine data obtained at 26°K (Fig. 19). At 80°K, however, the band intensities are nearly the same (Fig. 20), whereas the 1,305-cm^{-1} band was much stronger than the 1,265-cm^{-1} band for the 26°K biprop data (Fig. 19). Upon warmup to 124 to 134°K (Fig. 22), the band intensities changed with the 1,265-cm^{-1} band becoming as strong as or stronger than the 1,305-cm^{-1} band. This is the same trend for these bands as was observed for the 26°K biprop data after warmup. For pure N_2O_4 deposited at 77°K (Fig. 21) the band at 1,305 cm^{-1} was not observed at all.

The band which occurs at 1,600 cm^{-1} (Fig. 20) is the NO_2 ν_3 band which was observed in both the biprop and N_2O_4 data condensed at 20 to 26°K. The band which occurs at 1,745 cm^{-1} is the N_2O_4 band. Similarly, the band near 1,870 cm^{-1}, the $\nu_4 + \nu_5$ band of N_2O_4, was also seen in the N_2O_4 and bipropellant data for condensation at 20 to 26°K and for the N_2O_4

deposited at 77°K. The next absorption band in Fig. 20 is located at 2,090 to 2,100 cm^{-1}. This unidentified band was also observed in the 26°K biprop data but was not seen for N_2O_4 deposited at either 77 or 26°K. This may be the $\nu_1 + \nu_{12}$ band of N_2O_4 (Ref. 19), which is relatively weak even in the gas phase and may only show up when isolated within a matrix of other condensed gases. The other most probable candidate would be the ν_3 cyanogen (C_2N_2) band, which occurs at 2,150 cm^{-1} in the gas phase.

The final bands observed in Fig. 20 are a series of three weak bands between 2,100 and 2,300 cm^{-1} which occur at approximately 2,175, 2,240, and 2,280 cm^{-1}. The very weak band at 2,175 is not identified, but it remained until the deposit was warmed up to 200°K under vacuum and the N_2O_4 had already evaporated. The other two bands located at 2,240 and 2,280 cm^{-1} are attributed to N_2O and $C^{(13)}O_2$, respectively.

4.4.2 Species Deposition Temperatures

The cryogenic cooling system for the germanium substrate was cooled with nominal 20°K GHe, allowing the germanium substrate temperature to be controlled from 26°K to 375°K. Several operating temperatures above 26°K were chosen in order to selectively collect particular plume species. Shown in Fig. 23a are the results obtained after all the firings for one day (engine configuration B) with the substrate temperature held at 200°K the entire day. The only definite absorption band seen was at 1,350 cm^{-1}, which is the characteristic band of nitrates.

Upon cooling the substrate to 100°K and pulsing the engine 400 (25 msec) pulses, one distinctly observes only water (Fig. 23b) with a slight amount of cryosorption or trapping of trace amounts of other species. Further cooling to 45°K and more engine pulsing did not reveal any new bands (the NO band would be included in the 1,745-cm^{-1} band of N_2O_4).

4.4.3 Optical Properties Determination

Thus far, from the QCM data and IR transmission data, the mass flux and identification of species in the backflow region have been determined. However, these data become even more meaningful when their effect upon an actual surface can be predicted or accounted for. To account for the influence of these plume constituents as contaminants, one must know the solid condensed phase optical properties. These properties are necessary to compute the reflectance change of a surface or to compute the transmission change of an optical component. Knowing these properties can help correct for the effects of condensed plume exhaust constituents on an actual vehicle. The optical properties desired are the refractive index, n, and the absorption index, k.

In order to determine the complex refractive index ($\bar{n} = n - ik$) of the thin solid film from the transmission-versus-thickness data for wavenumbers between 700 and 3,500 cm^{-1} an analytical model of film plus substrate transmission was developed (Refs. 20 and 21). It was assumed that the germanium window acted as a thick film; thus there was no phase coherence between multiple internal reflected rays. Moreover, the real part of the germanium complex index, n_g, is known and given in Ref. 22 as

$$n_g = A + BL + CL^2 + D\lambda^2 + E\lambda^4 \tag{12}$$

where

$$L = (\lambda^2 - 0.028)^{-1}$$
$$A = 3.99931$$
$$B = 0.391707$$
$$C = 0.163492$$
$$D = -0.000006$$
$$E = 0.000000053$$

The geometry describing the transmission is shown in Fig. 24. For convenience the different layers have been subscripted 0, 1, 2, and 3, where subscripts 0 and 3 are vacuum and 1 and 2 are the thin condensed film and the thick germanium substrate, respectively. The model employed to fit the experimental results is for normal incidence only. As shown in Fig. 24, E_o is the amplitude of the incident radiation which undergoes an infinite number of multiple reflections after passing into the thin film. Following multiple reflection the total amplitude of reflected and transmitted radiation is given by B1 and E_2, respectively. When E_2 internally reflects from the back of the germanium window, it becomes A1, then C1, and again undergoes thin film multiple reflection in medium 1. This results in the rays B2 and A2, and so on. Analytically, the relationships between the amplitudes of the various waves are as follows:

$$\left.\begin{aligned}
E_2^+ &= t_{012}E_o^+ \\
A2 &= A1\, r_{210} \\
A4 &= A3\, r_{210} \\
A6 &= A5\, r_{210} \\
&\;\;\vdots
\end{aligned}\right\} \tag{13}$$

with

$$A1 = E_2^+ r_2$$
$$A3 = A2 \ r_2$$
$$A5 = A4 \ r_2$$
$$\vdots$$

$$(14)$$

with

$$C1 = t_2 E_2^+$$
$$C2 = t_2 \ A2$$
$$C3 = t_2 \ A4$$
$$\vdots$$

$$(15)$$

and with

$$B1 = r_{012} E_o^+$$
$$B2 = A1 \ t_{210}$$
$$B3 = A3 \ t_{210}$$
$$B4 = A5 \ t_{210}$$
$$\vdots$$

$$(16)$$

where t_2 is the amplitude transmission of light traveling from medium 2 to medium 3, r_2 is the amplitude reflection of light incident upon medium 3 from medium 2, r_{012} is the amplitude reflection of light which is incident from medium 0 and is reflected back into medium 0 after undergoing thin-film interference in medium 1, r_{210} is the amplitude reflection of light which is incident from medium 2 and is reflected back into medium 2 after undergoing thin-film interference in medium 1, t_{012} is the amplitude transmission of light incident from medium 0 and transmitted into medium 2 after undergoing thin-film interference in medium 1, and t_{210} is the amplitude transmission of light incident from medium 2 and transmitted into medium 0 after undergoing thin-film interference in medium 1.

33

The power transmitted through the thin-film, thick-film combination is given by

$$\xi = n_3|C1|^2 + n_3|C2|^2 + n_3|C3|^2 + \cdots \tag{17}$$

where $n_3 = n_0$ since medium 3 and medium 0 are both considered vacuum and with the constant $c/4\pi$ (c being the speed of light in vacuum) being omitted for convenience since this constant will be lost when dividing to determine the overall transmittance.

Substituting Eq. (15) into Eq. (17) yields the transmitted power as

$$\xi = n_0|t_2|^2\left[|E_2^+|^2 + |A2|^2 + |A4|^2 + |A6|^2 + \cdots\right] \tag{18}$$

Next, combining Eqs. (14) and (15) yields

$$\left. \begin{array}{l} |A2|^2 = R_2 R_{210}|E_2^+|^2 \\[2mm] |A4|^2 = R_2^2 R_{210}^2|E_2^+|^2 \\[2mm] |A6|^2 = R_2^3 R_{210}^3|E_2^+|^2 \end{array} \right\} \tag{19}$$

where

$$R_2 = |r_2|^2 \tag{20}$$

$$R_{210} = |r_{210}|^2 \tag{21}$$

$$T_2 = |t_2|^2 \tag{22}$$

When Eqs. (19) and (22) are inserted into Eq. (18), the transmitted power is given by

$$\xi = n_0 T_2|E_2^+|^2 [1 + R_2 R_{210} + R_2^2 R_{210}^2 + R_2^3 R_{210}^3 + \cdots] \tag{23}$$

where the infinite sum converges to the closed form expression

$$\xi = \frac{n_0 T_2|E_2^+|^2}{1 - R_2 R_{210}} \tag{24}$$

The transmittance is defined as the transmitted power divided by the incident power. The incident power is given by

$$\xi_o = n_o |E_o^+|^2 \tag{25}$$

and the expression for the overall transmittance is obtained by ratioing Eq. (24) to Eq. (25); i.e.,

$$T = \frac{\xi}{\xi_o} = \frac{T_2 |E_2^+|^2}{[1 - R_2 R_{210}] |E_o^+|^2} \tag{26}$$

But from Eq. (13)

$$\frac{|E_2^+|^2}{|E_o^+|^2} = |t_{012}|^2 = T_{012} \tag{27}$$

and the final result for the overall normal transmittance is given by

$$T = \frac{T_2 T_{012}}{[1 - R_2 R_{210}]} \tag{28}$$

The result in Eq. (28) is valid only when the substrate is a nonabsorbing medium. If the substrate is also absorbing (i.e., if the imaginary part of the complex refractive index of the substrate is nonzero), then Eq. (28) becomes

$$T = \frac{T_2 T_{012} \, e^{-\alpha_g D}}{1 - R_2 R_{210} \, e^{-2\alpha_g D}} \tag{29}$$

where

D = the thickness of the substrate (germanium)

$\alpha_g = \dfrac{4\pi \kappa_g}{\lambda}$ is the absorption coefficient of the substrate (germanium)

k_g = imaginary component of complex refractive index of the substrate (germanium)

λ = wavelength in vacuum

Having developed Eq. (29), which is the normal transmittance of a thin film deposited upon a thick, partially transmitting film, we must now define the expressions T_2, T_{012}, R_2, and R_{210} in terms of the optical constants of the thin film, substrate, and wavelength. The

derivation of these quantities is straightforward, although tedious, and is outlined in detail in Ref. 21. For completeness, the expressions required to evaluate Eq. (29) are listed below.

$$R_2 = |r_2|^2 = \left| \left(\frac{\bar{n}_2 - n_o}{\bar{n}_2 + n_o} \right) \right|^2 \tag{30}$$

$$T_2 = |t_2|^2 = \left| \frac{2\bar{n}_2}{(n_o + \bar{n}_2)} \right|^2 \tag{31}$$

The expressions for T_{012} and R_{210} are somewhat more complicated to evaluate and will be considered separately from R_2 and T_2. The expressions for T_{012} and R_{210} based on the work of Ref. 21 are given by

$$T_{012} = \frac{|t_a|^2 |t_b|^2 e^{-2b}}{[1 + |r_a|^2 |r_b|^2 e^{-4b} + 2e^{-2b}\{Re(r_a r_b) \cos 2a + Im(r_a r_b) \sin 2a\}]} \tag{32}$$

and

$$R_{210} = \frac{[|r_a|^2 + |r_b|^2 e^{-4b} + 2e^{-2b}\{Re(r_b r_a^*) \cos 2a + Im(r_b r_a^*) \sin 2a\}]}{[1 + |r_a|^2 |r_b|^2 e^{-4b} + 2e^{-2b}\{Re(r_a r_b) \cos 2a + Im(r_a r_b) \sin 2a\}]} \tag{33}$$

where

$$r_a = \frac{\bar{n}_2 - \bar{n}_1}{\bar{n}_2 + \bar{n}_1} \tag{34}$$

$$r_b = \frac{\bar{n}_1 - n_o}{\bar{n}_1 + n_o} \tag{35}$$

$$t_a = \frac{2\bar{n}_1}{\bar{n}_1 + \bar{n}_2} \tag{36}$$

$$t_b = \frac{2 n_o}{n_o + \bar{n}_1} \tag{37}$$

$$\bar{n}_1 = n_1 - ik_1 = n - ik = \bar{n} \tag{38}$$

$$\bar{n}_2 = n_g - ik_g \tag{39}$$

$$a = \frac{2\pi d_1 n_1}{\lambda} \tag{40}$$

$$b = \frac{2\pi d_1 k_1}{\lambda} \tag{41}$$

$$d_1 = \text{cryodeposit thickness} \tag{42}$$

and * denotes the complex conjugate. The optical constants of the cryopumped plume constituents were determined by using this analytical transmission model in conjunction with a nonlinear least squares convergence routine and the subtractive Kramers-Kronig relation between n and k. The subtractive Kramers-Kronig relation is given by

$$n(v) = n_{v_m} + \frac{2}{\pi} P \int_0^\infty \left[\frac{k(v')v' - k(v)v}{(v')^2 - v^2} = \frac{k(v')v' - k(v_m)v_m}{(v')^2 - v_m^2} \right] dv' \tag{43}$$

where v_m is a reference frequency (2,180 cm^{-1}) and P indicates the Cauchy principal value of the integral. Integration was performed using the simple trapezoidal rule; the $k(v')$ values used in Eq. (43) were those determined by the nonlinear least squares technique.

The transmission data recorded for all deposits discussed here were digitized every 2 cm^{-1}. In the determination of n, absolute transmission spectra at thicknesses (HeNe laser interference fringes) from 0 to 2.35 μm were used. For the bipropellant data, the test schedule only permitted time for the formation of ten thicknesses at 26°K and four thicknesses at 77°K; these data are shown in Figs. 25a through d and 26a through b, respectively.

Usually a minimum of 15 thicknesses is desired in order for the analytical model to converge upon a well-defined value of n. The n value appears to be primarily defined by the period of the transmission-versus-thickness curve at each wavenumber. When only a few thicknesses are obtained, the transmission-versus-thickness (for each wavenumber) curve is not well defined. It was found that for the high wavenumber (> 2,100 cm^{-1}) the analytical model had no problem in defining n; however, at the lower wavenumbers a neighborhood

37

(range) of n values seemed to equally satisfy the transmission data. The k value, which is primarily determined by the magnitude of the transmission, did not have this difficulty and was well defined over the whole spectral region (700 to 3,500 cm^{-1}). Thus, the k values were used with the subtractive Kramers-Kronig technique (Eq. 43) to compute n; these new n values were then used in the analytical model (along with the k values) to see if good agreement occurred with the transmission data. For all wavenumbers the Kramers-Kronig n's along with the least squares k's yielded excellent agreement when the analytical model and transmission data were compared. The optical constants for the condensed plume constituents at 26°K associated with the BL configuration are shown in Fig. 27.

The optical properties presented are important for calculating the effects of possible deposits upon cryogenically cooled surfaces. Such surfaces as cryogenically cooled sensor optics and telescopes will be functioning in the wavenumber region investigated. The interpretation of information from these types of instruments, when contaminated with thin films, will require spectral knowledge of n and k. Shown in Fig. 28 are the transmission-versus-thickness curves at a variety of wavenumbers for the 26°K data. The excellent agreement between theory and data is typical of the results obtained over the entire spectral region from 700 to 3,500 cm^{-1}. Figure 28 illustrates the good agreement between theory and data at both high and low wavenumbers and in regions of high absorption.

4.4.4 Gas Phase Transmission Data

During the chamber warmup the germanium substrate was rotated out of the IR beam, enabling the 10V chamber to be used as a large absorption cell for identifying the gas species which sublimated during chamber warmup. Each gas spectrum in Fig. 29 was recorded with the Fourier transform spectrometer at a resolution of 1 cm^{-1} and by coadding 64 scans; these data also correspond to engine configuration B. Also, each spectrum was normalized by the spectrum recorded while the chamber was cold and pumped down to 10^{-6} torr. The chamber pressure (torr), the GHe panel temperature, and the LN$_2$ panel temperature are shown at the lower left-hand corner of each scan. The chamber was allowed to warm up at its own rate without additional heat although at 48 mm the chamber was pressurized up to 500 mm with dry N$_2$ gas, which did provide extra heat. The LN$_2$ panels warmed more slowly than the GHe panels because of the remaining liquid nitrogen in the lines, which required more heat to evaporate.

In Fig. 29a, CO was immediately observed as the temperature of the GHe panels reached 55°K. The strong CO band indicated a significant volume of CO evaporated during warmup; however, in the backflow region only a trace amount of condensed CO had been detected in the 26°K IR spectrum. When the GHe panels were warmed to 105°K (Fig. 29b), methane (CH$_4$) was clearly seen along with a trace amount of CO$_2$. Methane, although seen here in the gas phase, was not detected in the condensed phase at 26°K in the backflow

38

region (similar to CO). The CO_2 became more evident when the GHe and LN_2 panels were warmed to 179 and 142°K, respectively (Fig. 29c). Also in Fig. 29c, NO, H_2O, N_2O, HcN, ethylene (C_2H_4), and acetylene (C_2H_2) became identifiable.

After the temperature of the GHe and LN_2 panels reached 189 and 155°K, respectively, the NO_2 and $C^{13}O_2$ bands became evident. Further warmup to 210 and 180°K, respectively, revealed the N_2O_4 bands, as shown in Fig. 29f. Additional warmup to 260 and 250°K by pressurizing the chamber to 500 mm with dry nitrogen yielded no additional observable species, although H_2O, CO_2, N_2O, NO, CO, and CH_4 bands became much more pronounced.

It is interesting to note that in the gas phase CO, CO_2, $C^{13}O_2$, N_2O, NO, NO_2, and N_2O_4 were all identified; these same species were also found in the backflow region (26°K). However, methane (CH_4), HCN, acetylene (C_2H_2), and ethylene (C_2H_4), were also observed in the gas phase, yet none of these species was found in the backflow IR spectra at 26°K. The fact that these constituents are seen in the chamber warmup but not in the 26°K backflow IR spectra means that these species probably exist in the plume core and thus can exist only in the forward flow region. These species probably do not exist in the nozzle boundary layer and thus do not undergo expansion into the backflow region. However, the more volatile N_2O_4 vapor can diffuse into the nozzle boundary layer, where less efficient combustion occurs. The effect of this incomplete combustion is the formation of species such as NO, N_2O, N_2O_3, and NO_2 along with unreacted N_2O_4. These species' being in the boundary layer allows for their expansion into the backflow region. Another explanation for some species' (CH_4, HCN, C_2H_4) not existing in the backflow region is that they are not formed in the exhaust plume but are actually formed on the cryopanels during the chamber warmup.

The two relatively strong bands covering the wavenumber ranges from 775 to 875 cm^{-1} and 960 to 1,060 cm^{-1} in Figs. 29f through i have not yet been identified. These bands were first seen at GHe and LN_2 panel temperatures of 210 and 184°K, respectively, for a chamber pressure of 41 torr. The bands resemble MMH($CH_3N_2H_3$) in appearance but are shifted considerably in wavenumber, and a strong MMH band at 2,800 to 2,900 is not observed in the biprop data of Fig. 29. Therefore, MMH was eliminated as the possible source of these bands. Several species similar to MMH in chemical formula were considered such as trimethylhydrazine, trimethylamine, tetramethyl hydrazine, monomethylamine, monoethylamine, methyl azide, asomethane, and others, but none was seen to match MMH. It appears that these two bands are caused by some modified form of the MMH molecule.

4.5 TWO-ANGLE LASER INTERFERENCE RESULTS

The two-angle laser interference technique was used for all engine configurations tested. However, the number of uninterrupted pulses where useful refractive index at 0.6328 μm

and density data could be obtained were available primarily for configurations A and D. For configuration D a refractive index of 1.35 (at 0.6328 μm) was measured; however, a density determination was not obtained. For the baseline engine (configuration BL) the refractive index was found to be 1.34, and this was the value of refractive index used in determining the deposit thicknesses for the n and k data.

Coupling the deposit thickness from the two-angle laser interference technique with the surface mass obtained from QCM No. 4 enabled computation of the deposit density. As Table 7 shows, the average refractive index for 26°K at 0.6328 μm was 1.34; the average density was 0.765 gm/cm^3. Since data were obtained from four different engine configurations (A, BL, C, and D) at 26°K with very little variation in either n or ϱ, it appears that the exhaust products in the plume were the same regardless of engine configuration, O/F ratio, or P$_c$ value. This confirms the findings of the QCM data and IR transmission data.

The density data of Table 7 show that for deposits formed at 100°K and 140°K the density and refractive index were essentially constant; at these same temperatures the IR transmission data show the deposits to be almost totally H$_2$O with a small amount of some nitrate. The density of 0.85 gm/cm^3 and n = 1.346 of Table 7 compare favorably with those found for pure H$_2$O at 80°K, which are ϱ = 0.923 gm/cm^3 and n = 1.316. Thus from the IR data and Table 7, the deposit at 100°K appears to contain only H$_2$O and a small amount of some nitrate.

At 75°K Table 7 shows a significant increase in both n and ϱ (1.417 and 1.01 gm/cm^3, respectively). This is evidence that between 75 and 100°K one or more additional species which have high values of n and ϱ begin to cryopump thus causing the overall bulk properties to increase. The new species seen at 75°K which has these properties is N$_2$O$_4$ with a refractive index and density of n = 1.56 and ϱ = 1.84 gm/cm^3. The IR transmission data show also that at 75°K significant amounts of N$_2$O$_4$ were observed for the first time in the IR spectra.

When the exhaust products were deposited at 26°K (Table 7), the density and refractive index were both observed to decrease. This was caused by the cryopumping of large amounts of N$_2$ which would tend to dilute both the density and refractive index since pure N$_2$ has a value of n = 1.24. Since N$_2$ is not IR active, it cannot be detected from the IR transmission data; however, the density data imply N$_2$ to be a major exhaust constituent, as was expected.

With n and ϱ known, the Lorentz-Lorenz constant [(n^2 − 1/n^2 + 2)/ϱ] was computed and is shown in Table 7. The other columns of Table 7 show the thickness and mass per

engine pulse and per second of engine firing time. Overall, for a given temperature (26°K) the physical properties (ϱ and n) of the deposit were essentially constant regardless of the engine used. This supports the QCM and IR transmission data, which show the engine cryopumped species to be the same regardless of the engine configuration of operating conditions.

4.6 THERMOVISION (INFRARED SCANNING CAMERA) RESULTS

The results obtained with the AGA thermovision are in the form of flow visualization. Infrared flow visualization identifies regions of peak radiance and is useful for providing an IR plume map. On each thermogram (Fig. 30, typical) the dark blue color on the left of the intensity scale corresponds to the lowest intensity, and the white on the right of the intensity scale corresponds to the highest intensity. The intensity scale on each thermogram is divided into ten color bands for a given range setting as follows:

Range, percent	Verbal Description
0	Left Side of Dark Blue Region
10	Dark Blue/Light Blue Boundary
20	Light Blue/Green Boundary
30	Green/Turquoise Boundary
40	Turquoise/Light Pink Boundary
50	Light Pink/Dark Pink Boundary
60	Dark Pink/Red Boundary
70	Red/Orange Boundary
80	Orange/Yellow Boundary
90	Yellow/White Boundary
100	Right Side of White Region

For the data recorder with the IR scanning camera an 8-deg field-of-view lens was used. This corresponds to an instantaneous spatial resolution element of about 0.8 cm square (r milliradians). The engine spatial field covered corresponds to about 1 in. upstream of the nozzle exit plane to about 12 in. downstream of the nozzle exit plane. The thermogram shown in Fig. 30 corresponds to engine configuration A after 0.5 sec of firing. From Fig. 30 the radiance is seen to monotonically decrease along the nozzle axis centerline with no evidence of any type of shock waves. Any gases which reached the backflow region were not emitting enough energy to be detected with the IR scanning camera. As expected, all of the radiant energy associated with the plume was concentrated in the forward flow regions.

41

4.7 SOLAR CELL RESULTS

Since most of the solar cell usage in space is for power, during the program the solar cells were operated at resistance load conditions corresponding to the peak of the power curve. The peak of the power curve was found to correspond to a resistance of 30 ohms for silicon and 70 ohms for selenium. With the load resistance in the circuit, the voltage generated is a linear function of the light intensity incident on the cell. Selenium responds to radiation in the 0.35- to 0.70-μm range, peaking at about 0.60 μm. Silicon is more sensitive to the near infrared in the range from 0.40 up to 1.15 μm with a peak at approximately 0.90 μm.

Solar cell scans were normally made prior to the start of a test sequence on a motor configuration and following completion of each day's firings. Table 8 is a record of the solar scans made during the program. The total engine operating time between scans is recorded in the table. After each series of firings both the solar readings and the percent change are given for the loaded condition. Solar cells 1 through 5 are the silicon cells inside the chamber and 6 through 10 are the selenium cells, also inside. Numbers 11 and 12 are the two external selenium solar cells. The solar cells (Fig. 7) were positioned 45 deg from the plume centerline and 33 in. downstream from the nozzle exit plane.

The output voltages for the silicon cells (Nos. 1 through 5) are very constant for the baseline readings as can be seen from the data for configuration A (Table 8) prior to the first series of firings. The selenium cell outputs showed considerable variation for the loaded condition (e.g., 0.080 to 0.238 volts). After the first day's firings (35.75 sec of firing time for nozzle configuration A) the measurements showed a slight drop in output voltage for the silicon cells but not for the selenium. Solar cell outputs from Nos. 11 and 12 outside the cell were about 5 percent higher for the first series of measurements and continued to read about 5 percent high even after the final day's firing, giving a total accumulated firing time of 241.5 sec. For the silicon cells after 241.5 sec of firing there was some variation between individual cells, the variation being between no change and a decrease of 11.4 percent. For the selenium cells essentially no change was detected after completion of the first series of firings. Changes of less than ±3 percent were considered essentially no change since there could have been this much variation in the beam intensity. In general, through the first major series of tests only slight degradation was observed, and that was for the silicon cells.

After completion of the first series of tests the entire chamber was brought to atmosphere and the inside of the cell cleaned. A fine dust was found on most of the interior surfaces. The solar cell surfaces were cleaned prior to the second part of the test (nozzle configuration BL). Solar cell No. 4 failed when a new set of baseline readings was taken. It is not known whether this failure was due to the surface cleaning, but visual inspection showed

no surface difference between the various cells. The final measurements after completion of this series, for 364 sec of accumulated firing time, revealed only 2 to 3 percent reduction for the silicon cells and essentially no change for the selenium. These results agree closely with the observed results from the first series of firings. The two external cells showed considerable variation throughout the firing sequence. The cause of the variation in the two external cells is unknown. However, it may have been due to a combination of 1) the blockage of the tube protecting them from directly seeing the plume, and 2) the orientation of the solar simulator.

The third series of firings (nozzle configuration B) showed essentially the same results as the first two with little if any degradation after 379 sec of firing time; the outputs for the most part were within ±3 percent of the baseline readings.

The final series of firings (nozzle configuration D) consisted of 450 sec of firing time. It was observed that the baseline reference measurements were approximately 40 percent lower than that observed in prior baseline readings. The cells were not cleaned between the last two series of firings since the chamber was not pressurized to atmosphere during that time. The cause of the 40-percent or so reduction in the output level is unknown. After 187 sec of firing time the data showed an average increase for the silicon cells of about 5 percent, whereas the selenium cells showed essentially no change over the baseline readings. The last day of firings brought the accumulated firing time to 450 sec for the fourth series. The data were obtained while the chamber pressure had increased up to a few millimeters; the results were very erratic and may have been heavily influenced by chamber pressure.

The data obtained for the first three series of experiments were consistent and indicated little solar cell degradation. The silicon cells appeared to be affected more than did the selenium. Even for the silicon, however, only 5- to 10-percent degradation was observed. The final series of measurements was inconclusive because the behavior was erratic.

4.8 ATTENUATED TOTAL REFLECTANCE MEASUREMENTS

Measurements were made of the two ATR plates mounted to the temperature-controlled retractable sting. A problem encountered with this unit in early tests was the slight contamination of the ATR plate (facing the engine) by mechanical vacuum pump during the process of removing the plate from the chamber. This problem was overcome for later test sequences. Figure 31 is typical of a scan made with the dual beam spectrometer before insertion into the chamber. After exposure to a full day's firing (88 sec) the results shown in Fig. 32 were obtained. Very little change is evident, and while the measurement is sensitive enough to identify very small amounts of vacuum pump oil, no exhaust constituents could be identified for this ATR plate. No evidence of exhaust residues was measured in any of the other test sequences.

4.9 WITNESS PLATES

None of the reactive witness plates inserted into the backflow region produced droplet stains which could be associated with droplets of fuel or oxidizer being ejected from normal motor operation. Early evidence of contamination on the witness plates which were withdrawn from the chamber with the ATR plates was traced to vacuum pump oil (Section 4.8), and this was corrected by cleaning the system. There was no evidence of droplets on the witness plates installed with the ATR plate under the motor and slightly behind the exit plane (Fig. 3).

Witness plates installed in the forward flow region were all badly eroded and were covered with particles and liquid droplets when they were recovered from the test chamber. Subsequent examination of these witness plates and selected surfaces in the test chamber does not preclude droplets being in the exhaust plume but indicates that the deposits probably accumulated from the gas phase and that the droplets and particles were formed during the test chamber warmup and repressurization.

In the forward flow region of the test chamber every attempt was made to cool all components to cryogenic temperatures in order to maximize the cryopumping of the exhaust gases. The witness plates attached to these surfaces were also operating at cryogenic temperatures. During a test series it was observed that a visible cryodeposit accumulated on the witness plates similar to that noted on the cryopumps. After a test series the chamber was slowly warmed up and the bulk of the cryodeposit sublimed. However, some residues remained even after the system reached room temperature. These residues can be classified into three basic types.

(1) Clear Liquid Droplets: These droplets ranged in size from 10 to 300 μm in diameter and were observed on aluminum-coated witness plates which had been mounted on 20°K cryosurfaces. The droplets appeared quite stable at atmospheric conditions. Several samples were placed in a dessicator for four days. There was no indication of evaporation; however, it was noted that after several weeks' storage the droplets had eaten through the aluminum coating and the droplet had solidified with a slightly milky coloration. One witness plate was slowly heated, and it was noted that the droplets first started to evaporate and then turned brown. As the heat was increased the droplets turned a darker brown and started to boil. The boiling continued until the brown liquid became very viscous and finally solidified.

(2) Dark Brown Droplets: These droplets were generally much larger, ranging from 300 to 5,000 μm. This liquid was quite viscous and resembled the later stage of the clear droplets as they were heated. These droplets were observed not only on witness plates but also on

some of the LN$_2$-cooled cryopanels. Figure 33 shows a typical distribution on a vertical panel which suggests that the liquid may have been less viscous when it first formed and ran down the panel. The material was very soluble in water and was quite easily cleaned from the cryopanels. After the second test entry a small sable hair brush and 2 cc's of distilled water were used to collect as many of these droplets as possible. The resulting liquid was vacuum distilled and produced light brown, needle-like crystals.

(3) Small Crystals: Small crystals ranging in size from 5 to 5,000 μ m were found on some of the witness plates and some of the cryopump surfaces. These plates and surfaces were generally those which had been located in the forward flow, were operated at 20°K during the test, and most probably warmed up the fastest during repressurization of the chamber. The crystals on the copper-coated witness plates were yellow in color, and most of the copper had dissolved. The crystals found on the aluminum witness plates and the stainless steel cryopumps were amber colored with darker bown inclusions. One of the vertical steel cryosurfaces had several crystal deposits located in a run pattern very similar to that of the dark brown droplets shown in Fig. 33. It was observed that on occasion during the warmup cycle the test chamber pressure could exceed the critical pressure, causing the solid nitrogen cryodeposit to liquefy and flow off the panels. Therefore, several crystals were recovered and added to a test tube containing liquid nitrogen. The crystals were not soluble in LN$_2$ or LOX, thus indicating that they were not deposited from a cryogen flow.

The amber crystals were hygroscopic and readily soluble in water. The solution was mildly acidic, and a droplet placed on a copper-plated witness plate reacted with the copper. After this droplet evaporated, a yellow crystalline material remained which was comparable to that on the copper-coated witness plates recovered from the chamber. Attempts to obtain detailed chemical analysis of the material were not successful.

From these observations it can be concluded that the brown viscous liquid and the crystalline deposits are but different manifestations of the same material. The final observed phase is a function of the warmup cycle of the test chamber. On surfaces which warm up sufficiently to form water solutions of the material while the chamber pressure is still being modulated by operation of the roughing vacuum pumps, the water vapor is pumped off, and the crystals are left behind.

Physical Properties of Crystals

A sample of one of the crystals was placed on the hot stage of a microscope and observed as it was slowly heated. At ≈ 47°C the surface appeared to glaze, and a liquid film evaporated from the surface. The basic shape or color did not change. Boiling at the dark

brown inclusions occurred at 86°C, and the crystal melted at ≈ 118°C. At this point the melt was a uniform light brown color. The material started to boil at 150°C.

As previously noted, the crystals were very soluble in water. They were slightly soluble in alcohol and acetone. It was also noted that when a crystal was placed on an open surface and a droplet of acetone added, the complete crystal dissolved. When the acetone evaporated, a yellowish liquid droplet remained. Since this residual liquid did not appear for samples treated with acetone in a small test tube, it is suspected that the enhanced solubility and the residual droplet are caused by adsorption of moisture from the ambient air.

The quantity of material recovered from the chamber was very small (≈ 0.1 gm). However, considering the large surface area of the cryopumps this sample represents a significant quantity of material deposited during the test series. At this point it is impossible to state whether the crystalline material is a result of particle combustion in the engine or partial reaction of raw fuel and oxidizer collected on the cryopanels. It would appear that the crystal clusters are a mixture of at least two MMH-nitrates, one with a very low melting point (≈ 47°C) and the other at ≈ 118°C.

4.10 PHOTOGRAPHY

The prime purpose of the sequence camera was to observe the lip and inner wall of the rocket motor nozzle and to record any evidence of liquid films or droplets which might form. The system did not have sufficient resolution to record micron-sized droplets which might be contained in the exhaust plume. One thousand photographs were examined, and no evidence of wall films or droplets was found.

While the sequence camera focus was adjusted it was noted that several sections of the cryopanels fluoresced each time the engine pulsed. Since there were no thermocouples located on these panels, no exact temperatures are noted. However, the surfaces were identified as being on the inlet side of the gaseous helium refrigerators, which were operating at 16°K. The surfaces were coated with a visible white cryodeposit with streaks of dark brown, and those areas fluorescing were in direct line with the exhaust plume. A transfer line from the LHe pump also started to fluoresce toward the end of the day's test period. This line was directly exposed to plume gases and was protected by several layers of aluminized mylar and aluminum tape. No temperatures are available for this surface; however, since it was alternately carrying LHe and vent gases from the liquid helium pumps, it is quite reasonable to suggest that its outer layers may have dropped below 20°K toward the end of the test run. The cryofrost fluorescence is apparently sensitive to cryopanel surface temperatures. It was observed for all engine configurations and operating parameters.

4.11 MASS SPECTROSCOPY

The mass spectrometer was set to sweep over a mass range from 2 to 60 amu. This produced approximately six spectral sweeps during a 1-sec engine firing. A typical data set is presented in Fig. 34. The spectral scan prior to engine firing indicates that H_2 is the major species contributing to the chamber base pressure of 1.6×10^{-6} torr. It is noted that the H_2 peak is truncated since the M.S. sensitivity was set to observe the minor species. The background gases N_2, O_2, and H_2O are typical residual gases and in this configuration probably represent outgassing from the long tubulation and M.S. valving system. The small He peak should be noted since it represents a very small leak in the cryogenic system. No CO_2 peak is evident, and the peaks at amu 15, 16, 17, 27, and 29 are from the expected cracking patterns of the basic gas molecules identified (i.e., radicals, atoms and isotopes). This particular mass spectrometer installation operated with higher than normal ionization energy (10 eV versus 80 eV). This increases the sensitivity but causes larger yields of the cracked species. The ratio of the N (amu 14) to the parent N_2 (amu 28) peak in the background scan is thus higher than one would normally expect.

The first point of interest in the M.S. scans during the engine firing (Fig. 34) is the appearance of a strong peak at 30 amu. This is indicative of NO. The lack of a peak at 46 amu would suggest that this NO is a partial reaction product from the engine rather than part of the cracking pattern from raw NO_2 oxidizer. The high ionization energy, however, could also account for the loss of the parent 46 peak; thus these data do not preclude the presence of raw oxidizer.

Some inferences as to the source of this NO can be made by comparisons with other mass peaks. The expected combustion products for an O/F ratio of 1.6 are presented in Table 9. It is noted that in these calculations less than 1 percent NO is predicted as compared to over 43 percent N_2 and CO. Since the cryopumping efficiency of the chamber is approximately equal for all three species, then the moderate increase in the peak at amu 28 as compared to the large amu 30 signal indicates that the NO is being dumped into the backflow region in much greater abundance than the N_2 or CO. This suggests that its origin is in the boundary layer at the nozzle wall and not in the core flow of the plume.

It is impossible to determine what percentage of the amu 28 signal is due to N_2 and what percentage due to CO. It is evident, however, that both gases are present since the peak at amu 14 (N) increases and peaks at amu 12 (C) and amu 16 (O) also increase.

The relatively small increase in amu 18 (H_2O), even though this is a major species, can be readily accepted due to the extremely effective pumping of water vapor by the cryogenic

systems. A point of interest is the disproportionate rise in the peak at amu 17. This peak is usually associated with the OH ion, which is a part of the expected H_2O cracking pattern. It is possible that the additional signal at amu 17 can represent a significant ammonia (NH_3) concentration. This species is not predicted from the combustion code and thus would represent a partial combustion product from the fuel.

The increased signal at amu 27 is also much larger than can be explained by the standard isotope of N_2. There are few species which produce a 27 peak, and the most promising candidate is suggested as HCN. Once again, this species is not predicted by the combustion code and thus may be a partial combustion product found mainly in a cool boundary layer from the engine.

Two further comments can be made regarding these spectra, and they concern the lack of peaks. No evidence of a signal is observed at amu 46. This is the prime peak for the raw fuel as well as the oxidizer. This could indicate at least partial reaction of all fuel and oxidizer, although the location of the mass spectrometer and the long tubulation could mask small quantities of both components. The helium peak evident in the prefire scan is seen to decrease significantly during the firing. A He leak had been suspected to be in the fittings to the liquid helium pump in the far end of the chamber and thus represented a net helium flow into the background from downstream of the engine. The fact that this gas source was shut off when the engine fired is evidence that gases sampled in the backflow region are not gases which have rebounded from the far end of the test cell. That is, any gases which are not cryopumped by the extremely efficient cryosystem are effectively blocked from the backflow region by the ejector action of the rocket plume itself.

CONCLUDING REMARKS

The distribution of rocket exhaust constituents in the back flow region of a small bipropellant rocket have been successfully measured. The use of a specially configured test chamber that could maintain low pressure (1 x 10^{-5} torr) during engine firing and a variety of specially applied diagnostic techniques produced measured results which can be used for spacecraft system design and for detailed comparison to future computer models of high altitude plume expansions.

REFERENCES

1. Hoffman, R. J. et al. "Plume Contamination Effects Prediction — The CONTAM Computer Program, Version II." AFRPL-TR-73-46, August 1973.

2. Williams, W. D. et al. "Experimental Study of Monopropellant Hydrazine Thruster Exhaust." Proceedings of the JANNAF 10th Plume Technology Meeting, San Diego, California, September 1977, Vol. II, pp. 209-225.

3. Williams, W. D. et al. "Experimental Study of the Plume Characteristics of an Aged Monopropellant Hydrazine Thruster." AEDC-TR-79-2 (ADA068326), April 1979.

4. Schoenman, L. and Schindler, R. C. "Five-Pound Bipropellant Engine." AFRPL-TR-74-51, 1974.

5. *Test Facilities Handbook* (Tenth Edition). von Kármán Gas Dynamics Facility, Vol. 3. Arnold Engineering Development Center, May 1974.

6. Dawbarn, R. et al. "Development of an Integrated Cryogenic Pumping System for Rocket Plume Studies." AEDC-TR-71-19 (AD880649), February 1971.

7. Schoenman, L. and Lundgreen, R. B. "AJ 10-181 5-lbf Bipropellant Engine: User's Manual." Aerojet Liquid Rocket Company, December 1976.

8. Baerwald, R. K. and Passamaneck, R. S. "Monopropellant Thruster Exhaust Plume Contamination Measurements." AFRPL-TR-77-44, September 1977.

9. Chirivella, J. E. "Hydrazine Engine Plume Contamination Mapping, AFRPL-TR-75-16, 1975.

10. Pipes, J. G. et al. "Transmission of Infrared Materials and Condensed Gases at Cryogenic Temperatures." AEDC-TR-77-71 (ADA044517), September 1977.

11. *Internal Reflection Spectroscopy*, Vol. 1. Wilkes Scientific Corporation, 1965.

12. Hill, J. A. F. and Draper, J. S. "Analytical Approximation for the Flow from a Nozzle into a Vacuum." *Journal of Spacecraft and Rockets*, Vol. 3, No. 10, October 1966, pp. 1552-1554.

13. Simons, G. A. "Effect of Nozzle Boundary Layers on Rocket Exhaust Plumes." *AIAA Journal*, Vol. 10, No. 11, November 1972, pp. 1534-1535.

14. Boynton, F. P. "Exhaust Plumes from Nozzles with Wall Boundary Layers." *Journal of Spacecraft and Rockets,* Vol. 5, No. 10, October 1968, pp. 1143-1147.

15. Abernethy, R. B. et al. "ICRPG Handbook for Estimating the Uncertainty in Measurements made with Liquid Propellant Rocket Engine Systems." CPIA No. 180, April 30, 1969.

16. Wiener, R. N. and Nixon, E. R. "Infrared Spectrum of Dinitrogen Tetroxide." *Journal of Chemical Physics*, Vol. 26, No. 4, April 1957, pp. 906-908.

17. Bibart, C. H. and Ewing, G. E. "Vibrational Spectrum, Torsional Potential, and Bonding of Gaseous N_2O_4." *Journal of Chemical Physics*, Vol. 61, No. 4, 15 August 1974, pp. 1284-1292.

18. Herzberg, G. *Molecular Spectra and Molecular Structure, Vol. II: Infrared and Raman Spectra of Polyatomic Molecules*, van Nostrand Co., Inc, 1945.

19. Begun, G. M. and Fletcher, W. H. "Infrared and Raman Spectra of $N_2{}^{14}O_4$ and $N_2{}^{15}O_4$." *Journal of Molecular Spectroscopy*, Vol. 4, No. 5, May 1960, pp. 388-397.

20. Vasicek, A. *Optics of Thin Films.* Interscience Publishers, Inc., New York, 1960.

21. Heavens, O. S. *Optical Properties of Thin Films.* Dover Publications, Inc., New York,

22. Herzberger, M. and Salzberg, C. D. "Refractive Indices of Infrared Optical Materials and Color Correction of Infrared Lenses." *Journal of the Optical Society of America*, Vol. 52, No. 4, April 1962, pp. 420-426.

LHe Supply Dewar

LN$_2$ "V" Shield

GHe Pump

QCM

LHe Pump

LN$_2$ Liner

GHe Pump

LHe Pump

Antechamber
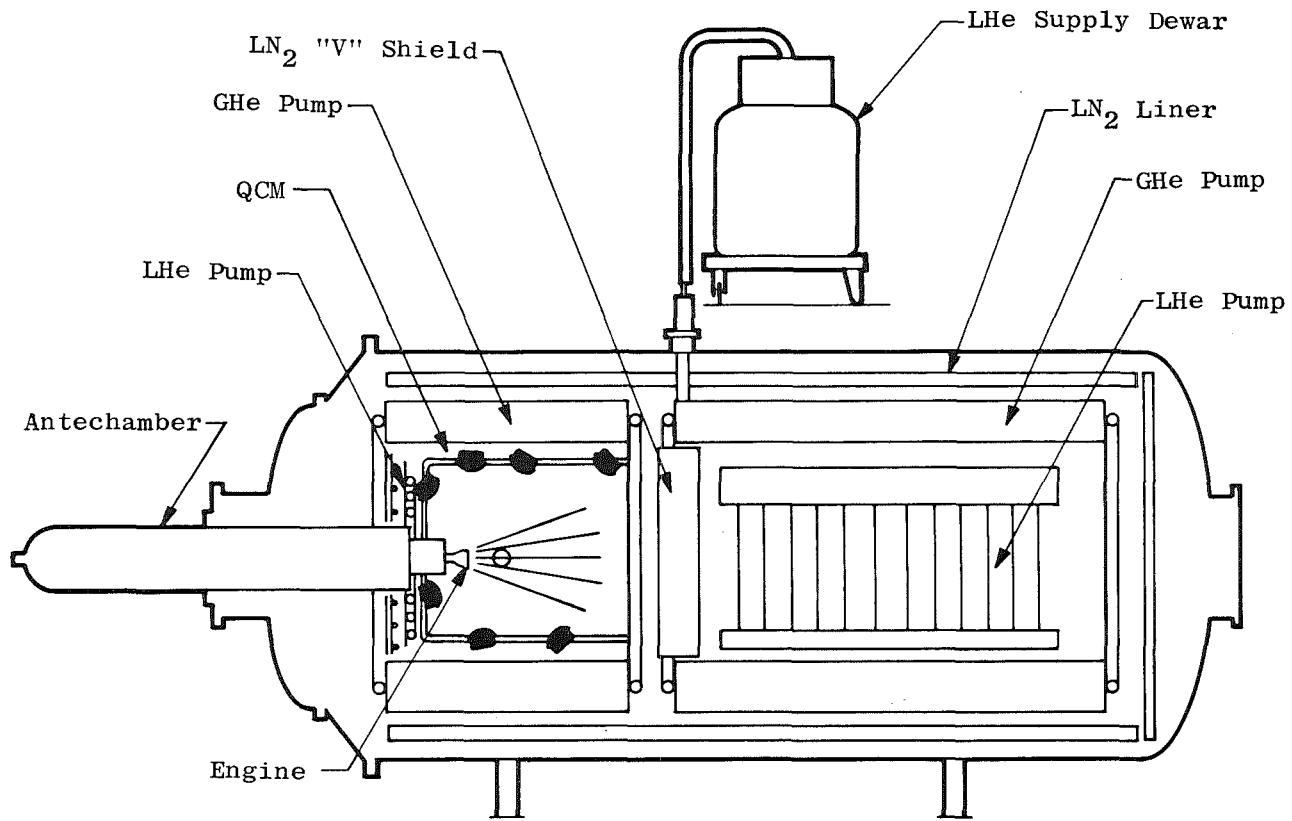
Engine

Aerospace Chamber 10V: Bipropellant Contamination test configuration, chamber elevation view.
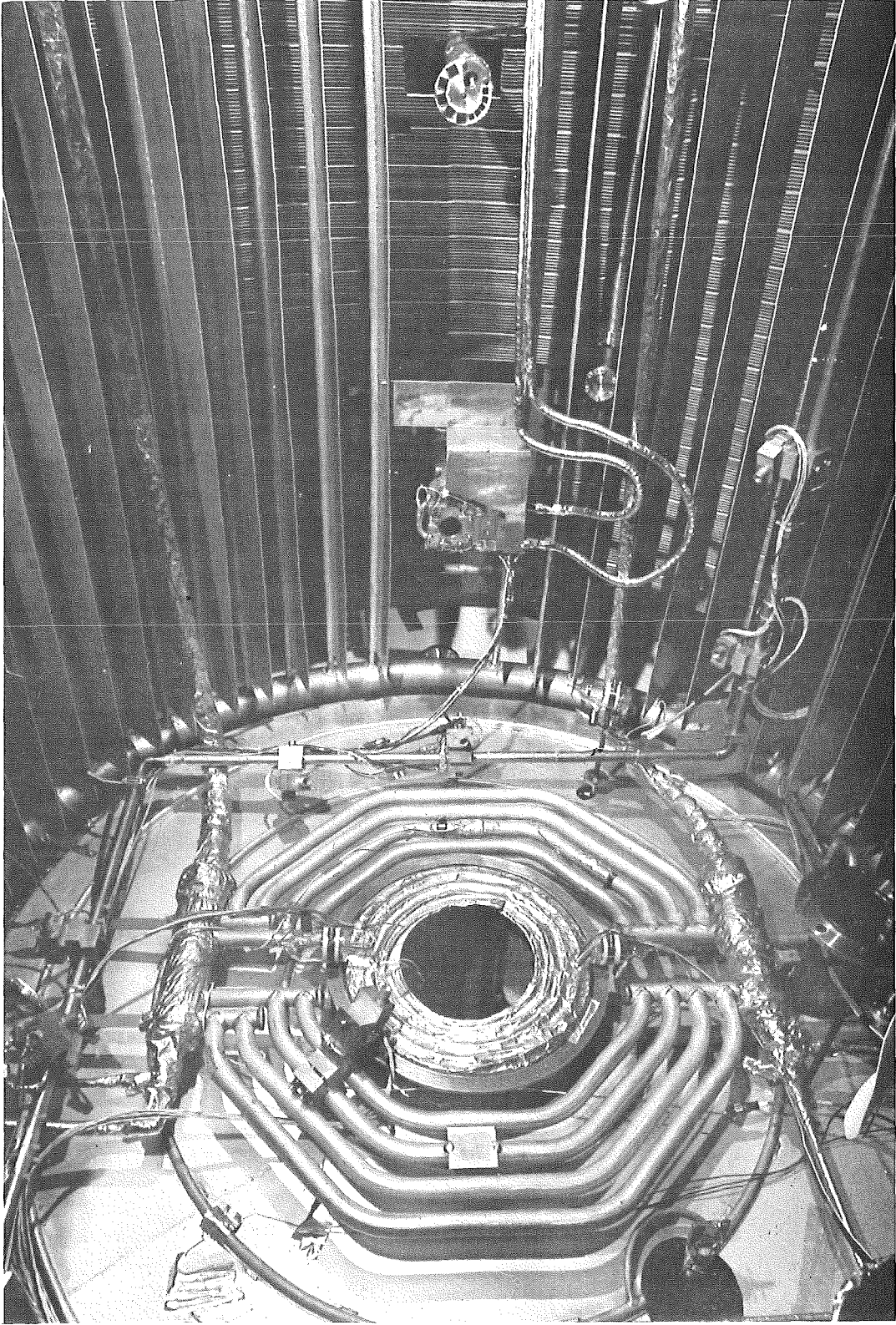
Aerospace Chamber 10V: Bipropellant Contamination test configuration, chamber interior.
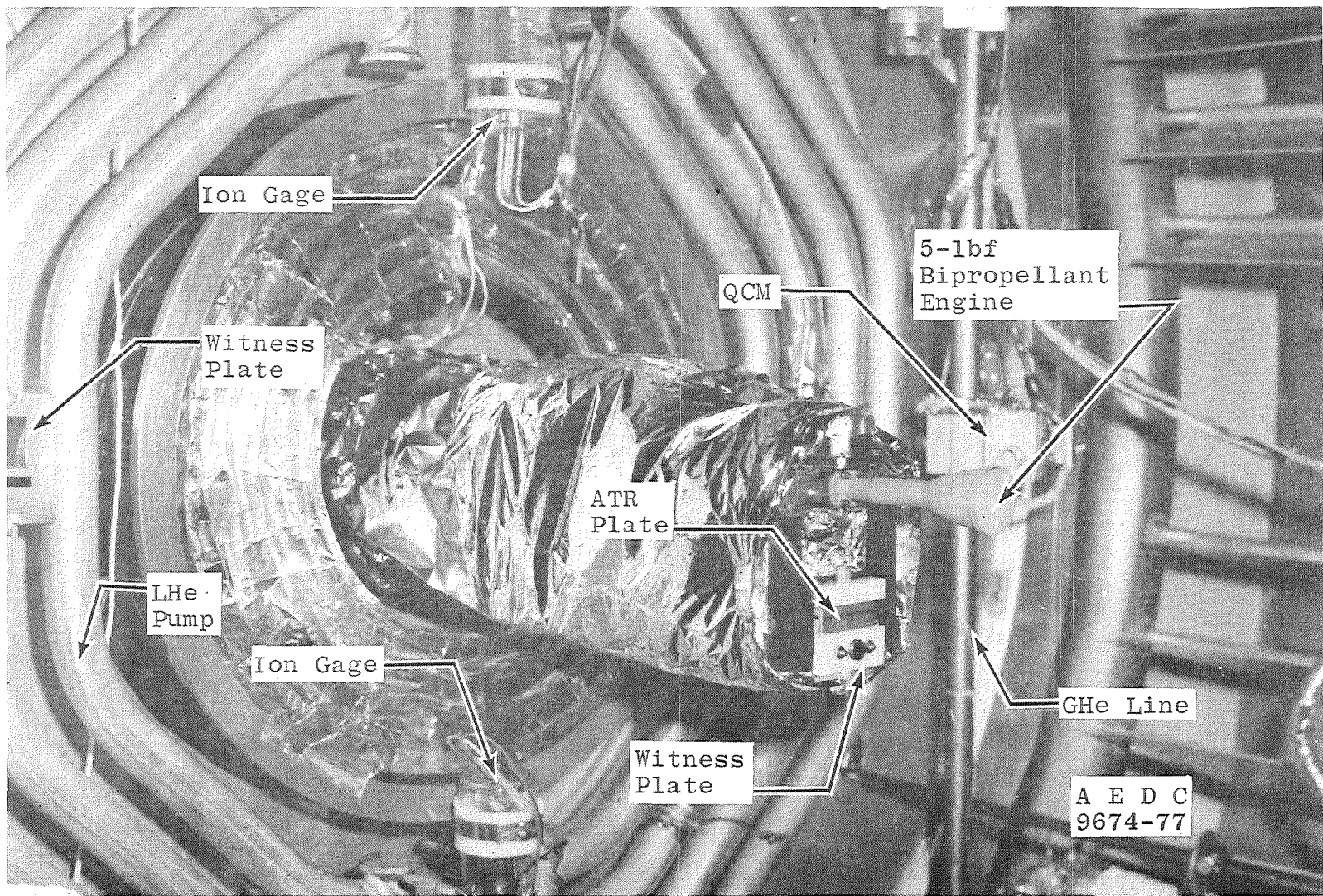
Figure 3. Five-lbf thrust bipropellant engine assembly.
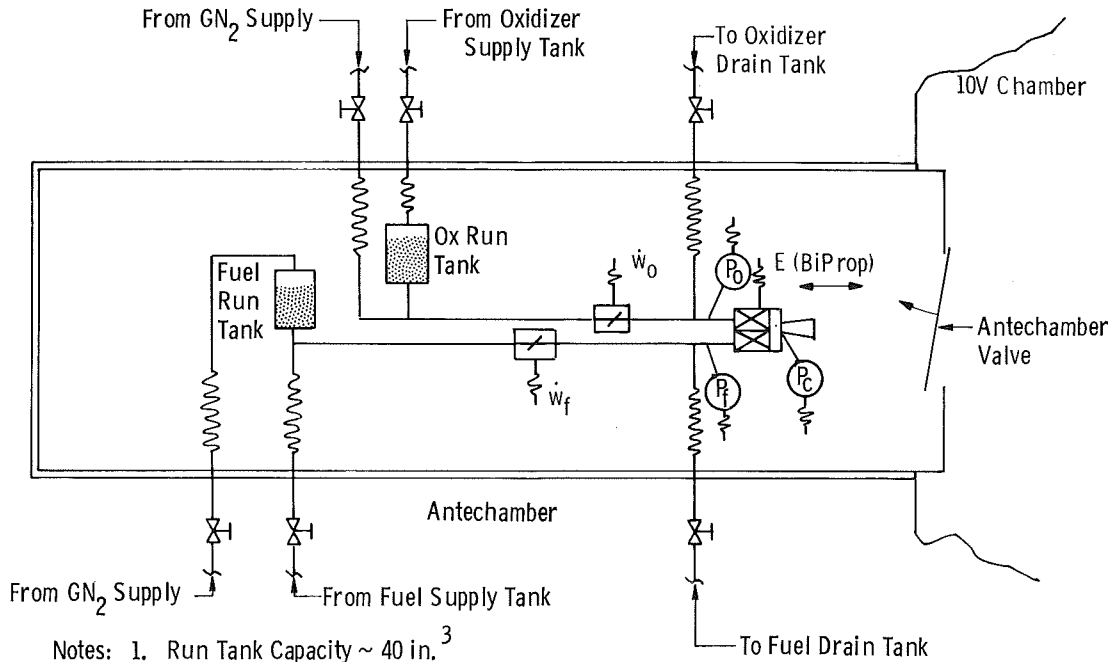
Notes: 1. Run Tank Capacity ~ 40 in.^{3}
2. Fuel Feedline Length ~ 60 in.
3. Ox Feedline Length ~ 33 in.

P_c	Combustion Chamber Pressure	Taber 2210	0 to 200 psia
P_o	Oxidizer Feedline Pressure	Taber 2210	0 to 1,000 psia
P_f	Fuel Feedline Pressure	Taber 2210	0 to 500 psia
$\dot{w}_o$	Oxidizer Flow Rate, gpm	Flow Technology	0 to 0.05 gpm
$\dot{w}_f$	Fuel Flow Rate, gpm	Flow Technology	0 to 0.05 gpm
E	Bipropellant Valve Voltage		0 to 28 v dc

Recorder: Honeywell Model 1858 CRT Visicorder

Figure 4. Propellant system Bipropellant Contamination test schematic.
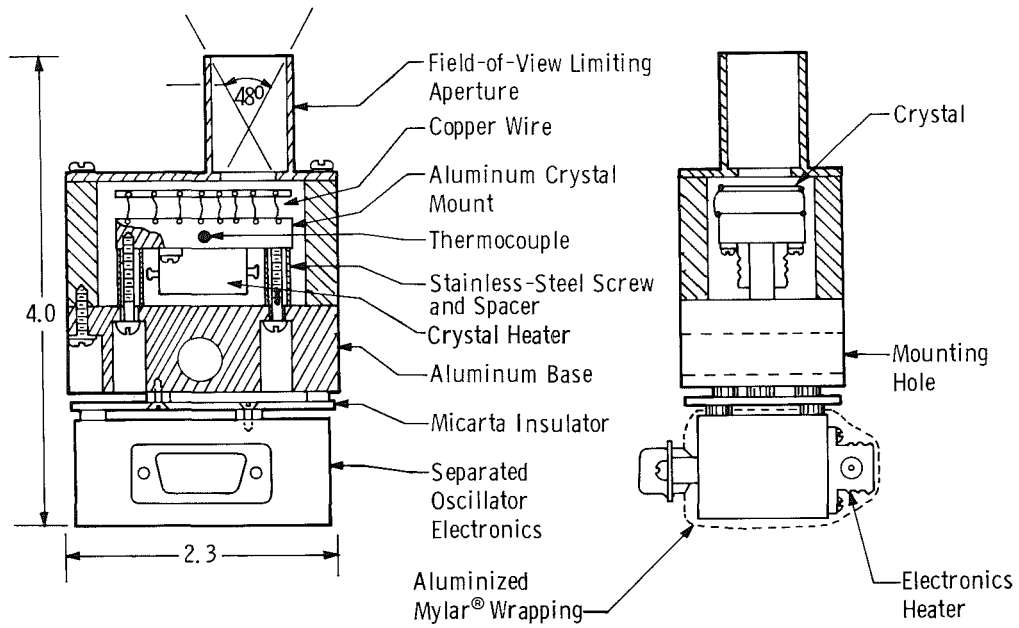
Figure 5. Quartz crystal microbalance.

1. Pyroelectric detector and collection optics.
2. Laser beam detectors.
3. Cryogenically cooled infrared window; germanium, 4 mm thick by 70 mm square (0.158 in. by 2.76 in.) and QCM #4.
4. Helium-neon laser (0.6328 μm) beams employed to measure cryofilm thickness.
5. Infrared beam, 38 mm in diameter (1.5 in.).
6. 2-mw He-Ne laser.
7. Michelson interferometer.
8. Infrared source and collimator mirror.
9. QCM #4.
10. Engine nozzle exit (5 lbf).

Top View

Top View

62.5 deg

82 cm

2.5 deg

Chamber Side View
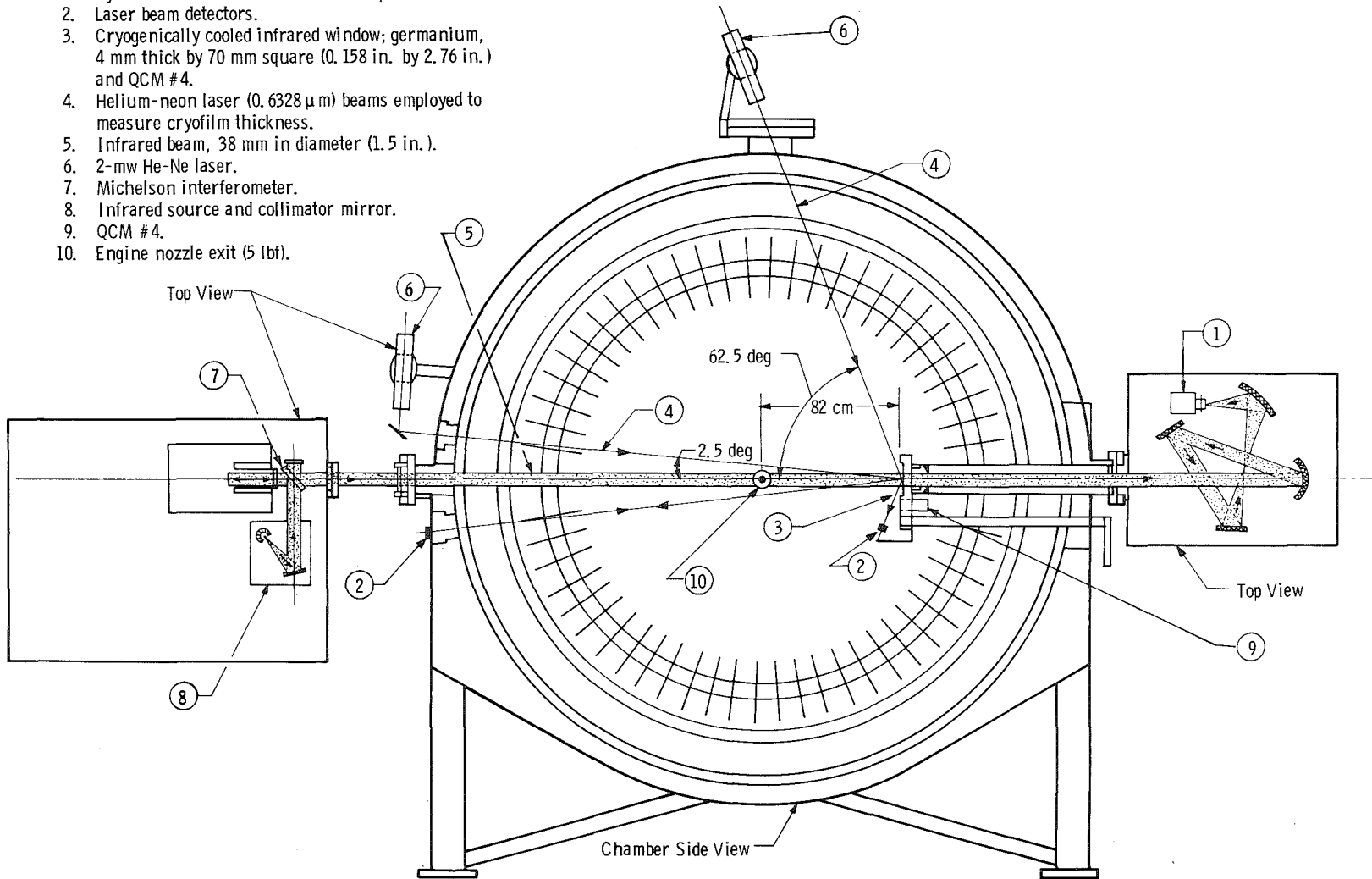
Figure 6. Schematic of 10V with FTS-14 interferometer, two-angle laser interference apparatus, IR substrate (germanium) and QCM No. 4.

0.65- by 0.75-in. Selenium Solar Cells (5)

0.2-in.-Square Silicon Solar Cells (2)

0.4-in.-Square Silicon Solar Cells (5)

AEDC
9668-77
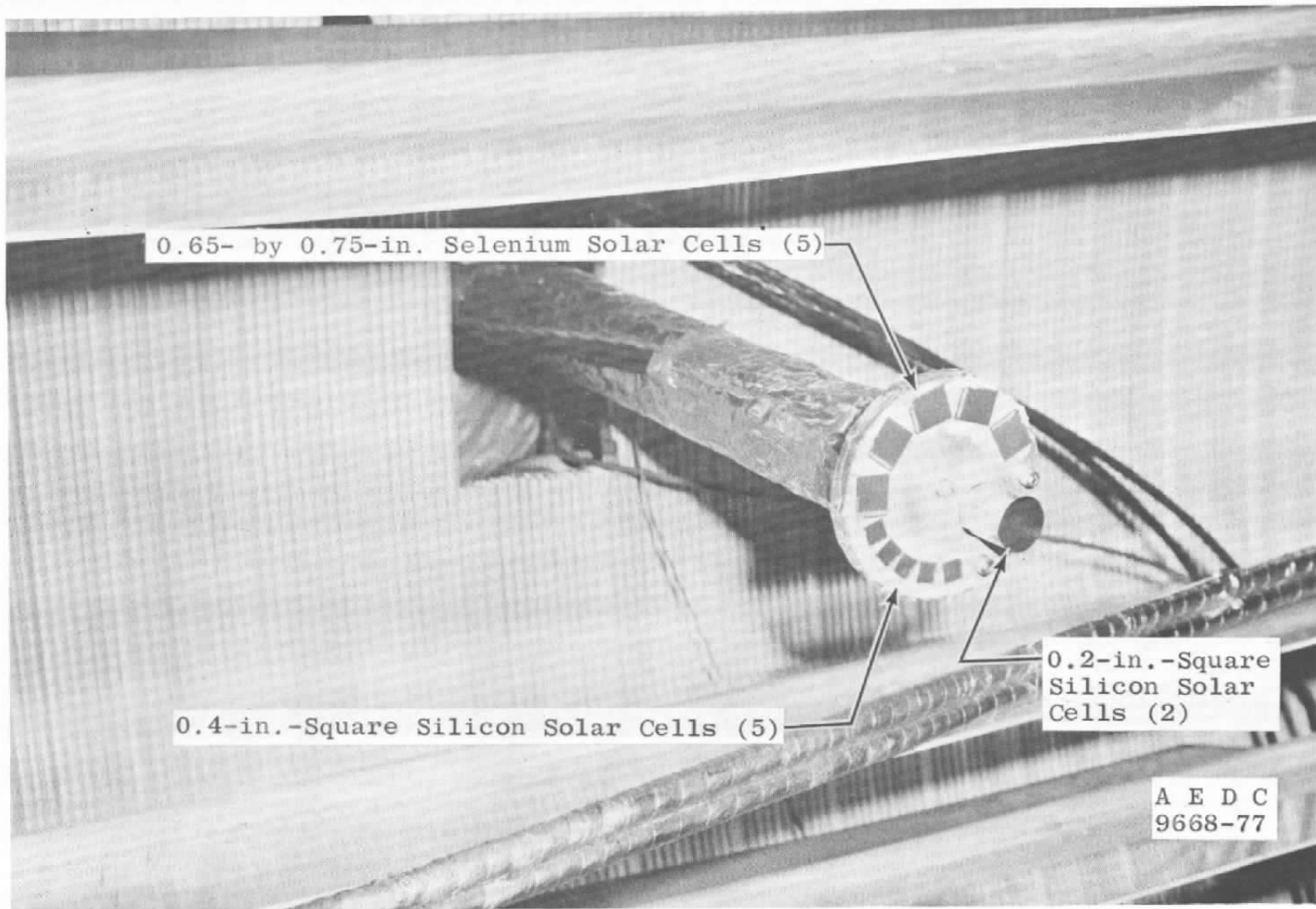
Figure 7. Solar cell apparatus in 10V.
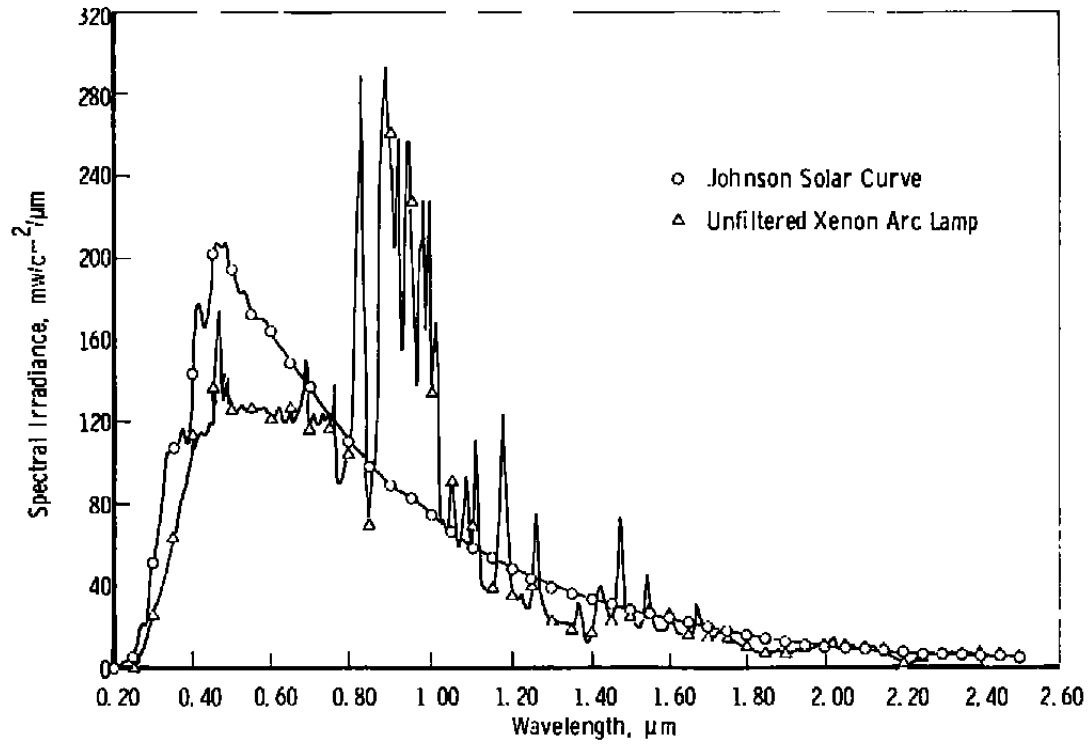
Figure 8. Spectral output of the 1,600-watt xenon lamp and the Johnson solar curve.
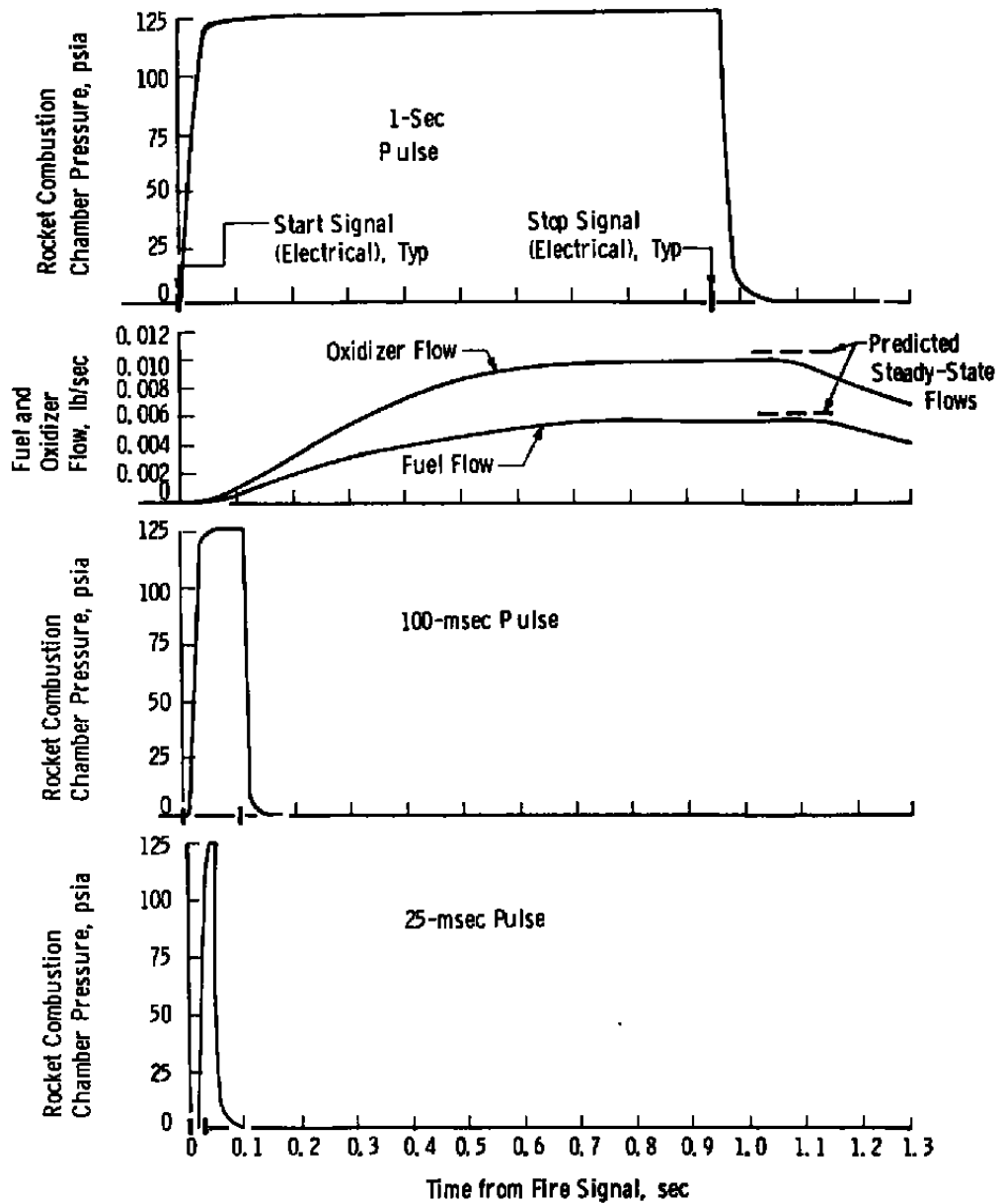
Figure 9. Engine chamber pressure and fuel flow
for different pulse lengths.
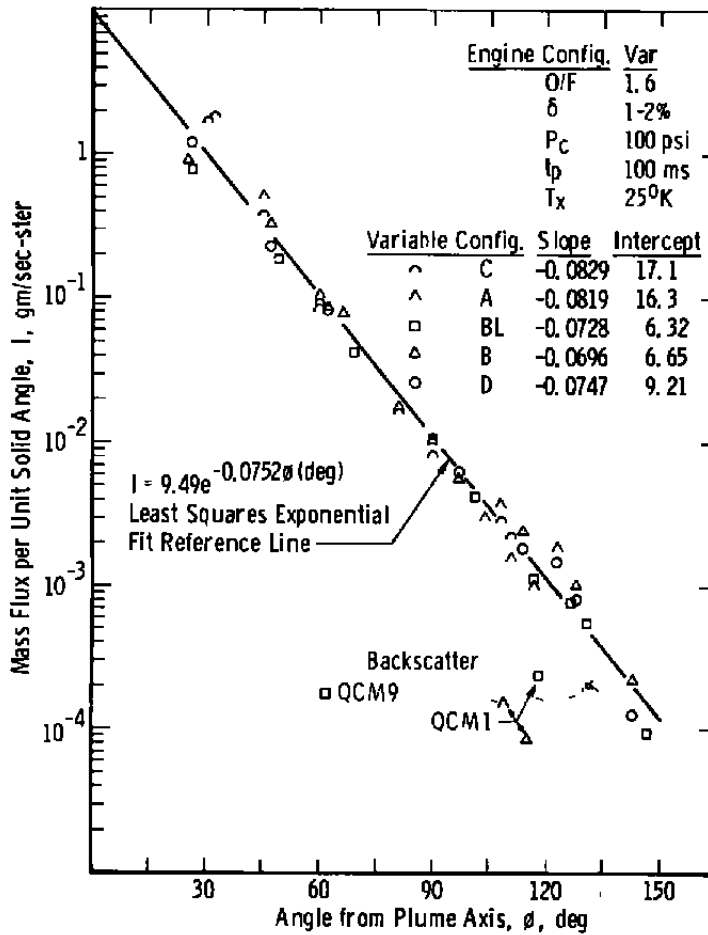
Figure 10. Mass flux for various engine configurations
at baseline operating conditions.
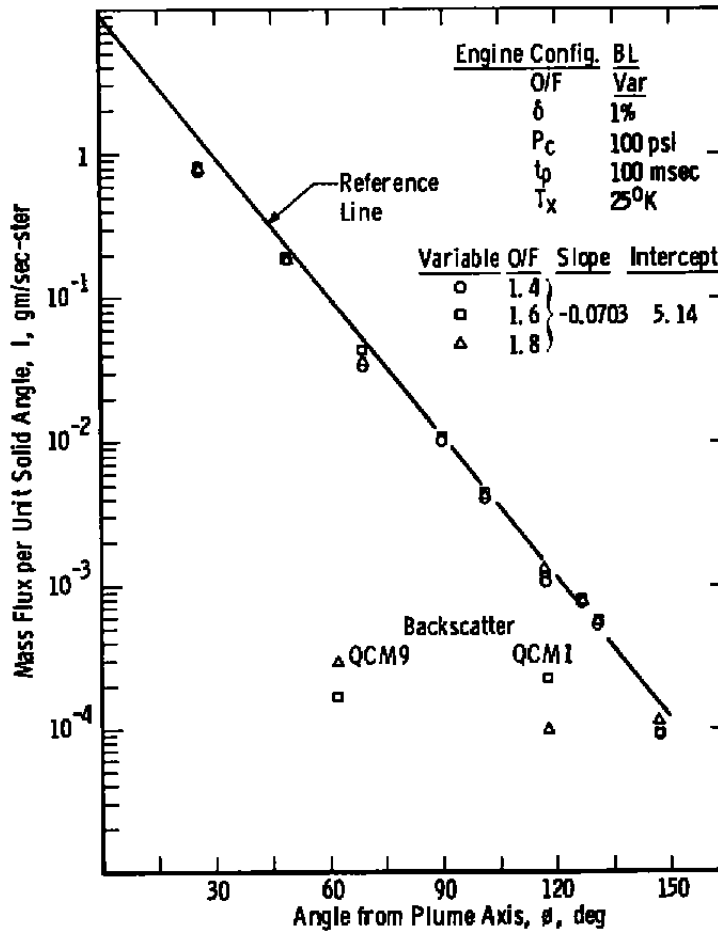
Figure 11. Effect of oxidizer-to-fuel ratio on mass flux.
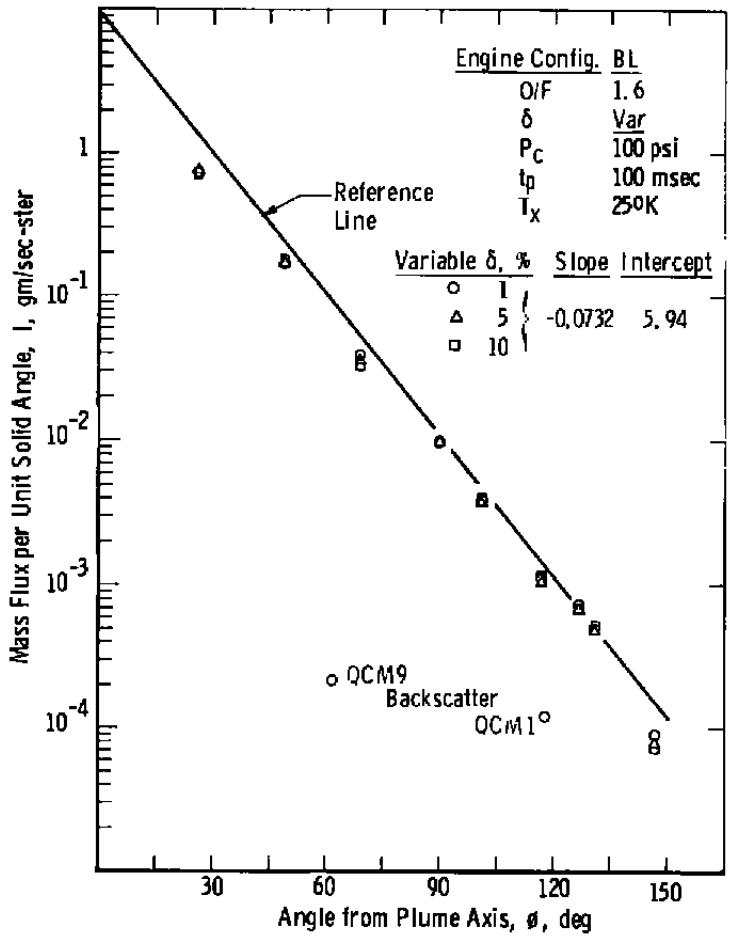
Figure 12. Effect of duty cycle on mass flux.
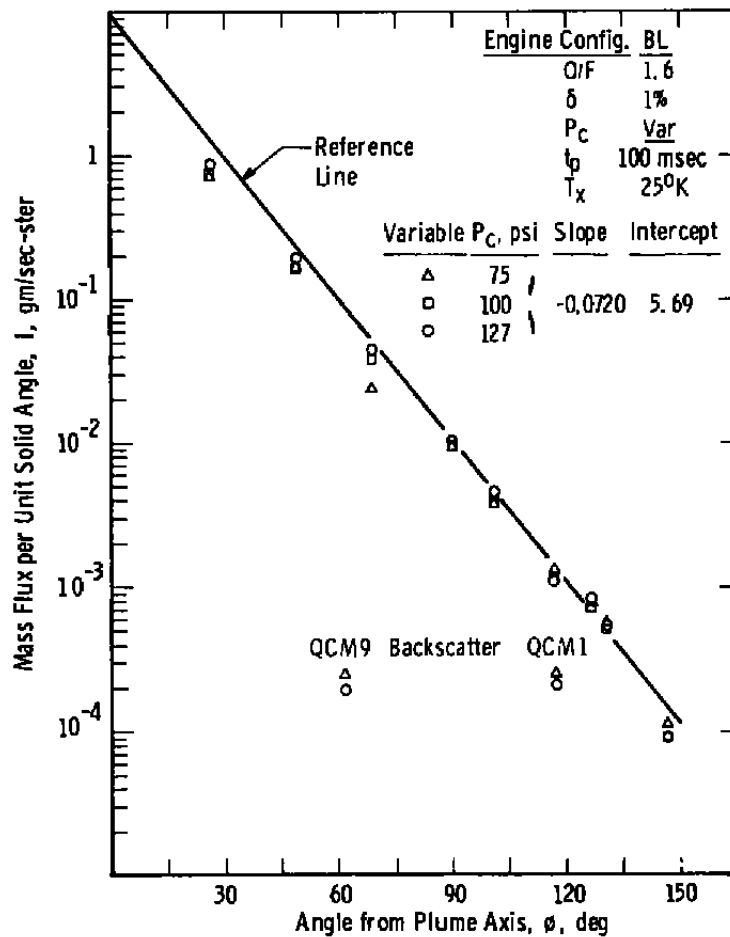
Figure 13. Effect of combustion chamber pressure on mass flux.
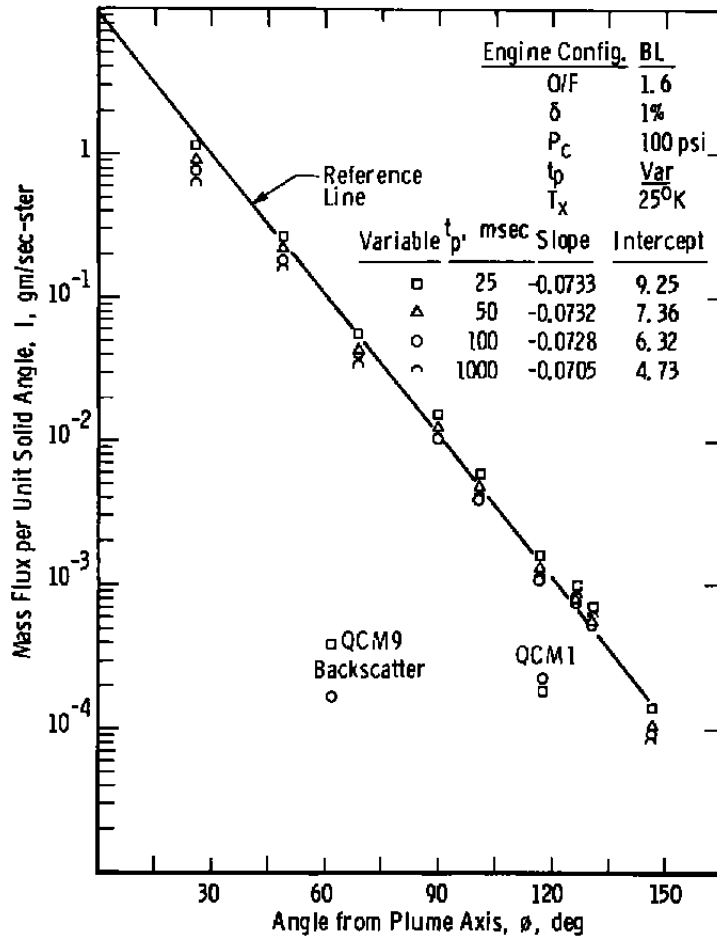
Figure 14. Effect of pulse length on mass flux.
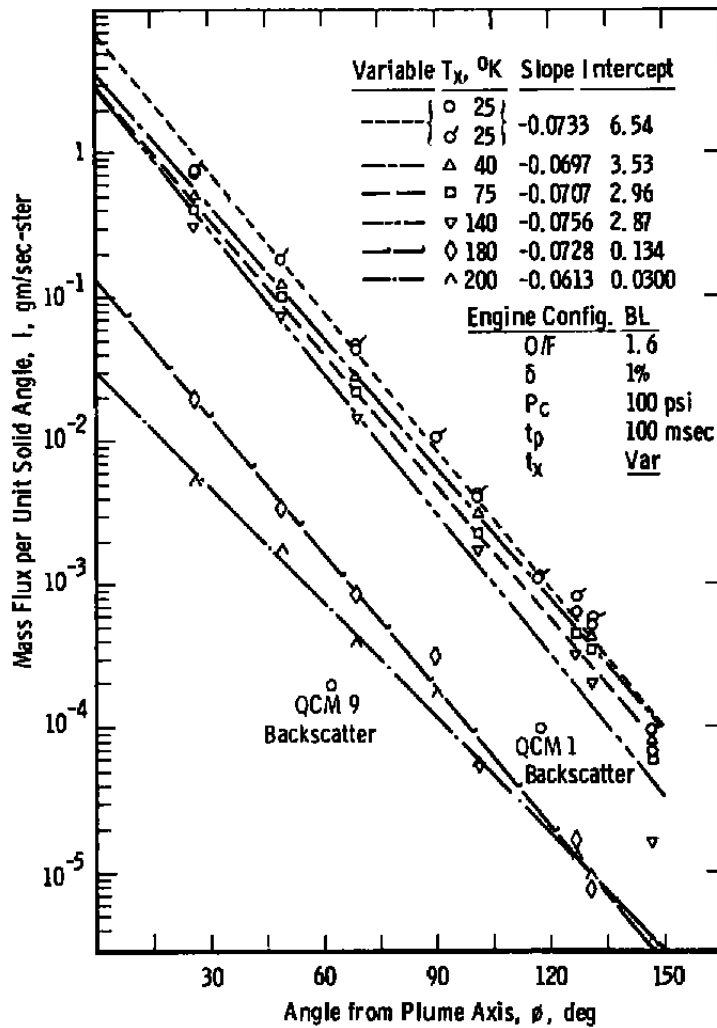
Figure 15. Effect of QCM temperature variation on mass flux.
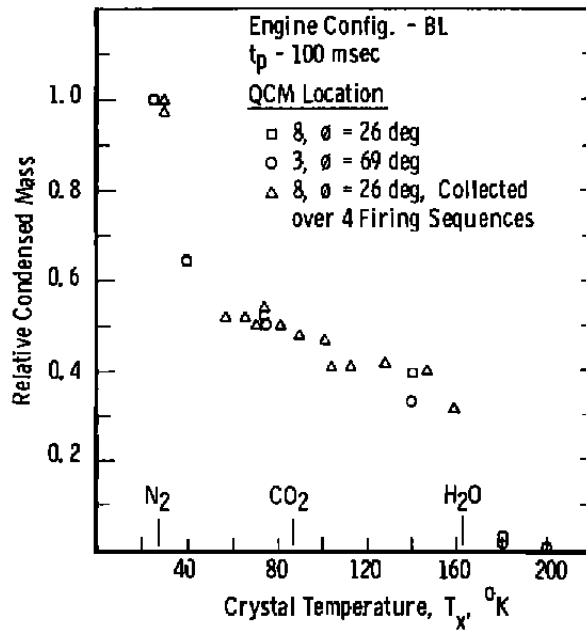
Figure 16. Relative mass collected as function of crystal temperature.

Variable	P_{He}, torr	Slope	Intercept
ʌ	9.0×10^{-6}	-0.0704	6.40
o	1.8×10^{-4}	-0.0699	4.94
⊐	4.8×10^{-4}	-0.0652	2.34
▵	8.4×10^{-4}	-0.0651	2.26
ʌ	4.2×10^{-3}		

Engine Config.	BL
O/F	1.6
δ	1%
P_c	100 psi
t_p	100 msec
T_x	25°K
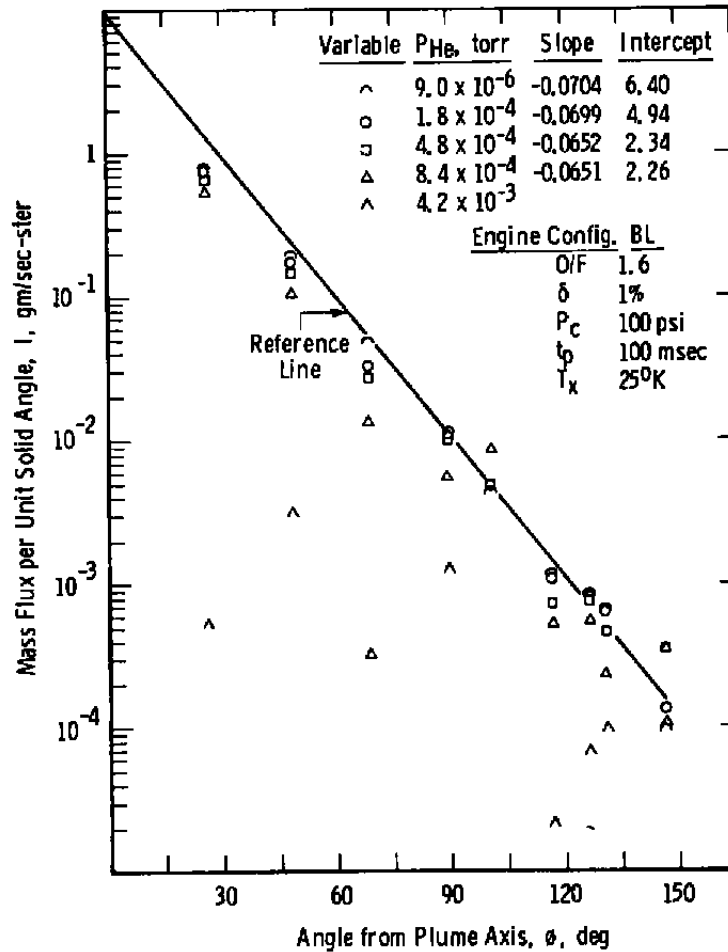
Figure 17. Effect of cryogenic chamber pressure on mass flux.

67
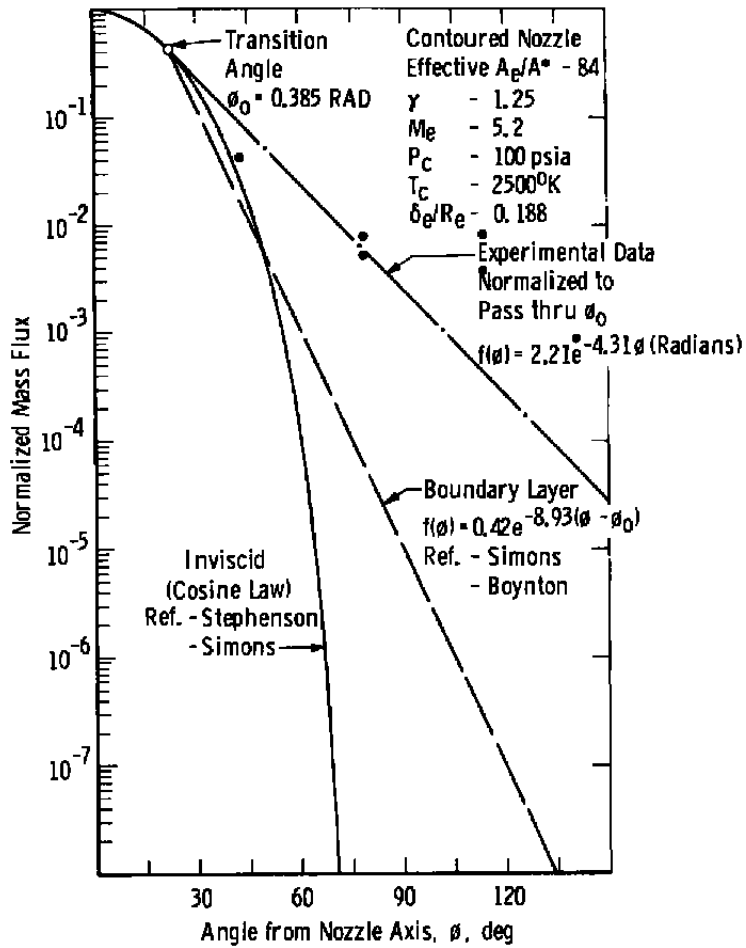
Figure 18. Comparison of measured and calculated mass flux distributions.
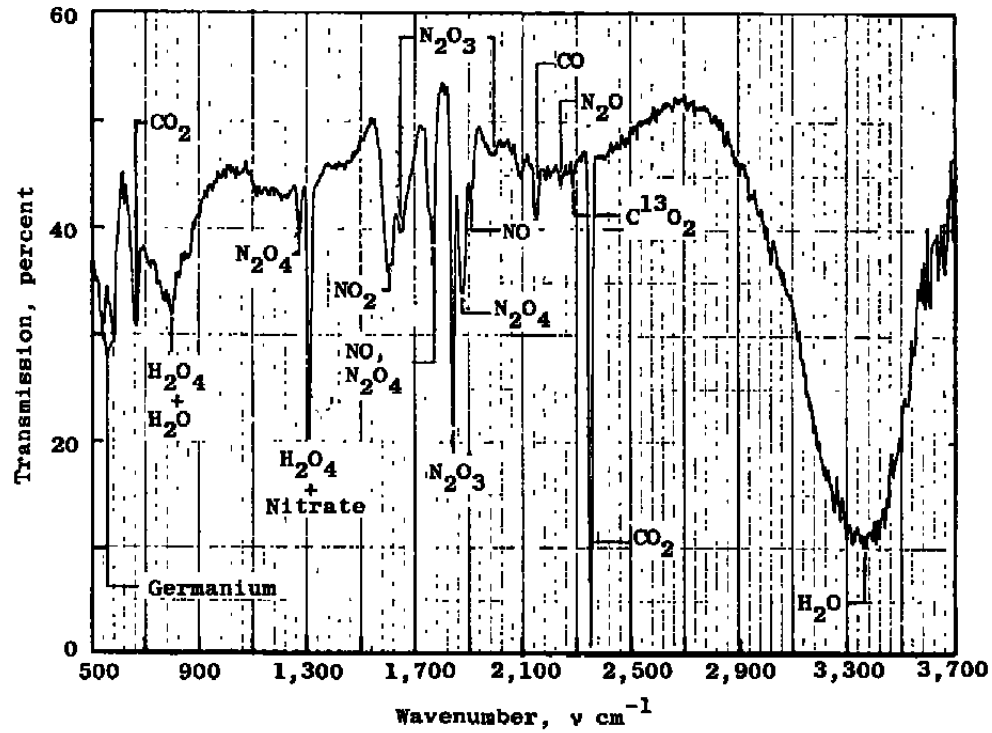
a. Germanium temperature = 26° K

Figure 19. IR transmission of 3.62-μm solid bipropellant plume exhaust.
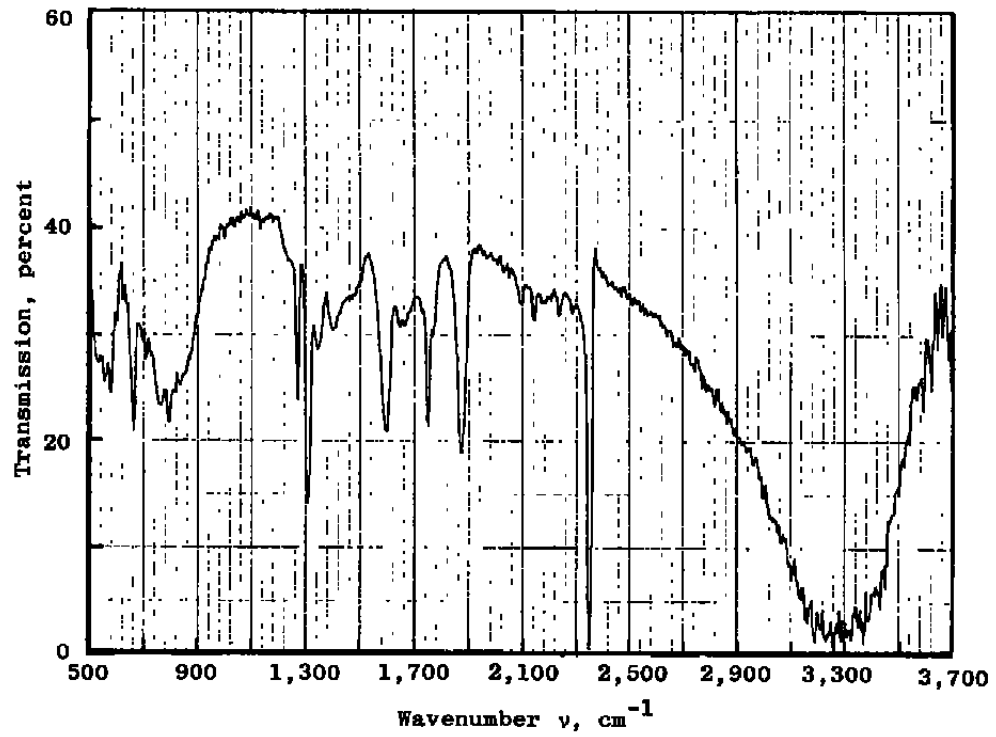
b. Germanium temperature = 96 to 103° K
Figure 19. Continued.
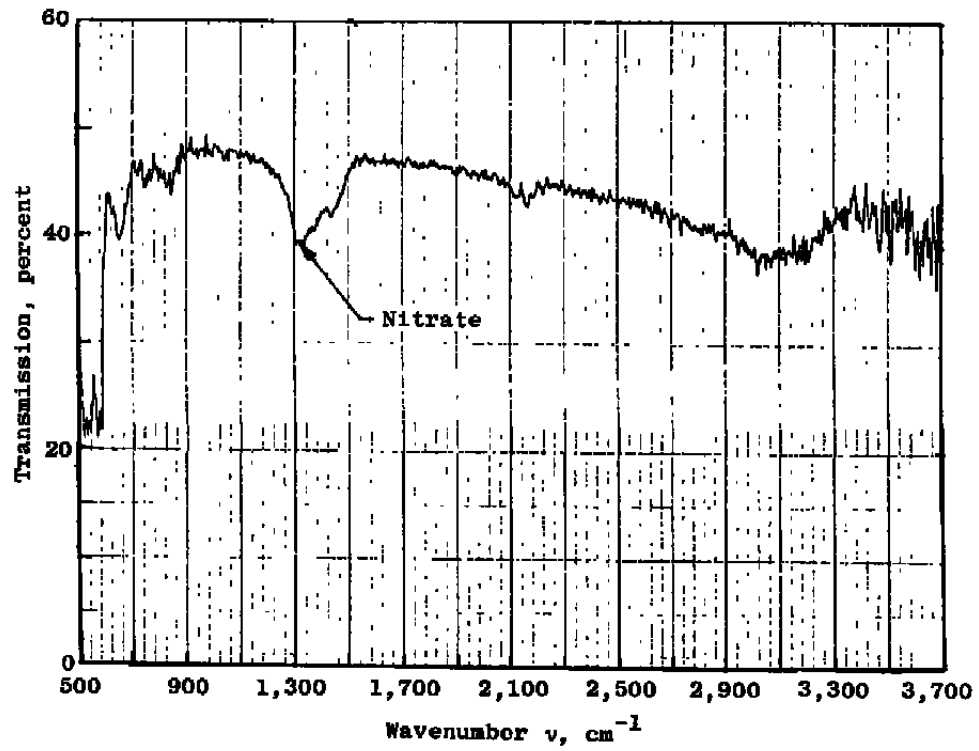
c. Germanium temperature = 220 to 225°K
Figure 19. Concluded.
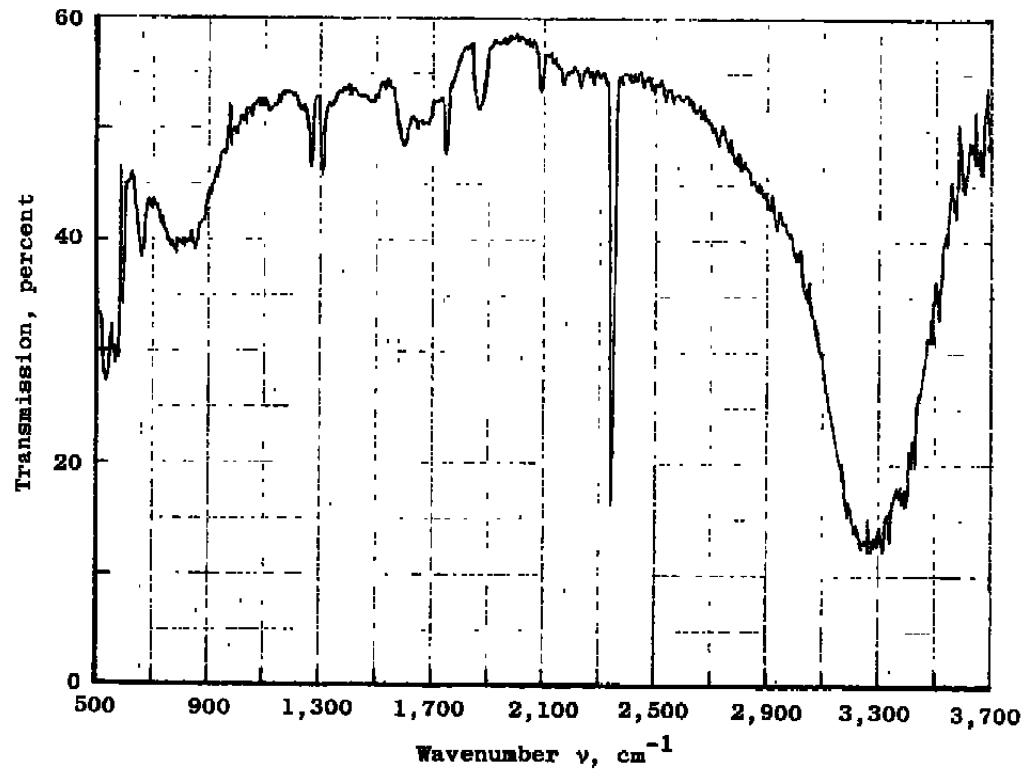
Figure 20. Transmission of 0.89-μm-thick deposit from bipropellant engine condensed on 80°K germanium.
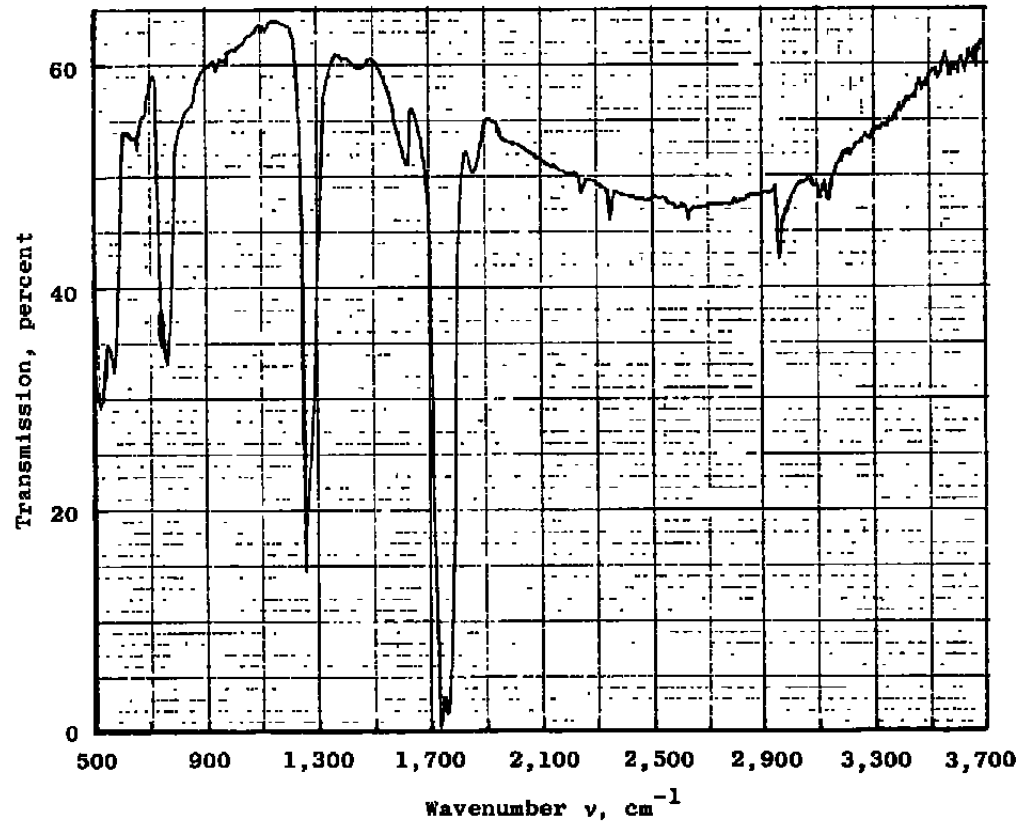
Figure 21. Transmission of 1.22-μm-thick N_2O_4 deposit formed at 77°K.
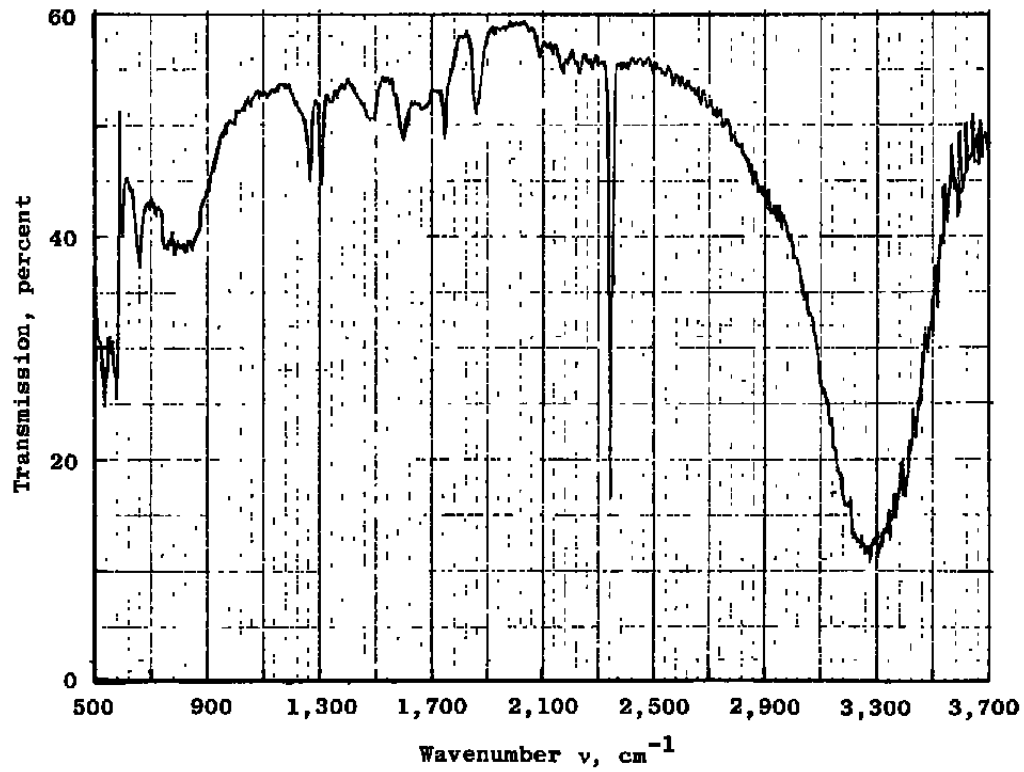
Figure 22. Transmission of 0.89-μm-thick deposit from bipropellant engine formed at 80°K and subsequently warmed up to 124 to 134°K.
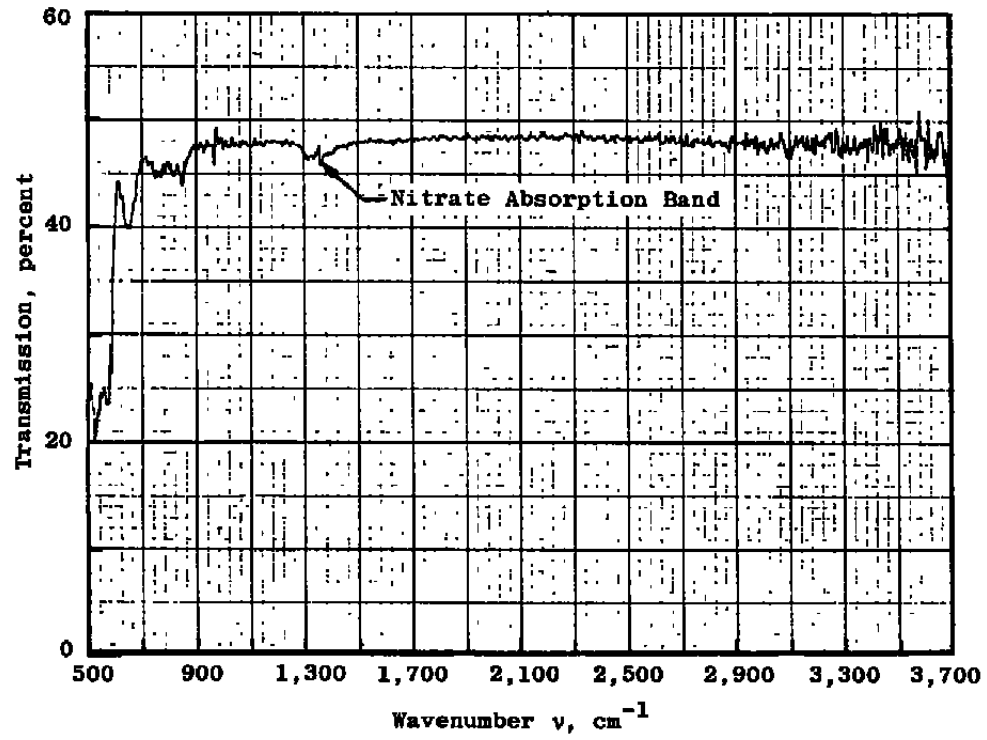
a. On 200°K germanium

Figure 23. Transmission of deposited exhaust constituents.
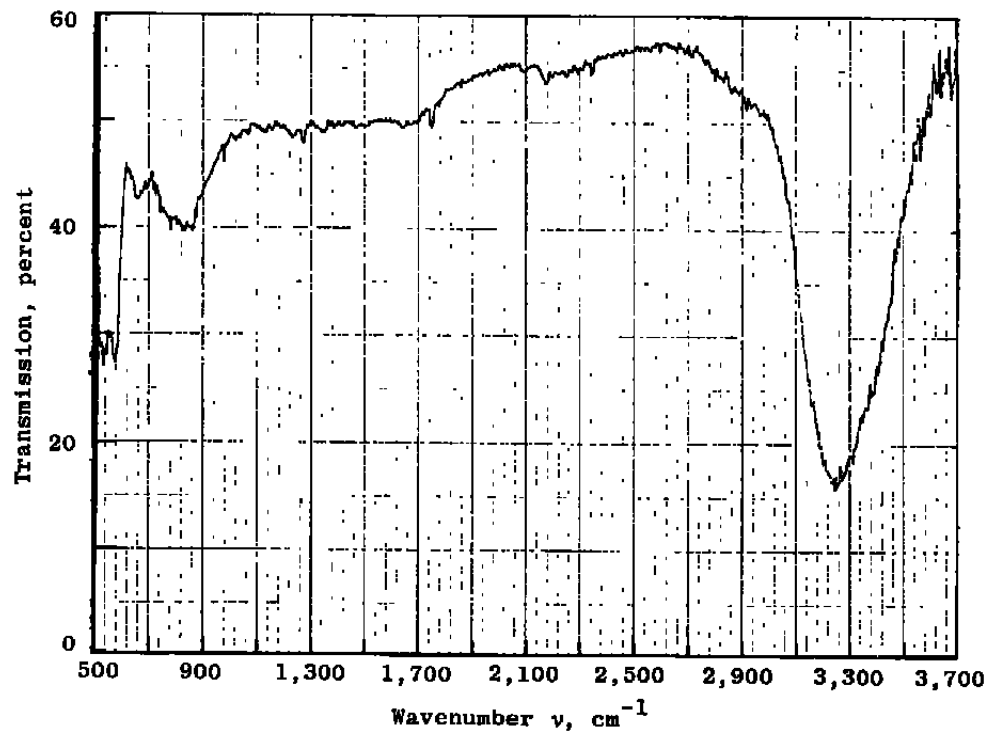
b. On 100°K germanium

Figure 23. Continued.
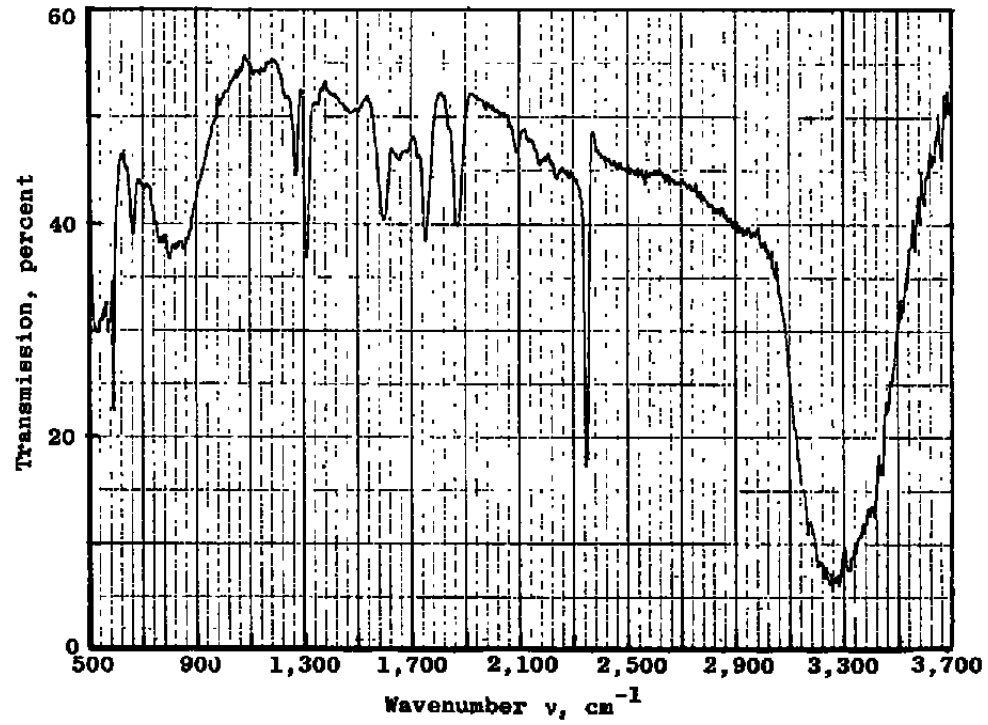
c. On 45°K germanium

Figure 23. Concluded.
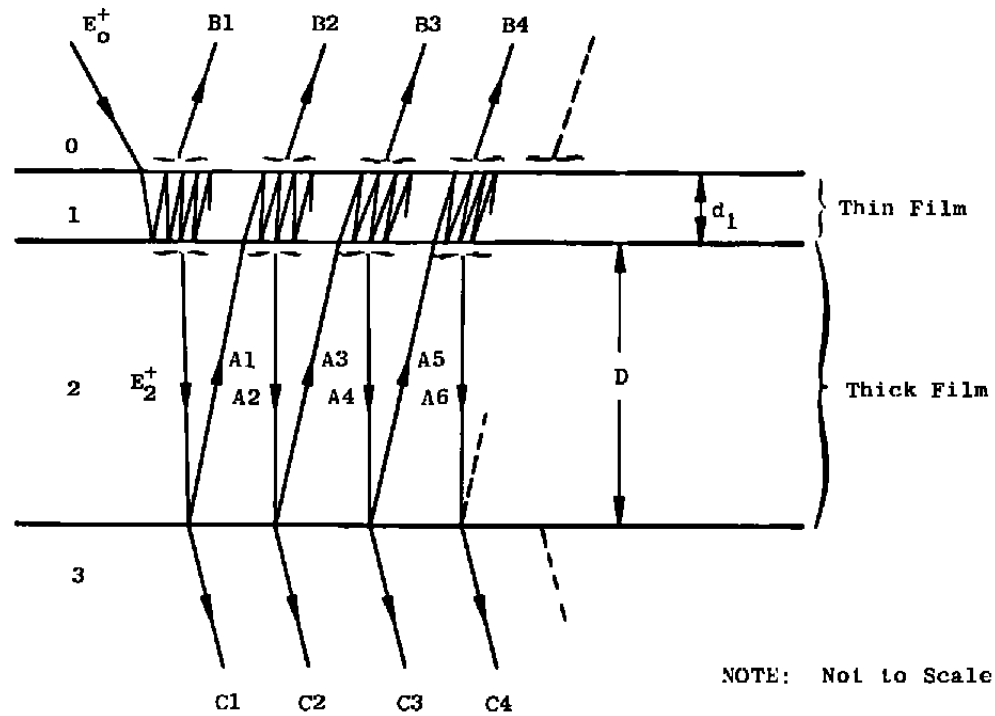
Geometry depicting analytical model for a thin film
formed upon a thick film.

Figure 24. Geometry depicting analytical model for a thin film formed upon a thick film.
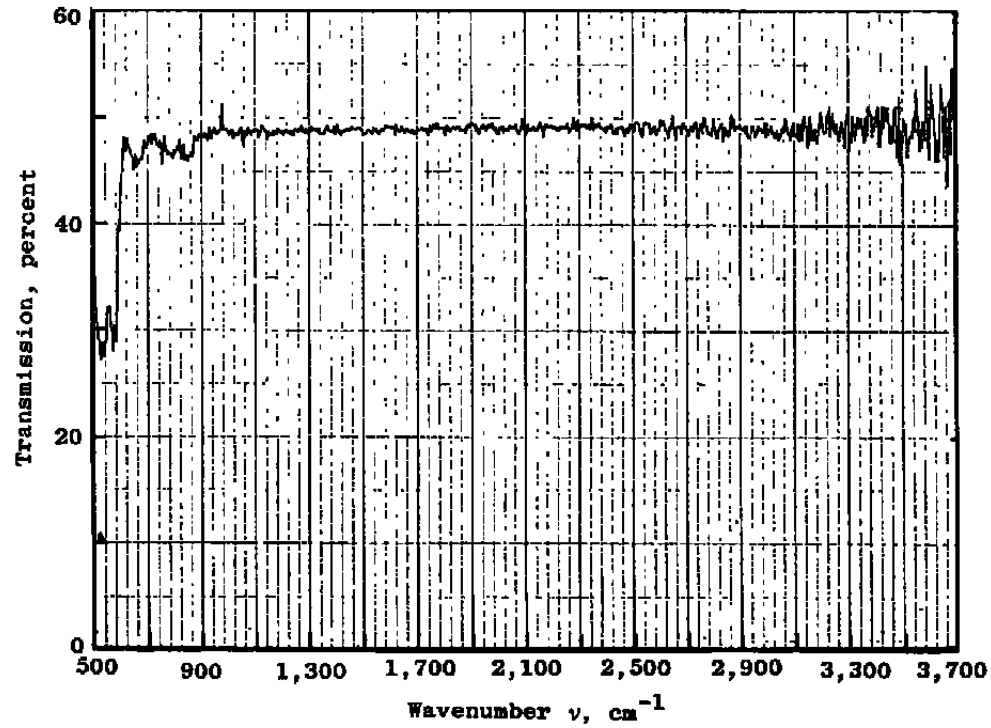
a. Bare 26°K germanium 0.000-μm-thick solid deposit
Figure 25. Transmission of plume exhaust constituents cryopumped on 26°K germanium.
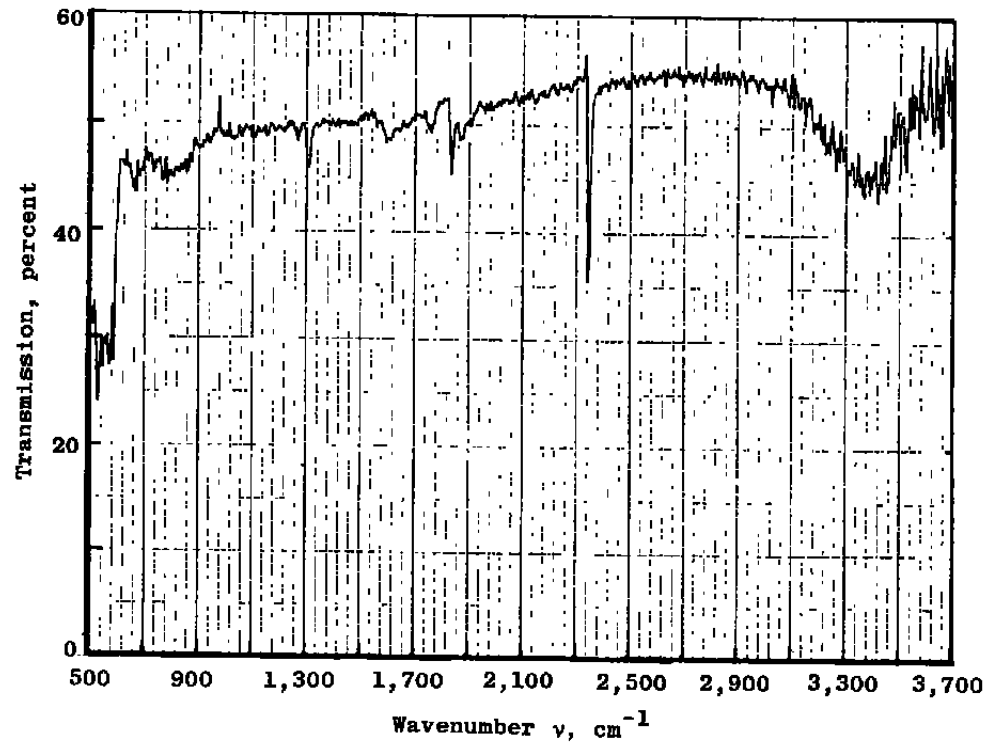
b. 0.471-μm-thick solid deposit
Figure 25. Continued.
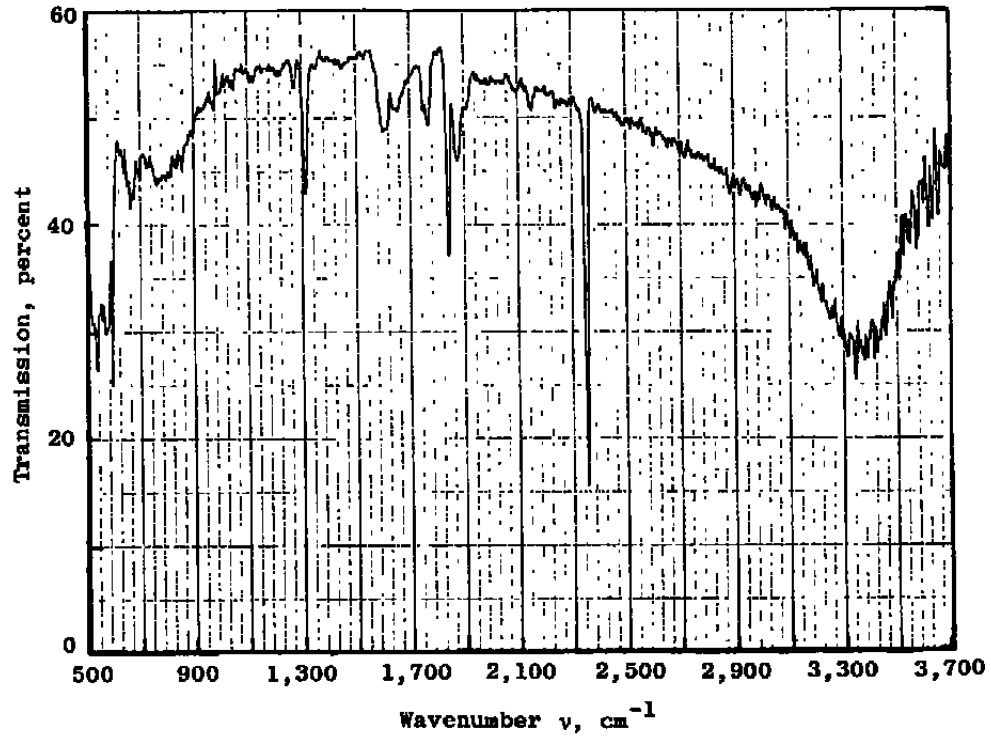
c. 1.18-μm-thick solid deposit
Figure 25. Continued.
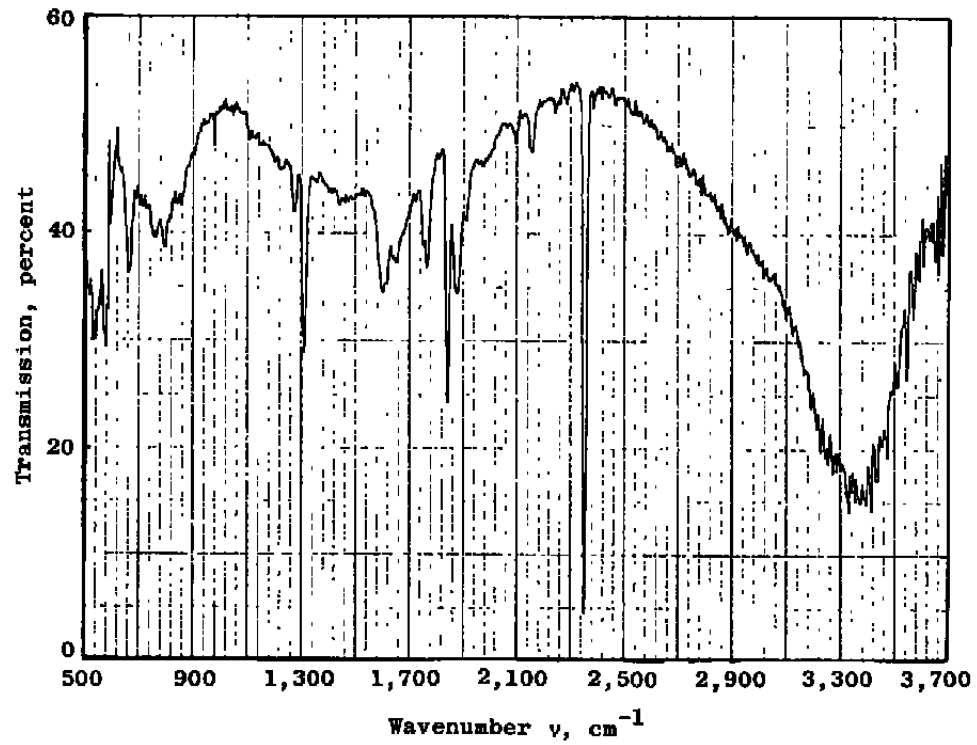
d. 2.35-μm-thick solid deposit
Figure 25. Concluded.
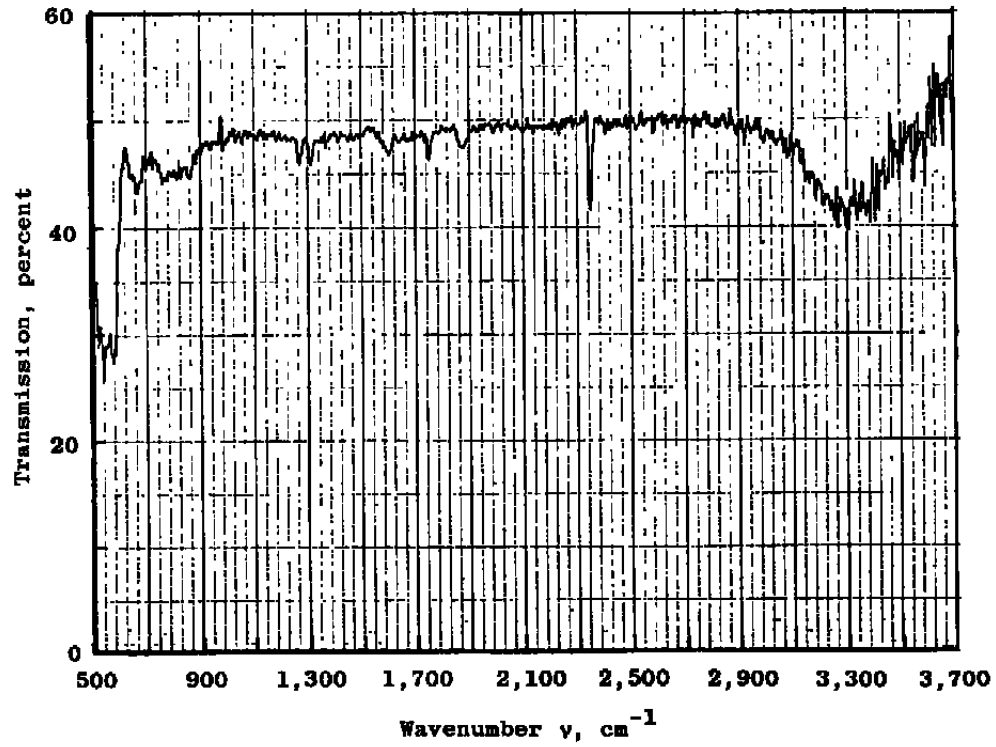
a. 0.223-μm-thick solid deposit

Figure 26. Transmission of plume exhaust constituents on 77°K germanium.
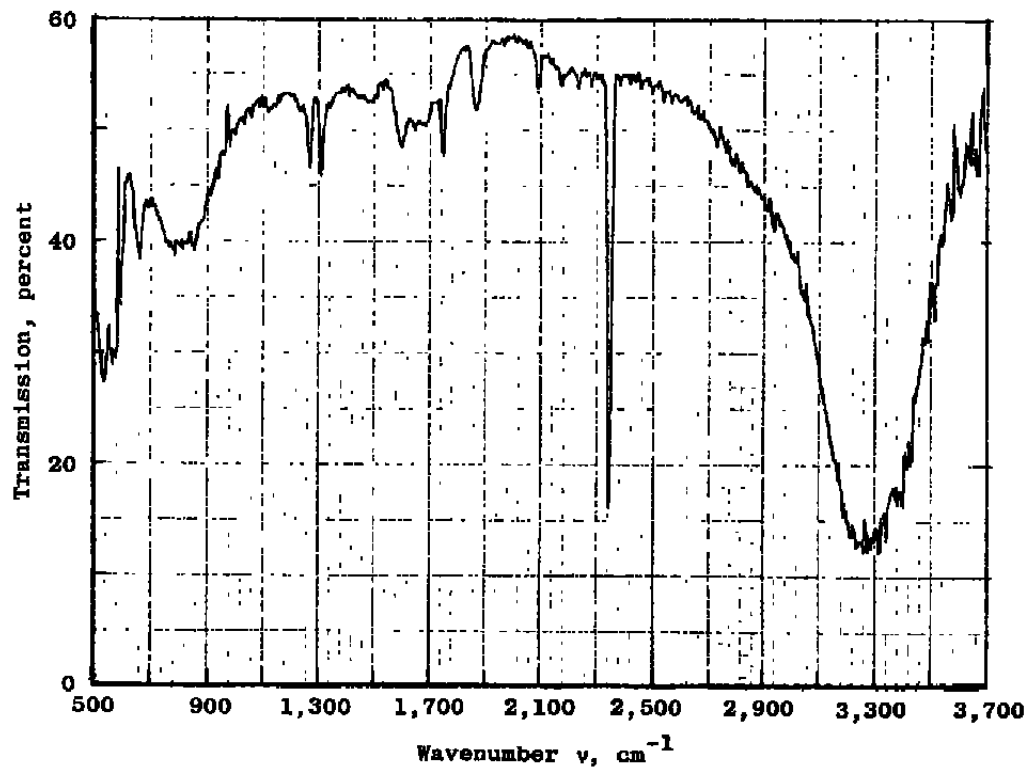
b. 0.894-μm-thick solid deposit
Figure 26. Concluded.
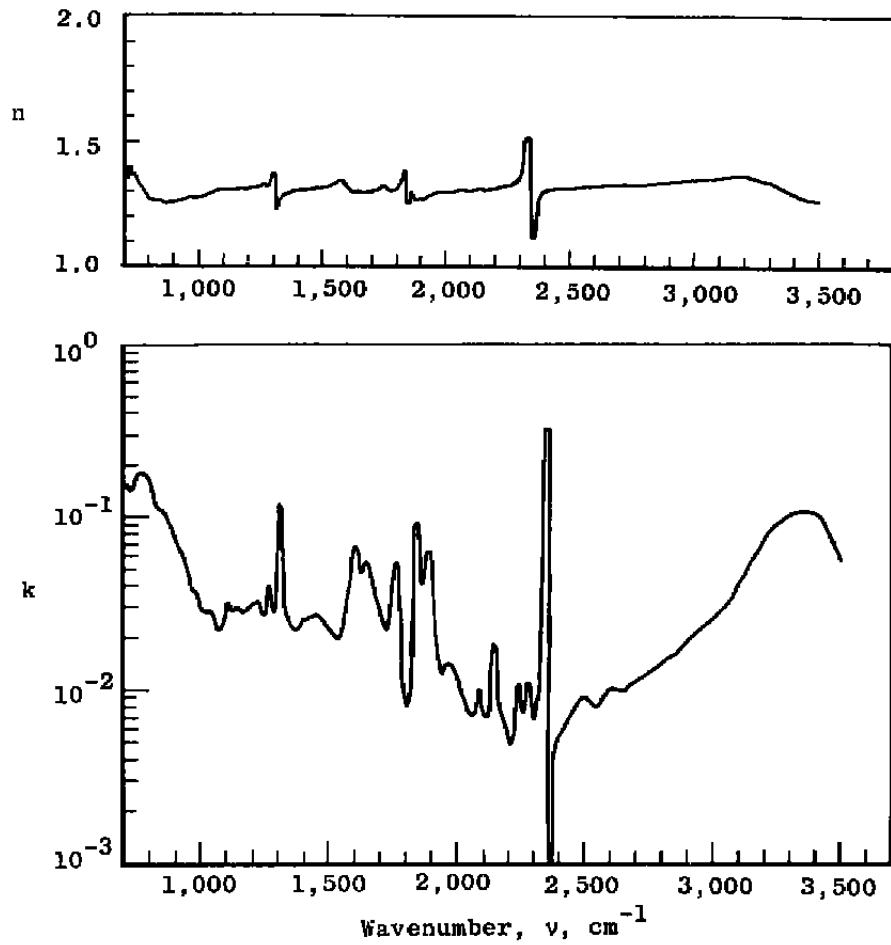
Figure 27. Complex refractive index of bipropellant plume
constituents condensed on 26° K germanium
for configuration BL.
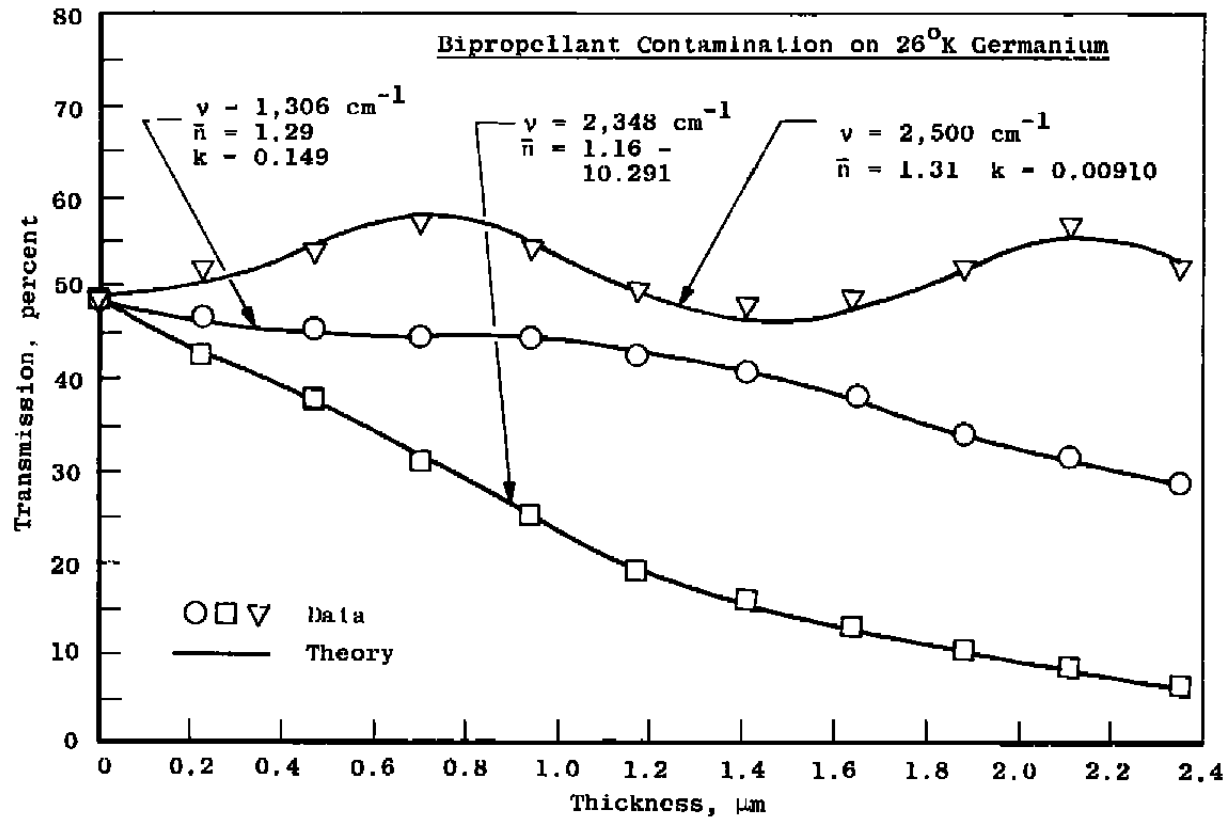
Figure 28. Comparison of theory and data for plume constituents cryopumped on 26°K germanium.
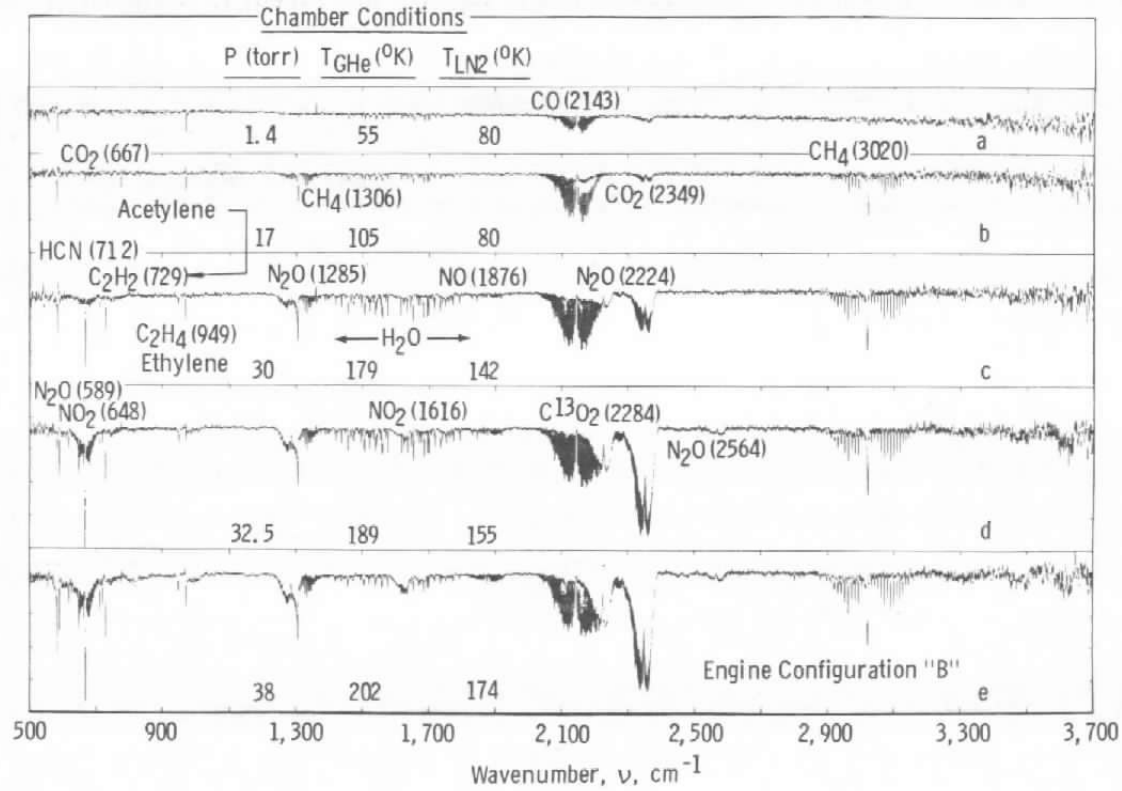
Figure 29. Gas species identification during chamber warmup.
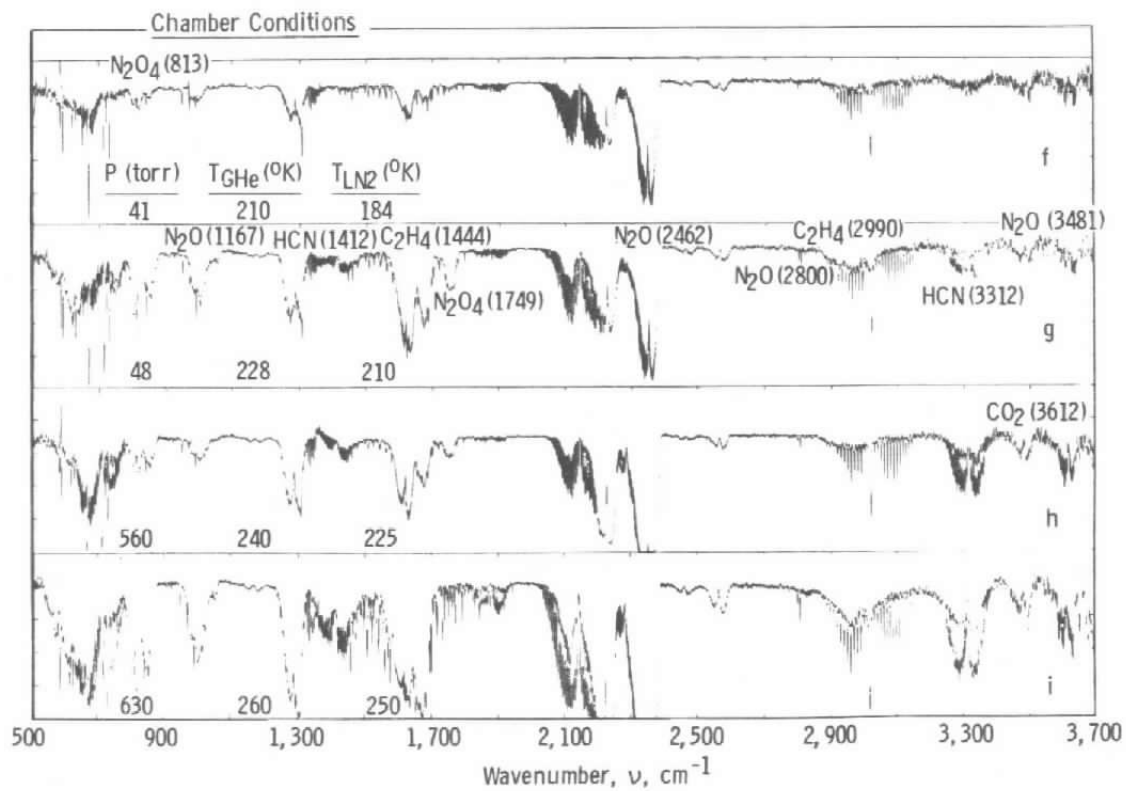
Figure 29. Concluded.
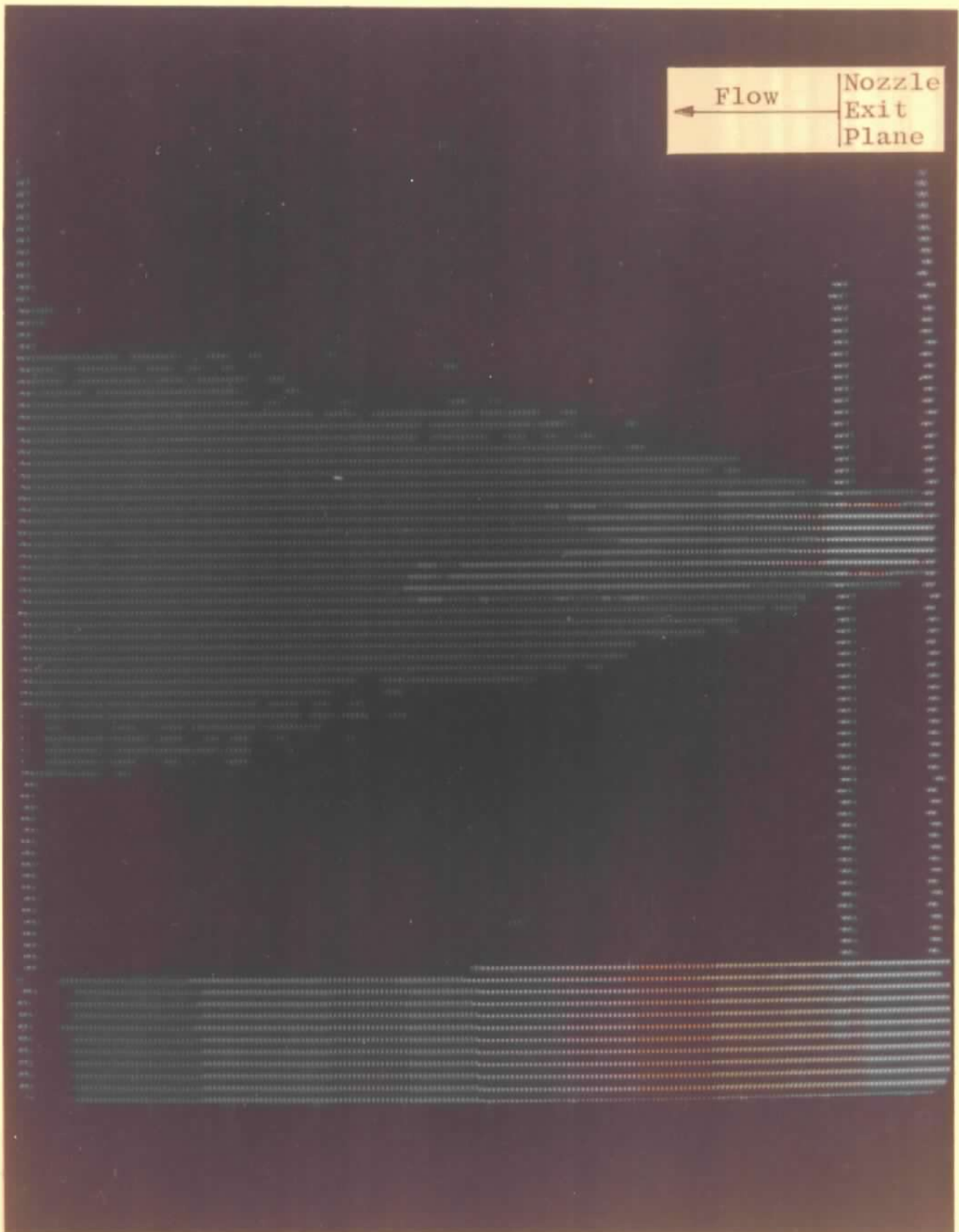
Figure 30. Thermogram of configuration A after 0.50 sec of a 1-sec firing.
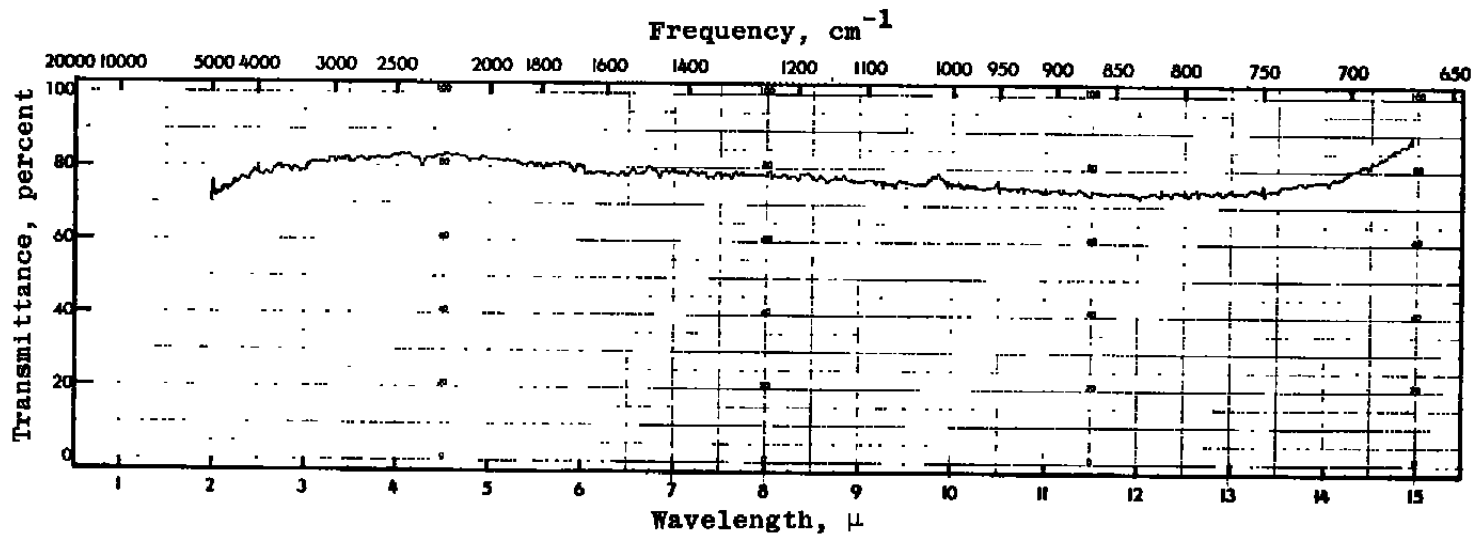
Figure 31. Transmission of clean ATR plate.

Frequency, cm^{-1}

Note: No visible contamination on surface of ATR plate.
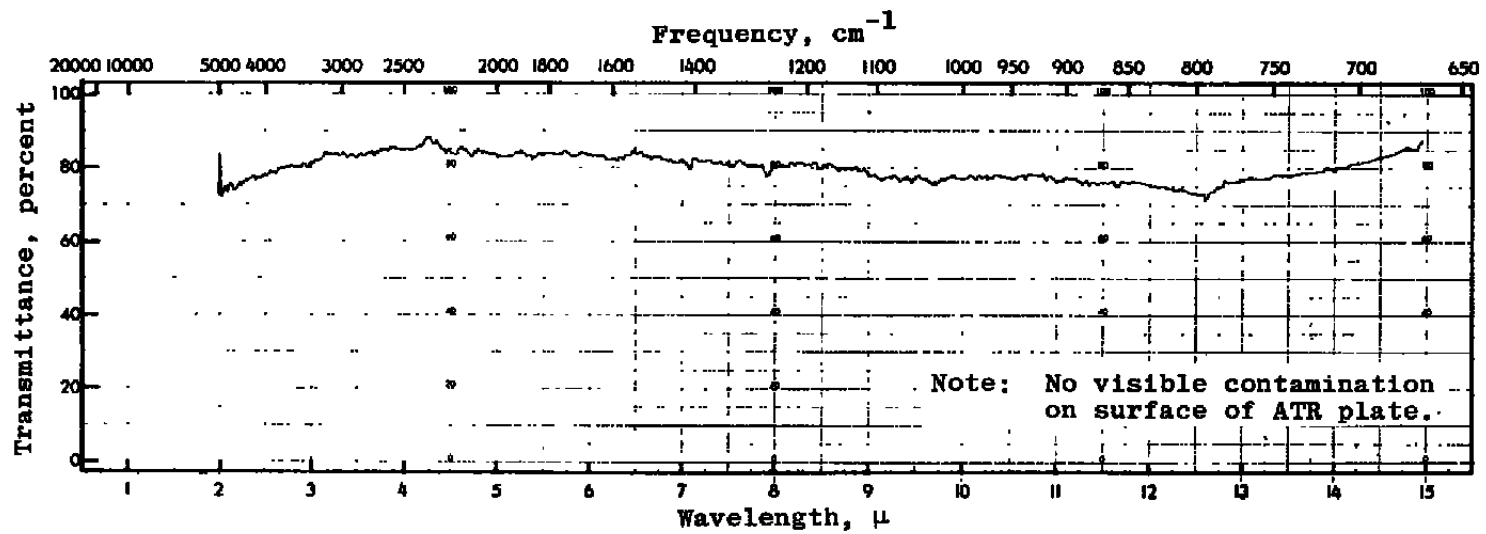
Figure 32. Transmission of ATR plate exposed to 88 sec of engine operation.
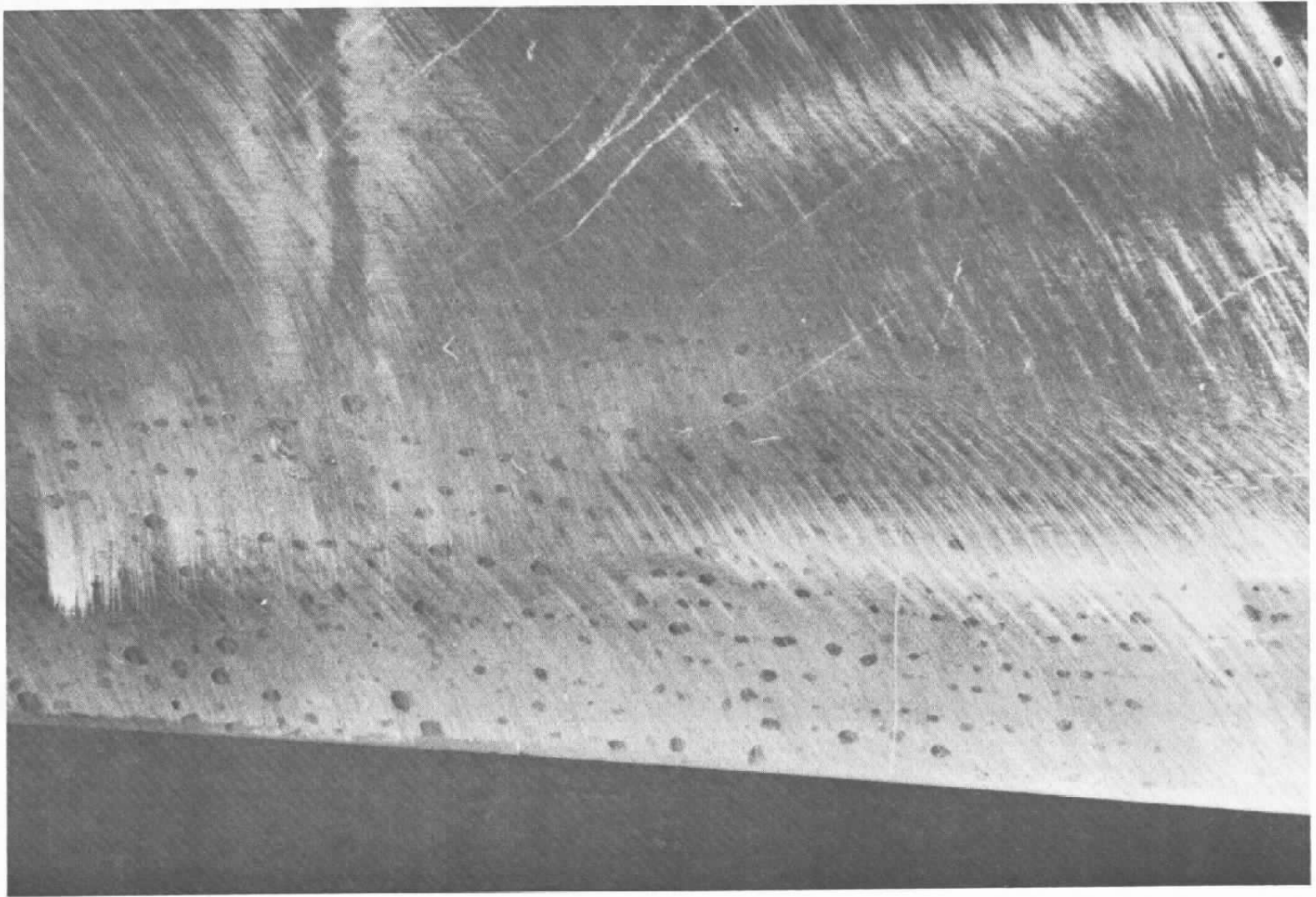
Figure 33. Liquid droplets on cryopanel in forward flow region.
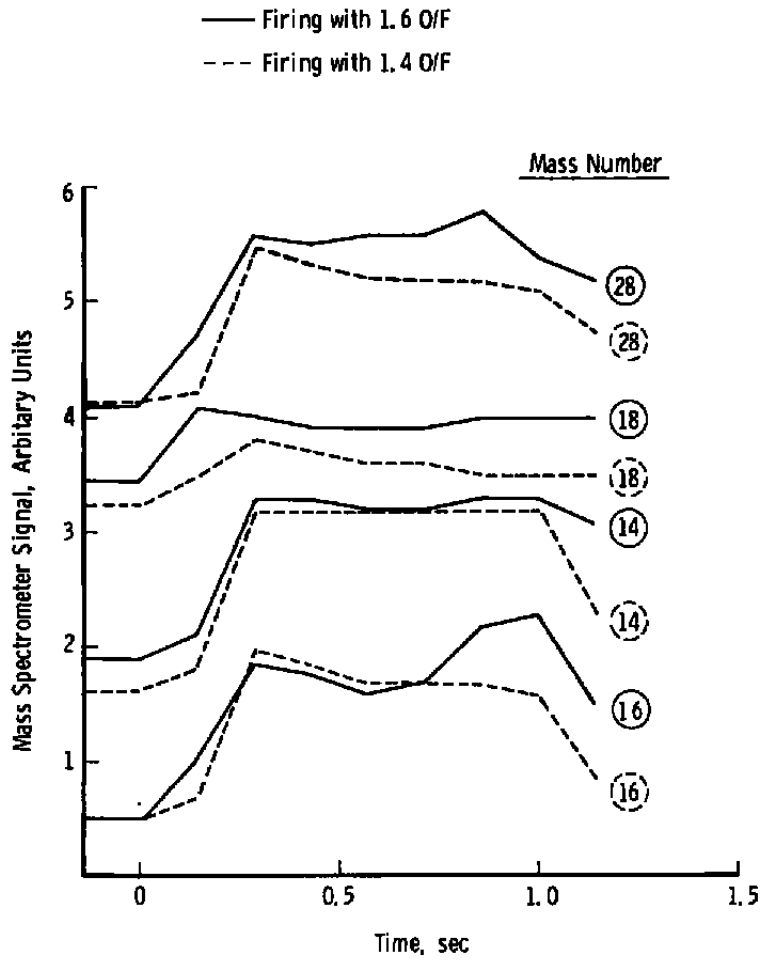
Figure 34. Mass spectrum signals during 1-sec pulse.
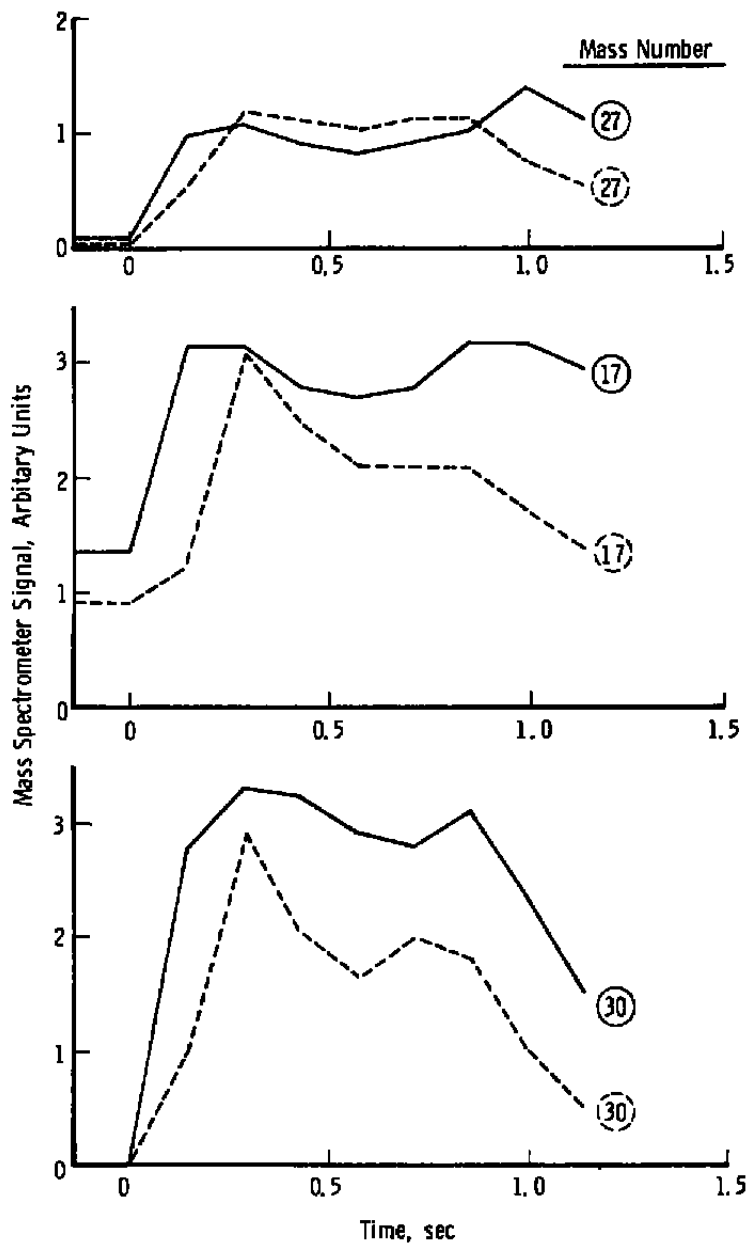
Figure 34. Concluded.

Table 1. Engine Configurations

Config Code	Combustion Chamber Length/Shape	Nozzle Area Ratio, A_e/A_t	Injector Splash Plate Angle, deg	Firing Dates, 1977
C	2 in./cyl.	50	45	Oct 5
A	1.5 in./cyl.	50	0	Oct 17-19
BL	2 in./cyl.	100	45	Nov 8-11
B	1.5 in./cyl.	50	45	Nov 21-23
D	2 in./conical	50	45	Dec 6

Table 2. Bipropellant Engine Specifications

Thrust (Vacuum), lbf	5 max.
Propellants, O/F	N_2O_4/MMH
Mixture Ratio, O/F	1.4/1.8
Chamber Length, in.	1.5 and 2.0
Chamber Pressure, psia	75 to 150
Area Throat, in.^{2}	0.0186
Nozzle Area Ratio, A_e/A_t	50 and 100, Contoured
Injector	Six-Element Splash Plate (0 and 45 deg)
Propellant Flow Rate, lb/sec	0.0167 (P_c = 150 psia)
Inlet Pressure Oxidizer, psia	100 to 300
Inlet Fuel Pressure, psia	100 to 300
Dribble Volume, in.^{3}	0.0006
Nozzle/Chamber Material	Silicide-Coated, Columbium Alloy
Application	Space Propulsion/RCS Buried/Free to Radiate

Table 3. QCM Locations

Location No.	Oct 5, 1977 Configuration – C			Oct 17-19, 1977 Configuration – A			Nov 8-11, 1977 Configuration – BL			Nov 21 – Dec 6, 1977 Configuration – B, D		
	QCM No.	R, cm	φ, deg	QCM No.	R, cm	φ, deg	QCM No.	R, cm	φ, deg	QCM No.	R, cm	φ, deg
1	1	157	30	1[a]	76.7	109	1[a]	81.3	118	1[a]	79.0	115
2	2	112	45	2	61.7	117	2	66.8	131	2	63.6	128
3	3	91	60	3	91.4	60	3	81.0	69	3	83.0	66
4	4[b]	81	90	4[b]	82.3	81	4[b]	83.8	90	4[b]	80.7	87
5	5	79	90	5	78.7	90	5	72.6	101	5	71.8	97
6	6	56	118	6	50.8	111	6	55.9	127	6	53.0	123
7	12	81	108	12	81.3	108	12	76.2	117	12	74.0	114
8	8	91	90	8	91.4	90	10	155.0	26	10	159.6	25
9	9	104	60	9	104.1	60	9[a]	92.9	62	9	94.0	62
10	10	127	45	10	127.0	45	7	112.0	49	7	115.4	47
11	11	172	32	11	73.7	104	11	39.4	147	11	35.3	143
	7	Spare		7	Spare		8	Spare		8	Spare	

[a]QCM Nos. 1 and 9 were pointed downstream toward the far end of the chamber away from the motor with no direct line of sight to the nozzle.

[b]QCM No. 4 was located as close as possible to the germanium substrate for the IR transmittance measurement. It did not have a collimating tube to limit the fov, as did the other QCMs.

Table 4. Operating Conditions

Variable Parameter	Variations with Baseline Conditions Underlined
Oxidizer/Fuel (O/F)	1.4, 1.6, 1.8
Duty Cycle (DC), percent	1, 2, 5, 10, Continuous
Comb. Chamber Pressure (P_c), psia	75, 100, 125
Pulse Length (t_p), msec	25, 50, 100, 200, 1,000
QCM Temperature (T_x), °K	25, 40, 75, 140, ≥ 180

Table 5. Summary of Measurements (Phase 1)

Measurement		Engine Configuration				
		C	A	BL	B	D
QCM's at Crystal Temperature ($^\circ$K)	25	x	x	x	x	x
	40			x	x	x
	75			x	x	x
	100		x	x	x	
	140			x	x	x
	180			x	x	
	≥ 200			x	x	
Condensed Phase In Situ						
-- IR Transmission for						
• Identification of Species Collected by QCMs at Same Temperature				x	x	x
• Optical Constants (n, k)				x		
-- Laser Interference for						
• Cryodeposit Thickness		x	x	x	x	x
• Cryodeposit Density		x	x	x	x	x
• Index of Refraction at 0.6328 µm		x	x	x	x	x
IR Spectra of Gas Phase during Chamber Warmup				x	x	
E-Beam Fluorescence						
• Flow Visualization			x			
• Species Density (Demo)						x
Photography				x	x	
ATR Spectroscopy		x	x	x	x	x
Witness Plates		x	x	x	x	x
Solar Cell Degradation			x	x	x	x
Mass Spectroscopy				x	x	
Thermovision (IR Scanning Camera)			x			

Table 6. Infrared Spectra of Bipropellant Exhaust Products

ν, cm^{-1}	Assignment
665	CO_2
800	N_2O_4, H_2O
1,275	ν_{11} N_2O_4
1,310	N_2O_4, NO_3^-, N_2O_3
1,600	$NO_2 - \nu_3$
1,645	$N_2O_3 - \nu_2$
1,745	$N_2O_4 - \nu_9$
1,765	NO
1,840	N_2O_3
1,880	N_2O_4
1,910	NO
1,980	N_2O_3
2,100	N_2O_4, $\nu_1 + \nu_{12}$
2,150	CO
2,240	N_2O
2,285	$C^{13}O_2$
2,345	CO_2 ν_3
3,300	H_2O

Table 7. Deposition Characteristics of Bipropellant Plume Cryopumped Constituents

Engine Config	Pulse Time, msec	No of Pulses	O/F Ratio	Ge Surface Temp, °K	n	ρ, gm/cm³	Lorentz Constant	Hz per Pulse	Thickness (Å) per Pulse	Mass (μg) per cm² Pulse	Thickness (Å) per sec of Firing	Mass (μg) per cm² sec of firing	Film Total Thickness, μm
A	50	315	1.6	26	1.347	0.747	0.2859	8.2	19.8	0.147	396	2.94	0.624
A	100	180	1.6	26	1.349	0.811	0.2646	14.8	32.7	0.265	327	2.65	0.589
BL	100	451	1.6	26	1.34	0.731	0.2867	10.7	26.0	0.190	260	1.90	2.361
C	100	-	1.6	26	1.35	---	---	. .	---	---	..	---	---
A	100	170	1.4	26	1.334	0.761	0.2713	13.6	33.3	0.253	333	2.53	0.566
A	100	200	1.4	26	1.345	0.737	0.2855	12.7	29.7	0.219	297	2.19	0.594
A	100	139	1.8	26	1.339	0.785	0.2664	16.5	37.2	0.292	372	2.92	0.517
A	100	239	1.8	26	1.329	0.783	0.2599	12.4	29.0	0.227	290	2.27	0.692
D	100	1,332	1.6	75	1.417	1.01	0.2491	7.15	12.8	0.129	128	1.29	1.710
A	100	280	1.6	100	1.346	0.850	0.2506	7.47	15.6	0.133	156	1.33	0.436
D	100	475	1.6	140	1.368	0.850	0.2648	5.07	10.6	0.0901	106	0.901	0.501
D	100	570	1.6	140	1.340	0.837	0.2506	4.89	10.4	0.0870	104	0.870	0.591

Table 8. Solar Cell Exposure to Plume Constituents

Nozzle Config	Elapsed Firing Time, sec	Voltage Reading and Percent Change												Remarks
		Silicon Cells					Selenium Cells					Ext. Selenium		
		1	2	3	4	5	6	7	8	9	10	11	12	
A (50-1)	0 (Baseline)	0.44	0.433	0.447	0.46	0.44	0.08	0.183	0.238	0.15	0.095	0.402	0.11	
	37.75	0.445	0.42	0.43	0.438	0.418	0.08	0.184	0.238	0.152	0.10	0.42	0.116	
		101	97	96	95	95	100	100	100	101	105	105	105	
	125.15	0.44	0.435	0.45	0.458	0.428	0.08	0.19	0.232	0.152	0.099	0.42	0.114	
		100	101	101	100	97	100	104	98	101	104	105	104	
	243.6	0.44	0.408	0.413	0.415	0.39	0.08	0.18	0.231	0.151	0.098	0.42	0.112	Solar Cells Cleaned Between Configs
		100	94	92	90	89	100	98	97	101	103	105	102	
BL (100-1)	0 (Baseline)	0.454	0.465	0.470	0.005	0.460	0.085	0.188	0.220	0.130	0.08	0.29	0.085	
	72	0.40	0.41	0.43		0.465	0.078	0.17	0.20	0.12	0.073	0.21	0.06	
		88	88	92		101	92	90	91	92	91	72	71	
	219	0.475	0.485	0.492	Failed	0.48	0.088	0.195	0.229	0.137	0.085	0.34	0.10	
		105	104	104		104	103	104	104	105	106	117	118	
	366	0.435	0.450	0.468		0.452	0.085	0.189	0.22	0.135	0.081	0.26	0.079	Solar Cells Cleaned
		96	97	100		98	100	101	100	104	101	90	93	
B	0 (Baseline)	0.44	0.46	0.475		0.475	0.093	0.21	0.243	0.141	0.086	0.298	0.090	
	297	0.44	0.46	0.474		0.475	0.091	0.208	0.240	0.140	0.083	0.288	0.087	
		100	100	100		100	98	99	99	99	97	97	97	
	379	0.43	0.46	0.476		0.474	0.091	0.205	0.24	0.140	0.082	0.249	0.082	Solar Cells Not Cleaned
		98	100	100		100	98	98	99	99	95	84	91	
D	0 (Baseline)	0.215	0.23	0.28		0.31	0.079	0.19	0.23	0.133	0.086	0.15	0.050	
	186	0.23	0.245	0.29		0.322	0.08	0.19	0.23	0.135	0.079	0.159	0.055	
		107	107	104		104	101	100	100	103	92	106	110	
	450	0.20	0.21	0.26		0.29	0.063	0.165	0.21	0.085	0.035	0.130	0.04	Very Erratic Readings
		93	91	93		94	80	87	87	65	65	87	80	

Table 9. Calculated Species for O/F Ratio of 1.6

Species	Mass No.	Mole Fraction
H_2O	18	0.3343
N_2	28	0.3075
CO	28	0.1287
H_2	2	0.1576
CO_2	44	0.0401
OH	17	0.0111
H	1	0.0179
O_2	32	0.0007
NO	30	0.0013
O	16	0.0008